

Diss. ETH No. 13617

Transport Measurements on InAs/AlSb Quantum Wells

A dissertation submitted to the
SWISS FEDERAL INSTITUTE OF TECHNOLOGY
ZURICH

for the degree of
Doctor of Natural Sciences

presented by

Sebastian Brosig

born May 10th, 1967
in Gelsenkirchen (D)

accepted on the recommendation of

Prof. Dr. Klaus Ensslin, examiner
Prof. Dr. Andreas Wieck, co-examiner

2000

Zusammenfassung

Indiumarsenid/Aluminiumantimonid (InAs/AlSb) Quantentöpfe stellen nach wie vor ein faszinierendes Objekt für die physikalische Forschung dar. Besondere Eigenschaften sind in erster Linie das tiefe Einschlusspotential im Quantentopf und die kleine effektive Masse der Elektronen, beides bedingt durch die kleine Bandlücke in InAs. Mögliche Anwendungen des ein wenig exotischen Materialsystems ergeben sich im Hinblick auf die aufgehobene Spinentartung bei $B = 0$. Die durch ein elektrisches Feld abstimmbare Spin-Orbit-Kopplung könnte phasenkohärente Devices für den Quantencomputer möglich machen. Mittels Molekularstrahlepitaxie können InAs/AlSb-Schichten mit sehr guter Raumtemperatur-Beweglichkeit und einer ausreichenden Quanten-Streuzeit für Tieftemperaturexperimente gewachsen werden.

Zunächst werden generelle Eigenschaften von Elektronen in solchen zweidimensionalen Systemen diskutiert. Insbesondere Quantisierungseffekte durch die Beschränkung der Bewegung in der Ebene, und lateral durch weitere Strukturierung der Schichten sowie durch das Anlegen eines magnetischen Feldes spielen hierbei eine Rolle. In diesem Zusammenhang wird auf quantitative Methoden zur Auswertung von Shubnikov-de Haas-Oszillationen besonders eingegangen. Weiter wird speziell für den Fall von InAs/AlSb-Quantentöpfen auf den Einfluss des Gitters auf die Dynamik der Elektronen eingegangen. Der Spin der Elektronen spielt in diesem Material eine große Rolle, da die Zeeman-Aufspaltung in diesem Material besonders hervortritt. Der g -Faktor in Volumen-Indiumarsenid beträgt $g = -14$. Die im Zusammenhang mit der vorliegenden Arbeit wichtigen apparativen Techniken, sowohl was die Experimente selbst wie auch deren Auswertung angeht, werden detailliert beschrieben.

In starken Magnetfeldern kondensiert die Zustandsdichte der Elektronen zu Landau-Niveaus, für die Stärke der Quantisierung ist in erster Linie die Komponente der Feldstärke senkrecht zur Ebene des Quantentopfes bedeutend. Für die Spinaufspaltung jedes dieser Niveaus gibt aber die gesamte Stärke des Magnetfeldes den Ausschlag. Diese Tatsache wird verwendet, um mit dem Winkel zwischen Probenebene und Magnetfeld verschiedene Szenarien der Spinaufspaltung zu realisieren. Im Experiment treten verschiedene Effekte auf, die mit einem einfachen Bild von unabhängigen Landau- und Spinniveaus nicht in Einklang stehen und auf die Nichtparabolizität von InAs und Wechselwirkungseffekte schließen lassen.

Auch ohne ein äußeres Magnetfeld ist die Energie von Elektronen mit unterschiedlichem Spin nicht entartet. Diese Tatsache ist einerseits durch die Inversionsasymmetrie der Kristallstruktur bedingt, andererseits durch das in die Schichtstruktur „eingebaute“ elektrische Feld. In den hier untersuchten Proben gibt es aber Diskrepanzen zu den gängigen Modellen: die gefundene Aufspaltung war entweder überhaupt nicht meßbar oder viel kleiner als vorhergesagt, was anhand der Experimente diskutiert wird.

Da InAs/AlSb-Quantentöpfe nicht ohne weiteres mit einem Metallfilm als Gate versehen werden können, ist man in erster Linie auf andere Methoden zur Variation der Elektronendichte angewiesen. Eine dieser Methoden ist es, mittels starkem hydrostatischem Druck den Gitterabstand der Atome im Kristall direkt zu reduzieren. Hierzu werden Experimente vorgestellt. Eine weitere Technik zum Ändern der Elektronendichte ist mit der kurzzeitigen Beleuchtung der Probe gegeben. Damit ist in einigen Proben eine persistente Reduktion der Elektronendichte verbundenen. Auch diese Trick wurde verwendet und die Ergebnisse vorgestellt.

Im Anhang wird unter anderem auf die experimentelle Praxis mit Druckzellen eingegangen.

Abstract

Indium arsenide/aluminium antimonide (InAs/AlSb) quantum wells continue to be a fascinating object for physical research. Special features are the deep confinement potential and the small effective mass of the electrons, both consequences of the small band gap in InAs. Possible applications of this somewhat exotic material system might exploit the lifted spin-degeneracy at $B = 0$. The spin-orbit coupling can be tuned with an electric field, which could make phase-coherent devices for a quantum computer possible. Using molecular beam epitaxy, InAs/AlSb layers can be grown with very good room temperature mobilities and sufficient quantum scattering times to allow for low temperature experiments.

First, some general properties of electrons in these two-dimensional systems are discussed. Quantization effects due to the confinement in the plane as well as due to further lateral confinement, either from further lateral structuring of the samples or by the application of a perpendicular magnetic field, play an important role here. The quantitative analysis of Shubnikov-de Haas oscillations is discussed in detail. In the particular case of InAs/AlSb quantum wells, effects of the crystal lattice on the dynamics of the electrons are shown. The spin of the electrons plays an important role in InAs because the Zeeman-splitting in this material is large: the bulk InAs g factor is $g = -14$. The techniques employed in this thesis are treated next, the experimental details as well as the methods of data evaluation.

In strong magnetic fields, the electronic density of states condenses into Landau levels, the component of the field perpendicular to the sample plane being most important for the amount of splitting. For the splitting of each of these levels in two, for the two spin directions, the total magnetic field counts. This is employed to realize various scenarios of spin- and Landau splitting, by tuning the angle between the sample normal and the magnetic field. Various effects occur in the experiment that can not be explained by the simple coincidence picture, and that allow to draw conclusions about exchange effects and non-parabolicity of InAs. Even without an external magnetic field, the degeneracy of electrons with opposing spin directions is lifted — on the one hand, by the inversion asymmetry of the crystal structure, on the other hand, due to the “built-in” electric field in the sample. However, in the data from samples featured here, there are discrepancies to the accepted models: the

splitting was either not found or far smaller than predicted, which is discussed with the experiments.

Since InAs quantum wells cannot be tuned easily by the application of an electrostatically biased metal gate, one is dependent on other methods of changing the electron density. One of these methods is the modification of the lattice constant by application of high hydrostatic pressure. Experiments are presented using this technique. Another method of adjusting the electron density is shining a short light pulse onto the sample, which leads to a persistent lowering of the density. This trick was used as well, and results are shown.

In the appendix the know-how concerning pressure cell methods is given a treatment that focuses on the practical side of the technique.

Contents

1	Introduction	6
2	Two-Dimensional Electron Systems	11
2.1	Basic Properties	11
2.1.1	Confinement in one Dimension	12
2.1.2	Motion in two Dimensions	13
2.2	Electrons in a magnetic field	13
2.2.1	Perpendicular Field	13
2.2.2	Tilted Field	15
2.2.3	Density of States in a Landau-quantized 2DEG	15
2.2.4	Conductivity in weak magnetic fields	17
2.3	Quantum Hall Effect	17
2.4	Model Calculation for ρ_{xx} from the Landau-quantized DOS	19
3	InAs/AlGaSb quantum wells	27
3.1	Bulk materials	27
3.1.1	Indium Arsenide	27
3.2	MBE-grown InAs/AlSb quantum wells	29
3.2.1	Sample Growth	29
3.2.2	Origin of the Quantum Well Electrons	31
3.2.3	Magnetotransport	33
4	Experimental Methods	35
4.1	Sample preparation	35
4.2	Transport Measurements	36
4.3	Cryostat environment	36
4.4	Tilted Field	39
4.4.1	Precision of Angle Determination	40
4.5	Hydrostatic Pressure	41
4.5.1	Pressure Cell	41
4.5.2	Pressure Sensors	42

4.6	Effective mass determination	44
4.7	Determination of τ_Q	46
5	Spin splitting in a tilted magnetic field	48
5.1	The Coincidence Method	49
5.2	Decreasing density with strong B_{\parallel}	57
5.3	Failure of the Simple Coincidence Model	59
5.3.1	Cross-over from Even to Odd SdH minima at constant angle	59
5.3.2	Level Anticrossing	61
5.3.3	More B_{\perp} -dependent Structure	64
5.4	Measuring the Zeeman and Landau gap simultaneously	66
6	Zero-Field Spin-Splitting, and its absence	69
6.1	Theory of zero-field spin splitting	70
6.1.1	Rashba term calculated in the $\mathbf{k} \cdot \mathbf{p}$ approximation	70
6.2	Experiments	72
6.2.1	Modifying the carrier density by illumination	72
6.2.2	Changing the carrier density by hydrostatic pressure	73
6.2.3	SdH beatings induced by inhomogeneous illumination	73
6.2.4	More beats	75
7	Hydrostatic pressure on InAs/AlSb quantum wells	79
7.1	Bulk materials	79
7.2	InAs/AlSb Quantum Wells	80
7.3	Conclusion	85
8	Negative Persistent Photoconductivity Effect	86
8.1	Experiments with Illumination	86
8.2	Sample Dependence	87
8.3	Inhomogeneous Illumination	87
8.4	Decay of NPPC, Temperature Dependence	88
A	Gating InAs/AlSb Samples	90
A.1	Silicon Oxide-Insulated Gates	90
B	Samples	93

C The making and use of a clamped pressure cell	98
C.1 Making Pressure Sensors	98
C.1.1 Manganine Gauge	98
C.1.2 InSb Gauge	98
C.2 Parts	99
C.3 Making Wire Feedthroughs	100
C.4 Assembly	101
C.5 Pressurizing	102
C.6 Cooldown and Warmup	102
D Glossary	104
Bibliography	106
Curriculum Vitae	111
Acknowledgements	112

Chapter 1

Introduction

Since it has been possible to produce crystals of very high purity, semiconductors have advanced from specialist topic for some physicists towards an industry that, arguably, has an impact on everyone. After semiconductors had been accepted as a new class of material, their fascinating properties have been subject to intensive investigation. Many research results found applications immediately. The proliferation of technology that the industrial production of semiconductor devices demanded became beneficial, in turn, to basic research. The possibility of making layered systems with atomic precision came along as a milestone in the development of semiconducting materials [Cho71]. Lattice-matched crystals with different electronic properties can be stacked onto one another. The best way to do this, from the point of view of quality, is molecular beam epitaxy, where the individual components are evaporated and made to condense on a substrate in a good vacuum.

The two-dimensional electron systems in these structures exhibit unique properties. Some of these properties, specifically the fast switching of junctions, have become indispensable in the gadgets that modern, civilized people evidently have a great need for. But since the spatial dimensions of such layered systems are on a length scale that approaches that of the microscopic world of atoms, the physical laws that govern the microscopic world determine the behaviour of these electronic systems. This has made the ensemble of highly mobile electrons that form in the carefully designed semiconductor layers a new playing field for physicists. The two-dimensional electrons as a whole are often referred to as a 2D electron gas, or 2DEG for short. Very briefly, the standard trick with 2DEGs is to separate spatially the electrons from the ionized donors that generated them: By stacking materials with different band gaps it is possible to confine electron to one layer. The doping layer with many scattering centres is placed at a distance from the electron layer so that scattering between electrons and their donors is substantially reduced.

At low temperatures, when the crystal lattice is not distorted by the thermal agitation of the atoms, quantization effects to play a role. In a strong magnetic field, under the conditions of the quantum Hall effect, electrical properties of a 2DEG are governed by quantum mechanics entirely: the Hall resistance is then just a combination of fundamental constants and no properties of the individual sample play a role [Fowler66, vKlitzing80]. Chapter 2 deals with some important properties of two-dimensional electron gases from an abstract point of view. A numerical model calculation was employed to gain understanding of the details of magnetoresistance curves. The model calculates the conductivity as a function of magnetic field, temperature, and other parameters, from a modelled density of states.

Apart from these more general properties of a 2DEG, the material itself does influence the behaviour of the electrons. The effective mass of electrons in semiconductors is often reduced with respect to the mass of a free electron. This is a consequence of the band structure. Small bandgap materials generally have small effective masses. The low effective mass, in turn, leads to a high electron mobility, which is of course an interesting parameter from the point of view of applications. The material systems used in this thesis is InAs/AlSb and InAs/AsGaSb. It is not as well-studied as the much more common GaAlAs/GaAs system, but it has some interesting properties. The effective mass in Indium Arsenide is very small, so that the electron mobility is high. AlSb has a relatively large band gap, so that the confining potential is very strong. Electron gases with high electron density can be realized. Together with the high electron mobility¹ of up to $80 \text{ m}^2/\text{Vs}$, the sheet resistance of these layers is very low, typically of the order of 10Ω . InAs/AlSb quantum wells generally have a high electron density even when no intentional doping is introduced to the layers. Several mechanisms have been discussed as a possible source of the electrons [Nguyen93, Kroemer92, Tuttle90a]. Forming Ohmic contacts to connect the 2DEG to the outer world electrically is not always easy in the GaAlAs/GaAs system, but with InAs quantum wells this is generally no problem. The surface chemistry of InAs is such that the Fermi energy is pinned in the conduction band, which means that it is sufficient to evaporate some metal onto the quantum well to form a good contact. These special properties of the InAs/AlSb system are covered in chapter 3.

The experimental methods that were employed are explained in chapter 4. This includes an account of how the samples were prepared for electrical mea-

¹SI units are used throughout this manuscript, even though the electron mobility numbers are more impressive in the customary unit: $800\,000 \text{ cm}^2/\text{Vs}$.

surement, the mode of measuring electrical resistance at low temperatures, high magnetic fields, and under the application of high hydrostatic pressures. The technical details of the pressure cell are covered in Appendix C. Magnetooscillations of the electrical resistance are used extensively to gain insight into the processes that govern the behaviour of 2D electrons. The techniques that were employed to evaluate these curves in terms of the effective mass m^* and the quantum scattering time τ_Q are also explained here.

The electron spin plays an important role in InAs: because the g factor is large in the crystal, compared to the free electron value, the spin splitting is noticeable at comparatively low fields. Chapter 5 deals with tilted field measurements and the spin splitting. In a magnetic field perpendicular to the sample normal, the spin splitting amounts to about 1/5 of the Landau splitting. But the ratio between spin and Landau splitting can be tuned with the angle under which the magnetic field is applied. When certain coincidence situations are met, for example when the Spin splitting is equal to the Landau splitting, this is reflected in the appearance of magnetooscillations. In turn, the signature of the magnetooscillation can be used to find the ratio of spin and Landau splitting. This is often referred to as the coincidence method. We demonstrated that the spin splitting can exceed the Landau splitting by up to a factor of five. In very large fields, we could show that the coincidence of levels is avoided by the system: an anticrossing takes place. In the simplest model, the ratio between spin and Landau splittings is defined by the tilt angle only, thus the coincidence situation is constant over the whole magnetic field range. In the experiment, the situation is more complex. A crossover between different coincidence situations can be observed at constant angle. Samples with different carrier densities show different characteristics in this respect, indicating that the band non-parabolicity in InAs is responsible for this effect. At large magnetic fields tilted nearly parallel to the sample, a decrease in electron density is detected, the origin of which remains largely unclear.

In InAs/AlSb quantum wells, as well as in some other materials, theory predicts a spin splitting even at zero external magnetic field [Schulz96]. The main contribution to this is due to an electric field in the direction of the sample normal, induced by unequal distribution of donor sites on both sides of the well. For electrons moving in the sample with the Fermi velocity, this field translates into an effective magnetic field, leading to a lifting of the spin degeneracy. Many authors have reported to see this effect, which manifests itself in a beating pattern of the magnetooscillations. We have found an indication of these beats only in one sample, while their absence strikes as odd in many

other experiments[Brosig99]. Chapter 6 has all the details about the presence or absence of the zero-field spin splitting.

With the application of hydrostatic pressure to the crystal, the lattice constant can be decreased by a small amount. This generally increases the band gap of the semiconductor. Intuitively, this is clear because the existence of the gap depends on the interaction of the individual atoms, and as they are pressed closer together, the overlap of the atomic orbitals is increased. Much work has been done to study the band alignment in InAs/GaSb quantum wells, where the valence band in the GaSb is higher than the InAs conduction band, at zero pressure. This can be inverted by the application of pressure [Beerens87, Claessen86]. Bulk InAs and AlSb under pressure have been investigated for a long time [Shubnikov76, Stroessner86]. Chapter 7 describes experiments with InAs/AlSb quantum wells under hydrostatic pressure. Pressure up to 15 kbar, or 1.5 GPa, can be applied with in a pressure cell using an inert liquid as the pressure transmitting medium. Pressure generally decreases the carrier density in the quantum well. The rate of density decrease for different samples is measured and allows insight into the donor mechanisms that contribute to the carrier density. The fascinating aspect of hydrostatic pressure as a tool for investigating semiconductor structures is that it allows a direct change of the material parameters, while leaving the general layout of the system unchanged. One of the drawbacks, however, is that the pressure cannot be changed while the experiment is running: the pressure is changed outside of the cryostat under an hydraulic press, and the arrangement has to be re-cooled for each new pressure value.

In AlGaAs/GaAs heterostructures, it is possible to increase the number of carriers at low temperatures by illuminating the sample with a short flash from an LED, the carriers generated by this stay even after the light is switched off. Some InAs/AlSb quantum wells exhibit the opposite effect: the carrier density is persistently *lowered* by exposure to light. Sometimes the persistency is not perfect. Slow transport processes take place so that, on a time scale of minutes to hours, the carrier density creeps back up. In chapter 8 an account of the experiments with illumination is given.

From a general point of view, several types of nanostructures made out of InAs could provide insight into fascinating physics: because of the strong spin effects, new devices have been proposed, such as the spin transistor, that was proposed years ago [Datta90], and apparently has been realized for the first time recently [Gardelis99]. The behaviour of Aharonov-Bohm rings [Arahanov59] out of InAs in the presence of strong spin-orbit interaction effects

might lead to the unambiguous detection of interference effects due to Berry's phase [Berry84, Morpurgo98]. The principal question of 'gateability' has been adressed in many studies [Werking90, Rahman98, Symons98] but is not finally settled. For experiments, the pressure method is interesting and proves to be the most reliable method of changing the pressure, but it is a slow method that of course forbids taking direct technological advantage. That is to say: hydrostatic pressure will remain a powerful method for basic research.

Chapter 2

Two-Dimensional Electron Systems

This chapter deals with fundamental properties of electrons in two dimensions. This configuration is the one in which all of the experiments presented here are based on. The configuration is two-dimensional in a sense that movement is more or less free in two directions (i.e. only influenced by the crystal and its properties), and confined in the third direction. This is usually denoted the z direction, electron motion is possible in the (x, y) -plane. There is, of course, a finite extent of space available for electrons even in the z direction, but with a degree of freedom much reduced, in the extreme case to just one quantized state.

2.1 Basic Properties

A uniform two-dimensional conductor, one that can be envisioned for the moment as a large but thin sheet of some conductive material, has one peculiar property: the resistance of the system, measured from one point of the sheet to another, does not depend on the distance of the two points, at least as long as the points are not too close to the edge of the sheet. According to Drude's theory (see, e.g., [Ashcroft76]) electrons in a conductor are accelerated in an electric field until they bump into something that is in their way, they shoot off in an arbitrary direction and have to be accelerated again. In this manner, electrons bear a current from one end of the conductor to the other. The Drude scattering time τ_D is the average time between two such collisions, and can be computed from the conductivity σ_0 of a piece of such a sheet of: $\sigma_0 = \tau_D N_s e^2 / m_e$, N_s being the density of electrons per unit area in the sheet and m_e their mass. The *mobility* of electrons in the material is defined as $\mu = 1/\rho_0 N_s e$, where ρ_0 is the resistivity, $\rho_0 = 1/\sigma_0$. The mobility is a measure for how often the electrons get scattered in the material, since μ is proportional to τ_D . When a magnetic field is applied perpendicular to the

sheet, the Lorenz force acts on moving electrons and a Hall electric field builds up perpendicular to the current flow and the magnetic field. The magnetic field breaks the rotational symmetry, and thus the conductivity is no longer a scalar but a tensor. Ohm's law becomes a vector equation:

$$\mathbf{j} = \boldsymbol{\sigma} \cdot \mathbf{E}.$$

$\boldsymbol{\sigma}$ is now a magnetic-field dependent quantity:

$$\boldsymbol{\sigma} = \frac{\sigma_0}{\omega_c \tau_D} \begin{pmatrix} 1 & -\omega_c \tau_D \\ \omega_c \tau_D & 1 \end{pmatrix} = \begin{pmatrix} \sigma_{xx} & -\sigma_{xy} \\ \sigma_{xy} & \sigma_{xx} \end{pmatrix}. \quad (2.1)$$

The inverse of $\boldsymbol{\sigma}$ is the resistivity tensor $\boldsymbol{\rho}$:

$$\boldsymbol{\rho} = \rho_0 \begin{pmatrix} 1 & -\omega_c \tau_D \\ \omega_c \tau_D & 1 \end{pmatrix} = \begin{pmatrix} \rho_{xx} & -\rho_{xy} \\ \rho_{xy} & \rho_{xx} \end{pmatrix}. \quad (2.2)$$

where we have expressed the magnetic field B by the cyclotron frequency ω_c , the rate at which electrons go around in circles in a magnetic field: $\omega_c = eB/m$. For the components of $\boldsymbol{\sigma}$ and $\boldsymbol{\rho}$, the following relations hold:

$$\begin{aligned} \rho_{xx} &= \frac{\sigma_{xx}}{\sigma_{xx}^2 + \sigma_{xy}^2}, & \rho_{xy} &= \frac{-\sigma_{xy}}{\sigma_{xx}^2 + \sigma_{xy}^2}, \\ \sigma_{xx} &= \frac{\rho_{xx}}{\rho_{xx}^2 + \rho_{xy}^2}, & \sigma_{xy} &= \frac{-\rho_{xy}}{\rho_{xx}^2 + \rho_{xy}^2}. \end{aligned} \quad (2.3)$$

2.1.1 Confinement in one Dimension

An electron, or indeed any particle that is confined in one dimension between infinitely high barriers, can only assume discrete energy values.

$$E_i = \frac{\hbar^2}{2m_0^*} \frac{\pi^2}{a^2} i^2, \quad i = 1, 2, \dots, \quad (2.4)$$

with a being the distance between the barriers. The wave functions belonging to these energy values are sinusoidal functions which vanish at the ends of the well and have $i - 1$ nodes. This kind of arrangement is often called a *quantum well* (QW). In real physical situations the confining potential is always finite. The wave functions then are able to penetrate somewhat into the barriers, and there is only a finite number of states with discrete energy and the particle *bound* to the QW. For low-lying energy states, where E_i is well below the barrier height, the deviation from (2.4) is negligible. In most cases within this

thesis all the electrons in a QW populate the lowest energy level in the confined z direction only. For most intents and purposes the confinement energy is then a constant and motion in the z direction is completely quantized. The details of how the barriers work in semiconductor QW structures are explained in chapter 3.

2.1.2 Motion in two Dimensions

Thus our situation is a system of electrons that can move about freely, but only in two dimensions. As a consequence of the fact that there are a lot of electrons around, and each one of them must be in a distinct state (according to the Pauli principle), of \mathbf{k} -vector and spin, all states with energy lower than the Fermi energy E_F fill up. With the number of electrons per unit area being N_s , and k_F the magnitude of the wave vector for electrons that have the Fermi energy (those that populate the ‘Fermi edge’), the following relations hold:

$$k_F = \sqrt{2\pi N_s}, \quad E_F = \pi \frac{\hbar^2}{m^*} N_s. \quad (2.5)$$

The 2D density of states (DOS) can be calculated from (2.5), and amounts to

$$\rho(E) = \frac{dN_s}{dE} = \frac{m^*}{\pi \hbar^2} \quad (2.6)$$

This density of states does not depend on energy: this is only so for electrons in two dimensions. There is a constant number of electrons in any interval below E_F . Around E_F the distribution is governed by the Fermi distribution. Electron densities in our samples usually range from $4 \cdot 10^{15} \text{ m}^{-2}$ to $1.3 \cdot 10^{16} \text{ m}^{-2}$, thus the Fermi energy lies between 32 meV and 100 meV, for $m^* = 0.03m_e$.

2.2 Electrons in a magnetic field

2.2.1 Perpendicular Field

When a magnetic field is applied along the normal vector of the plane the electrons are confined to, travelling electrons are confined to orbits because of the Lorenz force acting on them. The Hamiltonian for electrons in a magnetic field can be written as

$$\mathcal{H} = \frac{(\mathbf{p} + e\mathbf{A})^2}{2m} + sg\mu_B B + V(z). \quad (2.7)$$

The first term is the kinetic energy of a charged particle in a magnetic field, the second term is the spin energy, and $V(z)$ is the external confining potential.

It is useful to apply the Landau gauge $\mathbf{A} = (0, xB, 0)$. The magnetic field \mathbf{B} calculated from this is along the z direction: $\mathbf{B} = \nabla \times \mathbf{A} = B\mathbf{e}_z$.

The spin quantum number s commutes with \mathcal{H} and can be separated off. Furthermore, \mathcal{H} does not contain x or z explicitly, which is why the wave function can be split like

$$\psi(x, y, z) = e^{\frac{i}{\hbar}(p_x x + p_z z)} \chi(y) \quad (2.8)$$

The y -dependent part $\chi(y)$ of the wave functions is given by harmonic oscillator functions:

$$\chi_n(y) = i^n (2^n! \sqrt{\pi} l)^{1/2} \cdot H_n\left(\frac{x}{l}\right) \exp\left(-\frac{x^2}{2l^2}\right), \quad (2.9)$$

where $H_n(x/l)$ are Hermite polynomials of order n and l is the magnetic length: $l = \sqrt{\hbar/eB}$. Motion in the z direction is suppressed by the vertical confinement, which leads to additional quantization with states E_i . The result can be expressed like a harmonic potential in y , so the resulting energy eigenvalues are

$$E_{i,n,s} = E_i + \hbar\omega_c \left(n + \frac{1}{2}\right) + \frac{1}{2}sg\mu_B B. \quad (2.10)$$

n is the Landau quantum number ($n = 0, 1, \dots$), s is the spin quantum number ($s = \pm 1$). The Zeeman splitting $g\mu_B B$ is usually much smaller than the cyclotron energy, in the case of InAs, where the g factor is large ($g = 14$ in bulk InAs), $\hbar\omega_c$ is about five times the Zeeman splitting. The characteristic energy $\hbar\omega_c$ is called the cyclotron energy, with ω_c the cyclotron frequency:

$$\omega_c = \frac{eB}{m^*}.$$

The wave functions associated with the states (2.10) are plane waves in y -direction, with wave vector x_0/l^2 , and standing waves in x -direction. x_0 is known as the centre coordinate, $x_0 = \hbar k_y/m\omega_c$. This gives the location of maximum probability density of the electron. The spatial extent of the wave function is described by the magnetic length l .

Each of these levels is highly degenerate. But their degeneracy is finite: a piece of sample of finite size L can take states with quantum numbers up to N_L ,

$$k_y = \frac{2\pi}{L} N_L,$$

if the centre coordinate x_0 is to stay within L . We have

$$L = \frac{\hbar \frac{2\pi}{L} N_L}{m^* \omega_c}.$$

Per unit area there are

$$N_L = \frac{e}{h} \cdot B \quad (2.11)$$

states available. So, as the field increases the distance between the levels goes up (2.10), decreasing the number of levels below the Fermi edge, while the number of electrons each level can accommodate increases accordingly (2.11).

2.2.2 Tilted Field

If the magnetic field is no longer parallel to the sample normal, the situation is more complex. The initial equation for the Hamiltonian is again (2.7), we follow Maan[Maan84] in this calculation. Let the magnetic field be in the (x, z) -plane. For there is translational symmetry, y can be split off the wave functions: $\Psi(x, y, z) = e^{ik_y y} \Psi(y, z)$. Substituting this into(2.7), and using

$$x' = x + \frac{\hbar k_y}{e B_z}, \quad (2.12)$$

which is possible as long as B_z does not vanish, we get

$$\left[\frac{\hbar}{2m^*} \left(\frac{\partial^2}{\partial x'^2} + \frac{\partial^2}{\partial z^2} \right) + \frac{e^2}{2m^*} (x' B_z - z B_x)^2 + V(z) \right] e^{ik_y y} \Psi(x, z) = E e^{ik_y y} \Psi(x, z). \quad (2.13)$$

This Hamiltonian does not depend on k_y , which means that all eigenfunctions with different k_y share one eigenvalue. The degeneracy of these levels is the same as for the perpendicular field: the argument of the previous section holds unchanged.

The cyclotron energy too, depends only on the perpendicular field, if the system is strictly 2D. In systems with more than one occupied subband, this relation only holds for sufficiently small angles. When the tilt angle approaches 90° , mixtures between different states lead top a more complex energy structure [Ando79, Oelting88].

2.2.3 Density of States in a Landau-quantized 2DEG

In an actual sample which is not really an ideal crystal, the lifetime of the states (2.10) is limited, and the energy peaks become broadened. Different scattering scenarios yield different shapes for the broadening, but often it is sufficient to consider a Gaussian broadening.

The Landau level width can be assumed to be $\Gamma = \hbar/\tau_Q$, with the quantum scattering time τ_Q . This scattering time is different from the Drude scattering

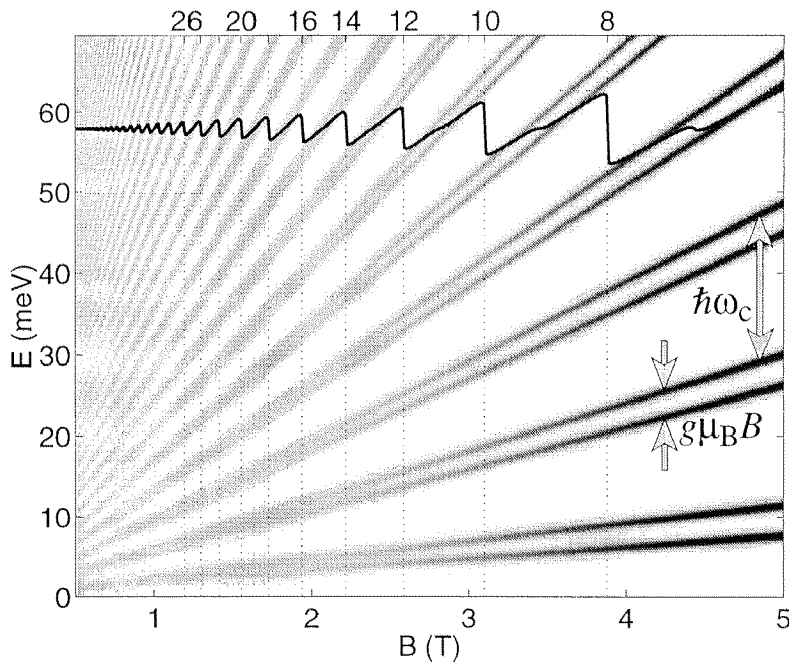


Figure 2.1: Density of states, given as grayscale, dark representing a maximum in DOS. The black line is the Fermi energy, which always lies in the lowest partially-filled Landau level. The arrows mark the size of the Landau splitting and the Zeeman splitting. The numbers given above the plot are filling factors: they count the number of Landau levels below E_F .

time out of (2.1). Even scattering events that change the direction of propagation by a small angle only, destroy the coherence of the electron and thus contribute to τ_Q . For τ_D , small angle scattering does not play a role (τ_D is therefore also referred to as the transport scattering time). Figure 2.1 shows the density of states represented as grayscale, with dark representing a maximum in the DOS. Parameters are: $N_s = 7.5 \cdot 10^{15} \text{ m}^{-2}$, $\tau_Q = 1 \text{ ps}$, Gaussian broadening, $g = 14$. A detailed account on the calculation is given in section 2.4. The Fermi energy at low fields is constant, as the field is increased such that the levels do no longer overlap, E_F follows the lowest Landau level that is partially occupied. Whenever the field increases such that this level is emptied, as the lower-lying ones increase their degeneracy, E_F drops into the next one down.

Properties of the system such as the conductivity and the magnetization are influenced by the DOS at the Fermi edge: As the magnetic field changes, minima occur in the conductivity each time E_F slips to another level. Since $N_L \propto B$, these minima are periodic in $1/B$ always. The oscillations of the conductivity are referred to as Shubnikov-de Haas- (SdH-) oscillations.

At finite temperature, the smeared-out Fermi edge can obscure effects of the modulated DOS: the oscillatory behaviour only appears if the gaps in between individual levels exceed the thermal broadening sufficiently. This leads to a strong temperature-dependence in the depth of the oscillations, which can be exploited to determine the size of the gap: refer to sections 4.6 and 5.4 for details.

2.2.4 Conductivity in weak magnetic fields

How much current can the DOS contribution from a Landau level support? The conductivity of a 2DEG can be described by $\sigma = e^2 \mathcal{D} D(E_F)$, where \mathcal{D} is the diffusion coefficient and $D(E_F)$ the density of states at the Fermi level, as described e.g. in [Kawaji94]. Based on the assumption of a semi-elliptic shape of one broadened Landau level, the conductivity for a Landau level with Landau index n is

$$\sigma_{xx}(n) = \frac{2e^2}{\pi^2 \hbar} \left(n + \frac{1}{2} \right). \quad (2.14)$$

Theorists (among many other works, refer to [Ando82, Laihkhthman94]) have figured out in detail what the magnetoconductivity looks like. This involves calculating the DOS $D(E)$ with some specific broadening function, making an expansion in terms of $\cos(2\pi E/\hbar\omega_c)$ (this reflects the $1/B$ -dependence), and working out the thermal broadening by integrating the $D(E)$ over $-df/dE$, the negative derivative of the Fermi function. The result, as derived in [Laihkhthman94], is

$$\rho_{xx} = \frac{1}{\sigma_0} \left(1 - 4 \cos \left(2\pi \frac{\hbar N_s}{2e B} \right) \frac{2\pi^2 \frac{k_B T}{\hbar\omega_c}}{\sinh \left(2\pi^2 \frac{k_B T}{\hbar\omega_c} \right)} e^{-\frac{\pi}{\tau_Q \omega_c}} \right). \quad (2.15)$$

The $\cos(\dots)$ term is the $1/B$ -periodic oscillating term. This allows to determine the electron density from an experimental curve. The temperature-dependent term allows a determination of ω_c , and thus the effective mass. Once this is known, with the exponential term containing the scattering time and the cyclotron energy, τ_Q can be determined.

2.3 Quantum Hall Effect

From equations (2.1, 2.3), it follows for the transverse conductivity

$$\sigma_{xy} = -\frac{N_s e}{B} + \frac{\sigma_{xx}}{\omega_c \tau_D} \quad (2.16)$$

holds. Now, let us lower the temperature and switch on the strong magnetic field, such that $\hbar\omega_c$ exceeds $k_B T$ by far, and tune the magnetic field to an exact filling factor, where one Landau Level is just filled. There are no electrons available for transport since they would have to cross the big gap $\hbar\omega_c$ to find another state to be transported into,¹ which they cannot for it's too cold. σ_{xy}

¹We are neglecting spin splitting for the moment, without loss of generality for the argument that follows.

then reads:

$$\sigma_{xy} = -\nu \frac{e^2}{h}, \quad \text{where } \nu = 1, 2, \dots \quad (2.17)$$

Now, let us consider a real sample which has in the crystal lattice foreign atoms, lattice faults and such like. This will form random potential fluctuations for the electrons.

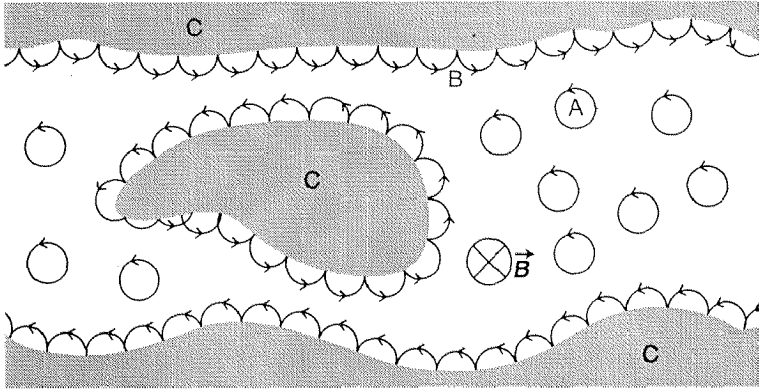


Figure 2.2: Classical skipping orbits. Electrons are localized in the middle of the sample (A), but can travel from one end to the other at the edge, where the potential rises above the Fermi level (grey areas C), on skipping trajectories (B).

The magnetic field is so strong that the magnetic length is a lot shorter than the size of the random potential fluctuations. The magnetic field pushes the electrons sideways with respect to their path. Classically, the electrons can only move on circular trajectories now. When the local potential is higher than an electron's energy it cannot penetrate any further but bounces off, it performs *skipping orbits* as shown in Figure 2.2.

In effect, the magnetic field drives it *along equipotential lines*. There are many electrons that are trapped on a hill and go around at the edge all the time. There may be others that are trapped in a puddle, on the hill: they go around in circles the other way. There is *one* channel, along the edge, that extends from one end of the sample to the other: here electrons can actually contribute to transport. The longitudinal conductivity is zero, but that does not mean there is no current: just the voltage drop is across the sample not along the edge, because of the peculiarities of equations (2.3) in a strong magnetic field.

The surface in Figure 2.3 displays the local potential in one, say the topmost, occupied Landau level. In addition to the energy $\hbar\omega_c(n + \frac{1}{2})$, there is the random long-range fluctuations, plus the abrupt rise at either edge of the Hall bar. Equipotential lines are marked. The white line is the transport-carrying channel, dashed lines are higher LL's, and the black solid lines are lower-lying LLs, which do not connect both ends of the sample. Now imagine several of the shapes in Fig. 2.3 stacked below the one that is there, spaced by $\hbar\omega_c$ in energy. These be the lower-lying Landau levels: there is always a path at the edge that goes through the Fermi energy, as the dashed lines do in Fig 2.3.

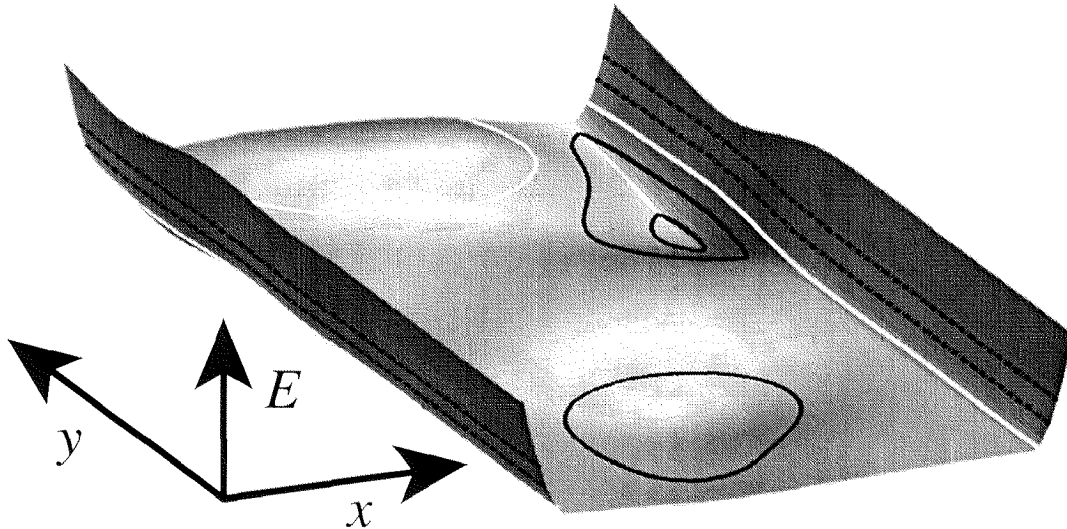


Figure 2.3: A simple model potential landscape to help visualize how electrons can move in the QH regime. White line: Fermi energy. Dashed lines: higher LLs. Black solid lines: completely filled levels.

When the Fermi energy is changed by a small amount, by putting in more electrons, the transport does not change at all: the number of current-carrying channels does not change. The number of current channels only changes when a new Landau level makes a connected channel from end to end of the sample. The quantized Hall resistivity comes out to be

$$\rho_{xx} = \frac{h}{2e^2} \cdot \frac{1}{\nu} = 25.812807 \text{ k}\Omega \cdot \frac{1}{\nu} \quad (2.18)$$

ν is called the filling factor: the number of completely filled Landau levels below the Fermi energy. The resistance quantum $h/2e^2 \sim 25.8 \text{ k}\Omega$, sometimes called a *Klitzing*, can be determined from quantum Hall samples exactly within 1 part in 10^7 . Today, it is used as a resistance standard for calibration purposes. Within this study, the plateaux in ρ_{xy} have been used to calibrate the current through the sample.

2.4 Model Calculation for the magnetoresistivity from the Landau-quantized density of states

In order to incorporate more details of the underlying physics, it can be useful to do a numeric model calculation of transport phenomena. The procedure has often been described in the literature [Gerhards76, Gobsch88]. For this study, we have implemented the model in MATLAB, and used it in various places. Once the basic equations, mainly (2.10) and (2.14), have been implemented,

it is easy to modify the model to incorporate all kinds of details to get a grip on experimental findings by comparison to modelled curves.

Density of states

The model DOS is a sum of broadened Landau levels (LL). We take the spin-split Landau fan (2.10) and let each state contribute N_L (2.11) to the DOS:

$$D(E) = N_L \sum_{l,s} g(E_{ls}). \quad (2.19)$$

$g(E)$ is a broadening function centered around E , with typical width Γ and normalized to $1 = \int_{-\infty}^{\infty} g(E)dE$.

To determine the position of the Fermi energy, we need to figure out how many levels, counting from the lowest energy upwards, are needed to accommodate all electrons, i.e. $\int_0^{E_F} D(E)dE = N_s$ has to be solved. Doing this and using the above expression for the density of states, one finds that for sufficiently narrow LLs, E_F jumps sharply once one LL is filled and the next one up is separated by a gap in Energy with no states at all. This leads to modelled ρ_{xx} curves that have sharp minima and round maxima, unlike they are ever seen in an actual experiment. To account for localized states that do not contribute to transport but let E_F vary smoothly between LLs, a constant DOS background[Gobsch88] is added, and compensated for in a lower DOS contribution of each level. The parameter x ($0 < x < 1$) adjusts the amount of constant background DOS:

$$D(E) = (1 - x)N_L \sum_{l,s} g(E_{ls}) + x \frac{m^*}{\pi \hbar^2} \quad (2.20)$$

In Figure 2.1 the density of states is displayed together with E_F . It can be seen that E_F hardly varies at all where individual LLs overlap strongly. Here, the self-consistently calculated value for E_F may safely be replaced by the zero-field value $E_F = \pi \hbar^2 / m^* N_s$. It has been verified that this may alter slightly the shape of the calculated ρ_{xx} oscillations, while the oscillation amplitude remains unchanged. This is because in the case of DOS minima and maxima, E_F crosses the value for $B = 0$ (equation 2.5) exactly. To evaluate the oscillation amplitude for comparison with experiments, the self-consistent determination of the Fermi energy, together with the constant background DOS, can be skipped.

Conductivity

To calculate σ_{xx} from the density of states, the integral

$$\sigma_{xx} = \frac{e}{\hbar} \int -\frac{df}{dE} \cdot N_L \sum_{l,s} g(E_{ls}(n + 1/2)) dE \quad (2.21)$$

has to be evaluated[Ando74a]. The resistivity can be worked out using relations (2.3), and assuming $\sigma_{xx} = eN_s/B$, which is the classical expression and valid to good accuracy in small and intermediate fields.

Evaluation

Individual LLs have been modelled with semielliptic, Lorentzian, and Gaussian shapes. Lorentzian curves have a relatively strong tail, that make the calculation either unprecise or inefficient. The semielliptic function yields results that are discontinuous. For most calculations, we have used the Gaussian shape, otherwise the Lorentzian has been employed. Using the B -dependent expression

$$\Gamma = \sqrt{\hbar^2 \omega_c / 2\pi\tau_Q} \quad (2.22)$$

for the Landau level width, which has originally been derived in the SCBA for silicon MOSFETS[Ando82], the oscillation amplitude of the resulting ρ_{xx} trace is linear in the Dingle plot (see section 4.7 for a description of Dingle plots).

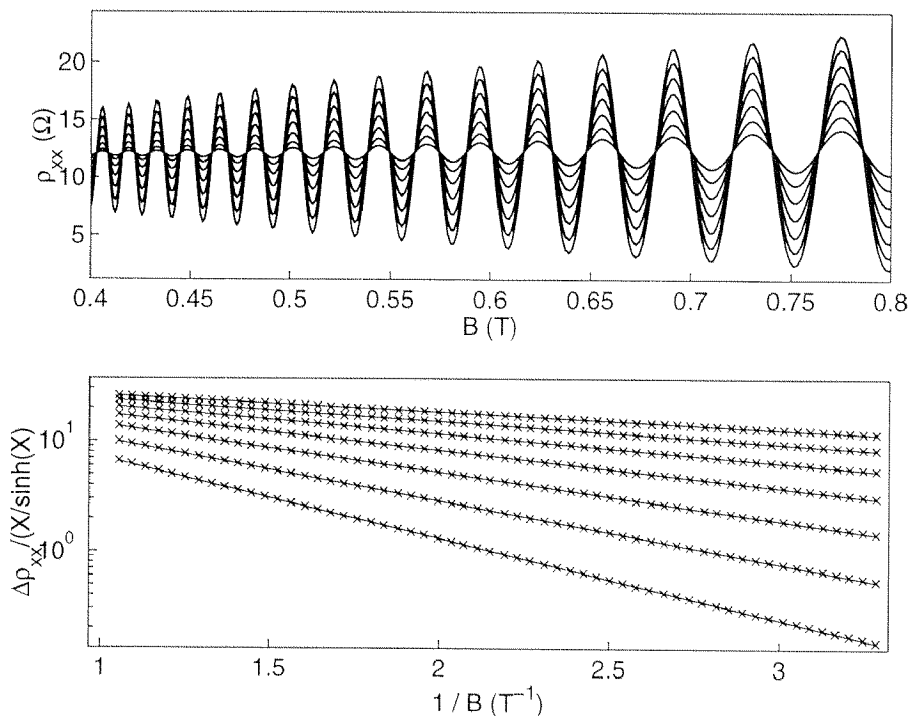


Figure 2.4: Top: Calculated ρ_{xx} traces for various values of the Landau level width. Bottom: the associated Dingle plots. Expression (2.22) was used for the level broadening. This leads to a B -dependence of the amplitude as predicted by (2.15), even though the absolute value of τ_Q comes out different.

In the upper half of Figure 2.4, calculated ρ_{xx} traces are given using the parameters $N_s=6.18 \cdot 10^{15} \text{m}^{-2}$ and $T=1.7 \text{K}$, while varying τ_Q between 0.2 ps and 1 ps. From the slopes of the Dingle plots in the lower part we can extract values for τ_Q like it has been done in many experiments. The resulting τ_Q is larger than the one put into the calculation through equation (2.22) by a factor of 1.5, for a wide range of parameters.

However, using a constant LL width $\Gamma = \hbar/\tau_Q$, the result of the model calculation does not fit to a line in the Dingle plot. Consequently, the τ_Q derived from the local slope of a Dingle plot varies with the range of magnetic field used.

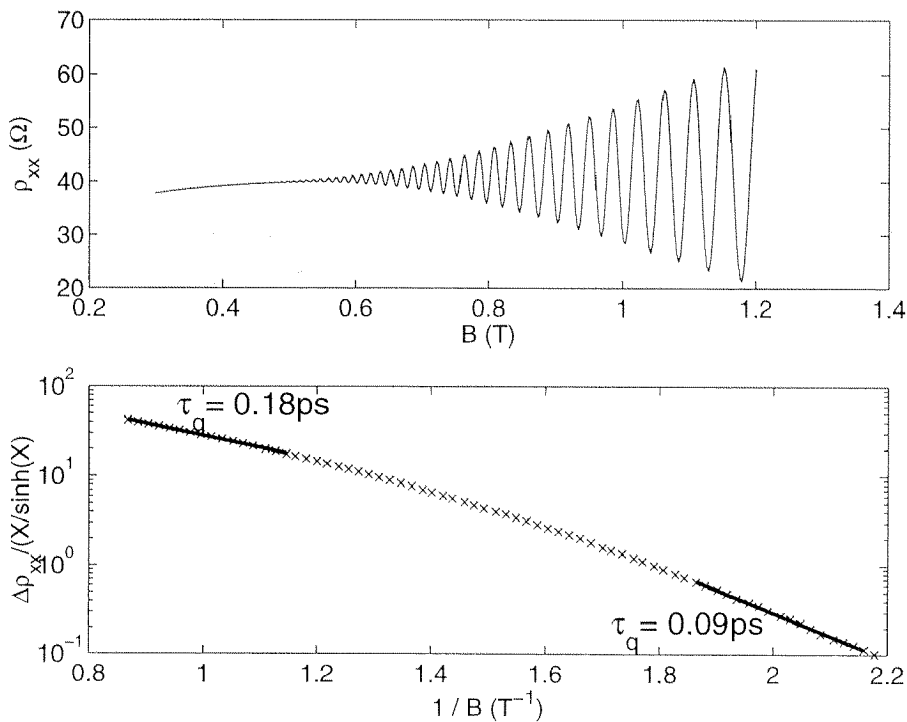


Figure 2.5: Top: Calculated ρ_{xx} trace. Bottom: the associated Dingle plot. A constant Landau level width $\Gamma = \hbar\tau_Q$ was assumed, with $\tau_Q=0.5 \text{ps}$, for the Gaussian level broadening. The Dingle plot does not show the expected linear behaviour, and the resulting τ_Q values are too small.

Figure 2.5 shows a calculated ρ_{xx} trace for $\tau_Q=0.5 \text{ps}$, all other parameters as above, and the corresponding Dingle plot, evaluated at either end of the B range. The resulting τ_Q ranges from 0.09 ps to 0.18 ps, which is far from satisfactory. Many experimental ρ_{xx} traces in InAs, however, do not come out with a straight line in the Dingle plot either. In InAs, at large densities, the Landau ladder may have severely bent rungs, from nonparabolicity, and a quantitative analysis of τ_Q by means of equation (2.15) is dubious.

The temperature dependence of the calculated ρ_{xx} amplitude is analyzed in Figure 2.6. We have modelled ρ_{xx} traces for $T = 0.5 \dots 8 \text{K}$, and used the mechanism described in section 4.6 to get back the mass. Input parameters: $\tau_Q=0.3 \text{ps}$, $N_s=4.4 \cdot 10^{15} \text{m}^{-2}$, $g=14$. Using Lorentzian Landau level shape, the resulting m^* is consistently equal to the input m^* , independent of other pa-

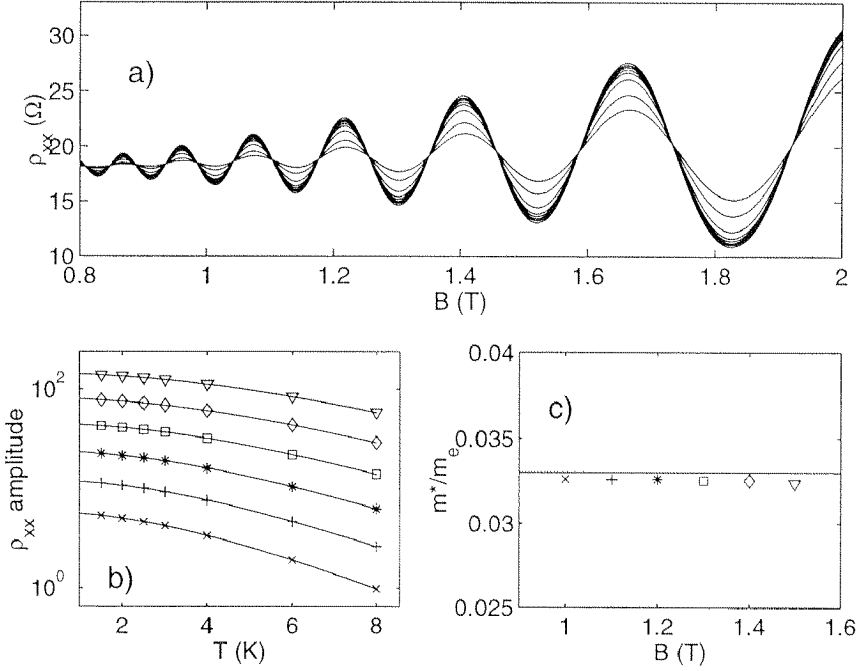


Figure 2.6: a) Calculated ρ_{xx} traces for temperatures between 0.5K and 8K. b) Amplitude of the curves in a) as a function of temperature, for several fixed magnetic fields (symbols) and fits of the temperature term to that data. c) Evaluation of b) in terms of the effective mass. The symbols in b) and c) correspond. The line marks the ‘input’ m^* ($=0.033m_e$) for a).

parameters such as N_s , τ_Q , or the fixed magnetic field where the evaluation takes place. The absolute value of the amplitude of ρ_{xx} , $\delta\rho_{xx}$ for short, is strongly dependent on the line shape used, but the temperature dependence yields the same effective mass, as can be seen in Figure 2.7. As long as $\delta\rho_{xx}$ is neither too small, nor so big that ρ_{xx} approaches zero in the minima, it follows the $X/\sinh X$ law from equation (2.15), where $X = 2\pi^2 k_B T / \hbar \omega_c$.

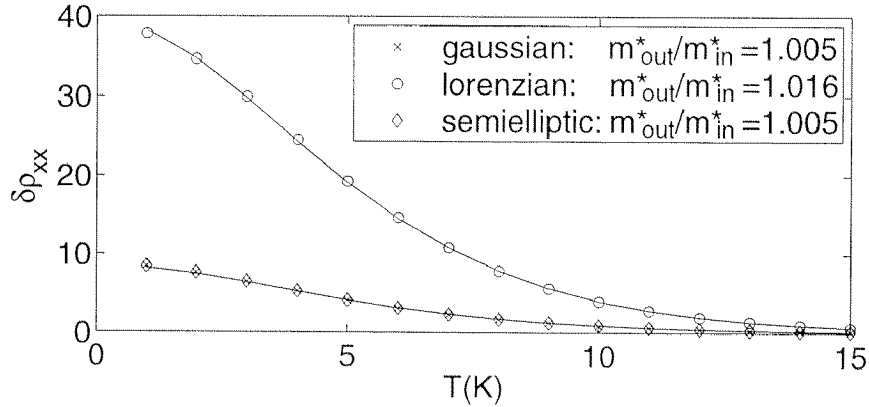


Figure 2.7: Calculated ρ_{xx} amplitude data and fits like in Figure 2.6 b), for three different Landau level shapes. For semielliptic and Gaussian shapes, the resulting amplitudes are essentially equal. All LL shapes yield the same mass value. The parameters were: $B=1\text{ T}$, $\tau_Q=0.3\text{ ps}$, $m^*=0.03 m_e$, $N_s=6.1 \cdot 10^{15}\text{ m}^{-2}$. No spin splitting was assumed.

For the rest of this section, a more detailed account of ‘computational experiments’ is given, which were undertaken to justify the use of a) the model calculation, and b) the methods for determining τ_Q and m^* from ρ_{xx} traces.

Figures 2.8 and 2.9 show an analysis of the resulting τ_Q from Dingle plots out of calculated ρ_{xx} traces, varying the shape of the Landau levels, and the expression used for the LL width.

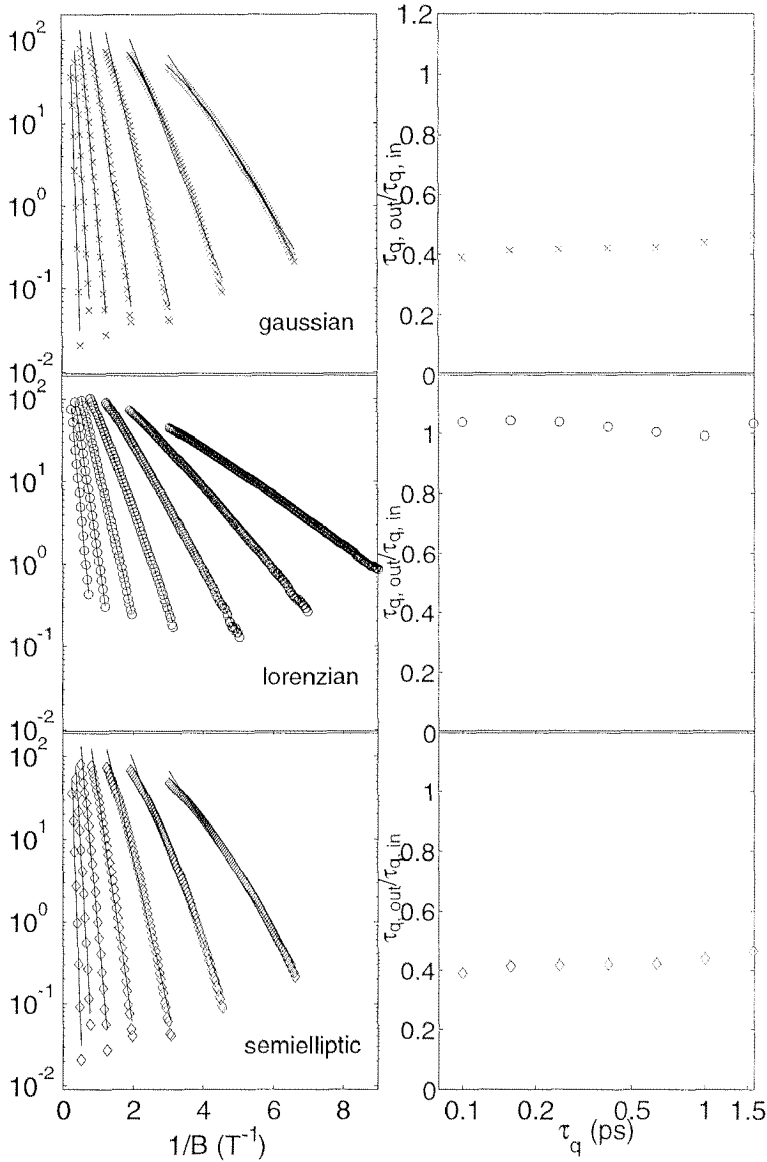


Figure 2.8: Comparison of different broadening functions, using $\Gamma = \hbar/\tau_Q$, and various τ_Q values from 0.1 ps to 1.6 ps. Left side: Dingle plots. Right side: ratio of output τ_Q and input τ_Q , plotted vs. input τ_Q , from the Dingle plot on the left. Only the Lorentz-shaped level broadening yields a linear Dingle plot, and the resulting τ_Q equal to the input τ_Q . The range of magnetic field was chosen in each case to include only the range where ρ_{xx} is sinusoidal.

Figure 2.8 assumes a constant LL width of $\Gamma = \hbar/\tau_Q$. Here, the resulting τ_Q values match the input τ_Q over the whole range. For Lorentzian Level broadening, this is convincing because each of the Dingle plots is linear, which means that the choice of the magnetic field range does not alter the result. With Gaussian and semielliptic broadening, the resulting τ_Q is considerably smaller, only about 0.4 of the input value, and the curved Dingle plots would yield different quantum scattering times for different ranges of B , as shown in Figure 2.5. The range of B for each τ_Q was chosen from the onset of oscillations, where $\omega_c\tau_Q = 1$ holds, up to where the amplitude is equal to $\rho_{xx}(B=0)$. Exceeding this would go beyond the semiclassical limit, because

ρ_{xx} comes close to zero in the minima.

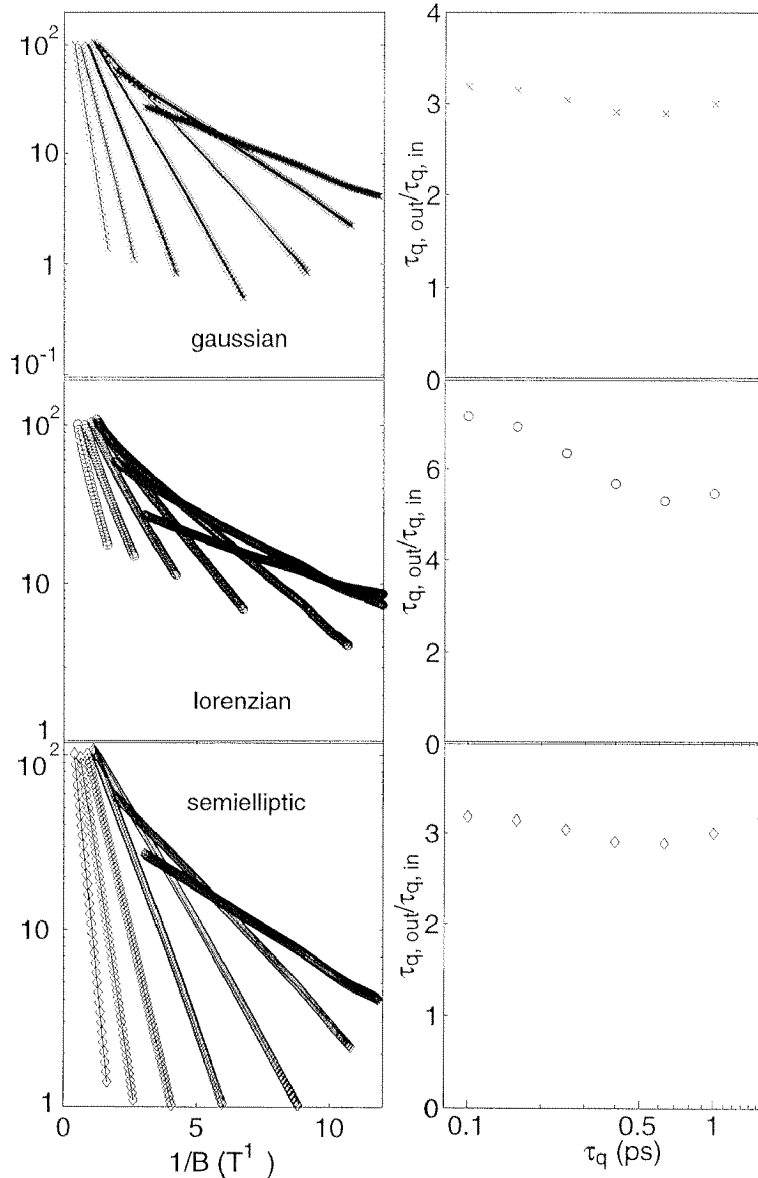


Figure 2.9: Comparison of different Broadening functions, using the \sqrt{B} -dependent LL width $\Gamma = (\hbar^2 \omega_c / 2\pi \tau_Q)^{(1/2)}$. Left side: Dingle plots. Right side: ratio of output τ_Q and input τ_Q , plotted vs. input τ_Q , from the Dingle plot on the left. All the resulting Dingle plots are roughly linear, but the altered definition of Γ yields completely different τ_Q values. With the Lorentzian broadening, the $\tau_{q, out}/\tau_{q, in}$ value varies with the input τ_Q . As in Figure 2.8, the range of magnetic field was chosen in each case to include only the range where ρ_{xx} is sinusoidal.

With the \sqrt{B} -dependent expression for the Landau level width, (2.22), the calculation yields linear Dingle plots for all choices of LL shape $\Gamma(E)$, as was already demonstrated in Figure 2.4. The \sqrt{B} -dependent LL width is derived in [Ando82] in the case of weak short-range scattering, where the range of the scattering potential matches the wavelength of the electrons. The resulting τ_Q values, however, are substantially different from the input value to the calculation, and, for the Lorentzian shape, the ration between input and output τ_Q varies over the range of values used.

In conclusion, the model can be used to understand the general features of SdH oscillations. A quantitative analysis of ρ_{xx} data in terms of the temperature dependence yields the size of the Landau gap $\hbar \omega_c$, or the effective mass. The precise shape of the levels plays no decisive role. The results presented

in section 5.4 extend the method to the case of tilted fields, including spin splitting.

The results concerning τ_Q are less convincing. The general trend behaves as expected, i.e. the SdH amplitude is decreased with decreasing τ_Q , so that a changing scattering behaviour can be measured with the use of this method. Numerical values of τ_Q from SdH amplitude have to be taken with a grain of salt.

Chapter 3

InAs/AlGaSb quantum wells

By far the most common material combination for quantum wells grown by molecular beam epitaxy (MBE) out of III-V semiconductor compounds is GaAs/AlGaAs. The technology is well-established and interfaces of very high quality are possible because a) the lattice-match of GaAs and AlAs is very good, and b) growth procedures have been subject to investigation for almost 30 years, starting from the infant years of MBE itself [Cho71]. There is a number of technical applications for these materials, fuelling research in the field. However, there is a number of other materials that can be used, and the InAs/AlGaSb material system for making quantum wells has certain specialities which accounts for the continuing attention that has been paid to it. This chapter explains the details of the InAs/AlSb samples used in this work.

3.1 Bulk materials

3.1.1 Indium Arsenide

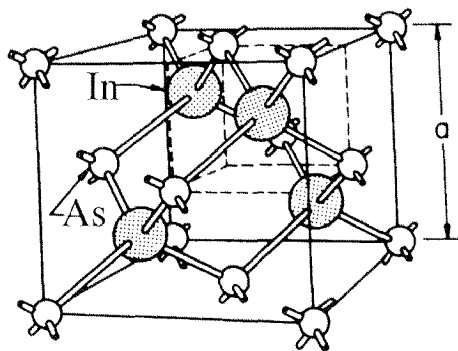


Figure 3.1: Schematic representation of the Zincblende crystal structure InAs as well as AlSb and most other III-V compounds crystallize in. Illustration from [Sze81].

Indium Arsenide is a narrow-gap III-V compound semiconductor. The fundamental band gap is 410 meV at room temperature. The effective mass for electrons at the conduction band edge is $0.023m_e$. Due to the small mass, the

electron mobility in bulk InAs is the second highest of all semiconductor bulk materials ($\mu = 3.3 \text{ m}^2/\text{Vs}$, only InSb having even higher μ).

InAs is a direct semiconductor: the smallest separation of valence band and conduction band is at $k = 0$. Because of the narrow band gap, the influence of adjacent bands is not negligible. Band structure parameters have been extracted from experimental data and calculations, and are summarized in [LB-tables].

Non-parabolicity

The effective-mass approximation is frequently used in GaAs and other semiconductors. If the effective mass is isotropic, the mass is just the reciprocal of the energy dispersion around the Γ -point:

$$\frac{1}{m^*} = \frac{1}{\hbar^2} \frac{\partial^2 E}{\partial k^2}. \quad (3.1)$$

As long as the dispersion is *parabolic*, m^* is just a constant. If k is no longer small, and other bands are close enough, as it is the case in InAs, interband interaction leads to a deformation of the parabolic band. In the expansion of the dispersion $E(k)$, terms of higher order have to be considered. The next simplest approximation after the parabolic is a *two-band model*, involving only the conduction band and the light-hole band [Kane57]:

$$E(k) = \frac{\hbar^2 k^2}{2m_e} \left(1 - \alpha \frac{\hbar^2 k^2}{2m_e} \right). \quad (3.2)$$

This can also be expressed in terms of an energy-dependent effective mass:

$$m^*(E) = m_0^* (1 + 2\alpha E) \quad (3.3)$$

where m_0^* is the band edge effective mass. In the two-band model the non-parabolicity parameter comes out as $\alpha = 1/E_g$, so that

$$m^* = m_0^* \left(1 + 2 \frac{E}{E_g} \right) \quad (3.4)$$

All physical quantities in InAs that contain the effective mass are now energy-dependent. In a 2D system, where electrons have an additional energy due to the 1-D confinement in the z direction, this has to be considered. In a magnetic field, the cyclotron energy is no longer the same for all Landau bands, so that the Landau-fan picture in Figure 2.1 gets curved instead of straight lines for the energy of Landau states as a function of the magnetic field.

3.2 MBE-grown InAs/AlSb quantum wells

3.2.1 Sample Growth

The technique of molecular beam epitaxy (MBE) was first developed in the late fifties and deployed by [Guenther58] to fabricate InAs and InSb Hall sensors. The fine art of growing high-quality III/V material became possible with the advent of IN_2 -cooled MBE machines and the possibility of in-situ layer analysis using Reflection high energy electron diffraction (REED) many years later. In principle an MBE machine is just a vacuum chamber where a substrate, usually a mechanically and chemically polished slab cut from a single crystal, is exposed to the vapor beams of various material components that sit in heated *effusion cells*, and the vapor beams can be switched on and off by means of shutters. Effusion cells are merely crucibles in which materials are evaporated from a melt (Ga, Al, In, Sb), or sublimated from the solid (As, Si). Much attention is paid to achieving the best possible vacuum, and ultimate purity of the elementary components in the effusion cells, so that the deposited material is free from defects to a degree that is superior to any other means of crystal growth. Also, because the rate of growth is comparatively low, typically one atomic layer per second, different materials can be deposited in layers with atomic precision by means of controlling the shutters.

MBE-growth of AlSb on GaAs (and GaSb) was first performed successfully by Chang et al. [Chang82] at IBM, Yorktown Heights in 1982. There is a large lattice mismatch between GaAs and AlSb: the lattice constant of AlSb is larger by 8.5%. Growing AlSb on GaAs starts off as three-dimensional growth and a smooth surface appears only after some tens of nanometres have been deposited.

All the samples used in this study were grown by MBE at the University of California, Santa Barbara, by Colombo R. Bolognesi, John English, George Tuttle, Chanh Nguyen and others in the group of Prof. Herbert Kroemer (Department of Electrical and Computer Engineering, Department of Materials). In this group, pioneering work has been done to achieve high-quality quantum wells out of this material system on (standard) GaAs substrates [Tuttle90b]. In order to achieve a reasonable surface quality, a thick buffer layer (1–2 μm) of GaSb and/or AlSb is grown after depositing an initial (“nucleation”) layer of AlSb (100 nm). To further reduce the amount of lattice defects, a superlattice is grown, usually with 10 or 20 interchanging layers of GaSb and AlSb, each 2.5 nm thick [Blank96]. Onto this, the bottom barrier of, say, 20 nm AlSb is deposited. The quantum well (QW) of InAs is then applied. For all the

samples studied here, it is 15 nm thick. The QW is covered by the AlSb top barrier, sometimes mixed with layers of GaSb, because AlSb (like AlAs) can not be grown in very thick layers with high surface quality. For very high electron concentrations, the AlSb is doped with Te, at a distance of ~ 50 nm from the top QW interface. Samples are capped with either GaSb or InAs, to ensure the chemical stability when exposed to air. InAs cap layers are grown so thin (5 nm), that no electrons can accumulate in it, i.e. there is no second quantum well at the surface.

After this procedure it is possible to obtain samples with high mobilities such as $61 \text{ m}^2/\text{Vs}$, as reported by Tuttle et al. [Tuttle89]. In these samples, the quantum hall effect beautifully demonstrated [Hopkins91].

Interface types

In a heterointerface between two binary compounds which do not share a component (like the arsenic in AlAs/GaAs), there are two possible interface types. When changing growth from AlSb to InAs, the interface can be either AlAs-like or InSb-like. These two materials have very different properties: to gain control over the interface type has been a key issue in obtaining the above-mentioned sample quality in the InAs/AlSb material system. Tuttle et al. [Tuttle90a] report that good electron mobility can only be achieved if the interface is grown InSb-like. A first-principles calculation of the different possibilities of stacking AlSb onto InAs (or vice versa) has been performed by [Ren97]. They found that with both interface types, it is energetically favourable to *switch* one atomic layer of cations, or anions. On the AlAs-like interface, the switch of one Indium and Aluminium layer has by far the largest energy lowering. It is suggested that this accounts for more roughness at an AlAs-like interface, in accordance with the experiment of Tuttle et al.

Bulk inversion (a)symmetry

The crystal structure of InAs is the Zincblende structure. The lattice constant as shown in Figure 3.1 is $a = 0.60584 \text{ nm}$. Inverting this structure in all three directions yields the same structure again, only rotated by 90° . Clearly, that does not change physical properties at all. When InAs is grown in a thin film on AlSb, the lateral axis is stretched by a small amount because the AlSb lattice constant is larger than the InAs lattice constant. At the same time, the lattice constant in the z direction will shrink a little. Now, the structure is no longer invariant under space inversion. This inversion asymmetry leads to an energy difference for electrons with different spins (See chapter 6).

Band offsets

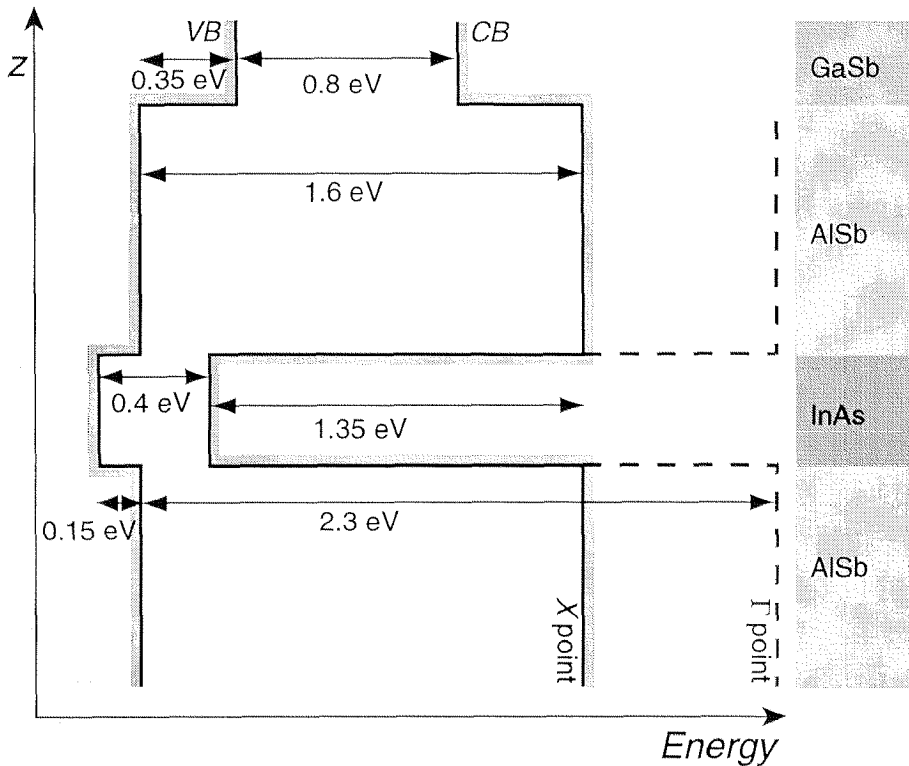


Figure 3.2: Layer sequence and band alignment of a typical InAs/AlSb quantum well. AlSb is an indirect semiconductor, the conduction band minimum is at the X point (solid line). The direct bandgap (at the Γ point, dashed line) is at a higher energy.

The band alignment between AlSb and InAs has been studied in [Nakagawa89]. Figure 3.2 shows most parameters for the material system in a simplified (flat-band) band alignment diagram. Symons et al. [Symons94] find the alignment parameter to vary by ~ 30 meV according to the interface type in GaSb/InAs superlattices.

3.2.2 Origin of the Quantum Well Electrons

In InAs/AsSb quantum wells grown without intentional doping, the quantum well is always filled with electrons. This is not the case with GaAlAs/GaAs structures. The question is: where do the quantum well electrons come from? If there were ionized impurities in the InAs well itself, they would give rise to strong short-range potential fluctuations and scattering rates that are incompatible with the high mobility of InAs/AlSb QWs. As an alternative source of electrons, three kinds of donors are suggested: a) deep donor levels in the non-intentionally doped AlSb barriers, b) surface states, and c) delocalized donors at the InAs/AlSb heterointerfaces. The experimental evidence for a) and b) is strong. The intrinsic carrier density in MBE-grown AlSb is too small to be measured directly. No shallow donors are available, and deep donors do not ionize into the conduction band. However, these levels can drain into the

very deep adjacent InAs well [Tuttle89]. The 2D electron density N_s in QW samples is always substantially lower in structures that are capped with InAs, in comparison with GaSb-capped samples.

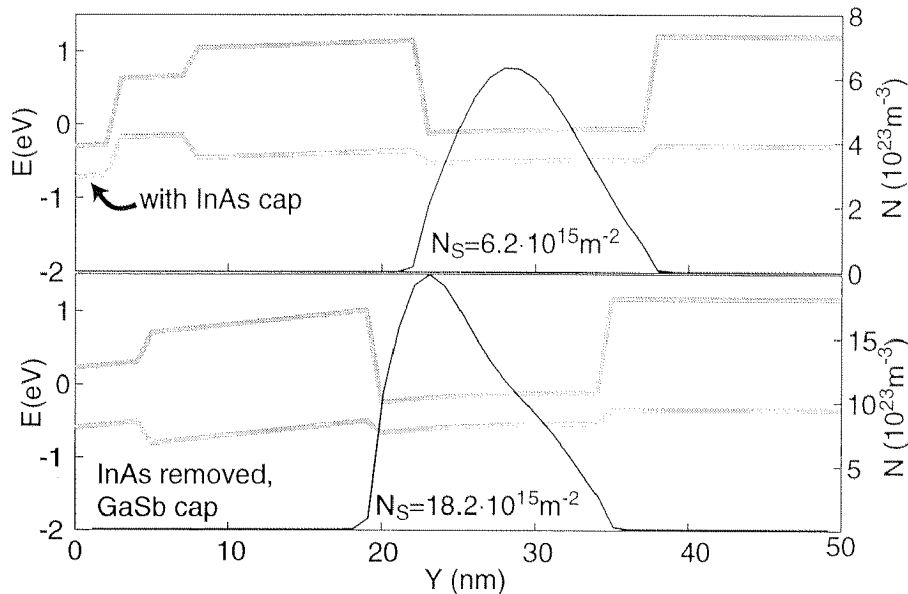


Figure 3.3: Simulation of the band structure in a sample similar to the experiment in [Nguyen93]. Grey lines: Conduction band, valence band (left axis, E_F is at $E = 0$). Black line: bulk electron density. Top: Sample with InAs Cap. Bottom: after removal of the InAs cap. The density is greatly increased.

A cunning experiment [Nguyen93] was performed to clarify this situation: samples with multiple cap layers were grown. Alternating GaSb (5 nm), AlSb (5 nm), and InAs (3 nm) for five times, a multi-capped sample had $N_s = 1.7 \cdot 10^{16} \text{ m}^{-2}$. Using selective etchants, the top GaSb/AlSb layer could be removed, after which the density went down to $N_s = 6.5 \cdot 10^{15} \text{ m}^{-2}$. After removing the InAs layer and exposing an InAs cap once more, the density went up again, though not quite to the original value. This procedure has been repeated five times. Thus the effect of different cap could be proved in one and the same sample.

The explanation for the different densities, depending on the cap layer material, is the different levels where the Fermi energy is pinned at the surface. This energy depends on the chemical termination of the cap layer. On the InAs surface, E_F is pinned $0.3 \pm 0.1 \text{ eV}$ above the conduction band edge of InAs, or, taking into account the band offset between InAs and AlSb, $1.1 \pm 0.1 \text{ eV}$ below the conduction band edge of AlSb. On the GaSb cap, The pinning is $0.18 \pm 0.03 \text{ eV}$ below the conduction band edge of AlSb. In Figure 3.3, a self-consistent band structure calculation [Snider90] for a similar sample is presented.

According to [Nguyen93], the value of 300 mV above the InAs CB is higher than that predicted by theory, which the authors attribute to residual antimony on the InAs surface exposed by the etching process. The antimony is verified to be present using surface-sensitive Auger electron spectroscopy. We have found that in InAs-capped samples the carrier density is increased substantially when

the surface is exposed to the liquid in a pressure cell. This is discussed in chapter 7 on pressure experiments.

The thickness of the top barrier is significant for the resulting carrier density as well. The farther the surface is away from the quantum well, the smaller is the effect of band pinning at the surface, because the ‘lever arm’ is longer. Consider the lower part of Figure 3.3: The carrier density is so high because the surface pinning of E_F forces the quantum well deep into the Fermi level. If the top barrier is thicker, the same pinning position leads to less pulling-down of the quantum well, and the number of carriers introduced into the well from the surface is reduced.

3.2.3 Magnetotransport

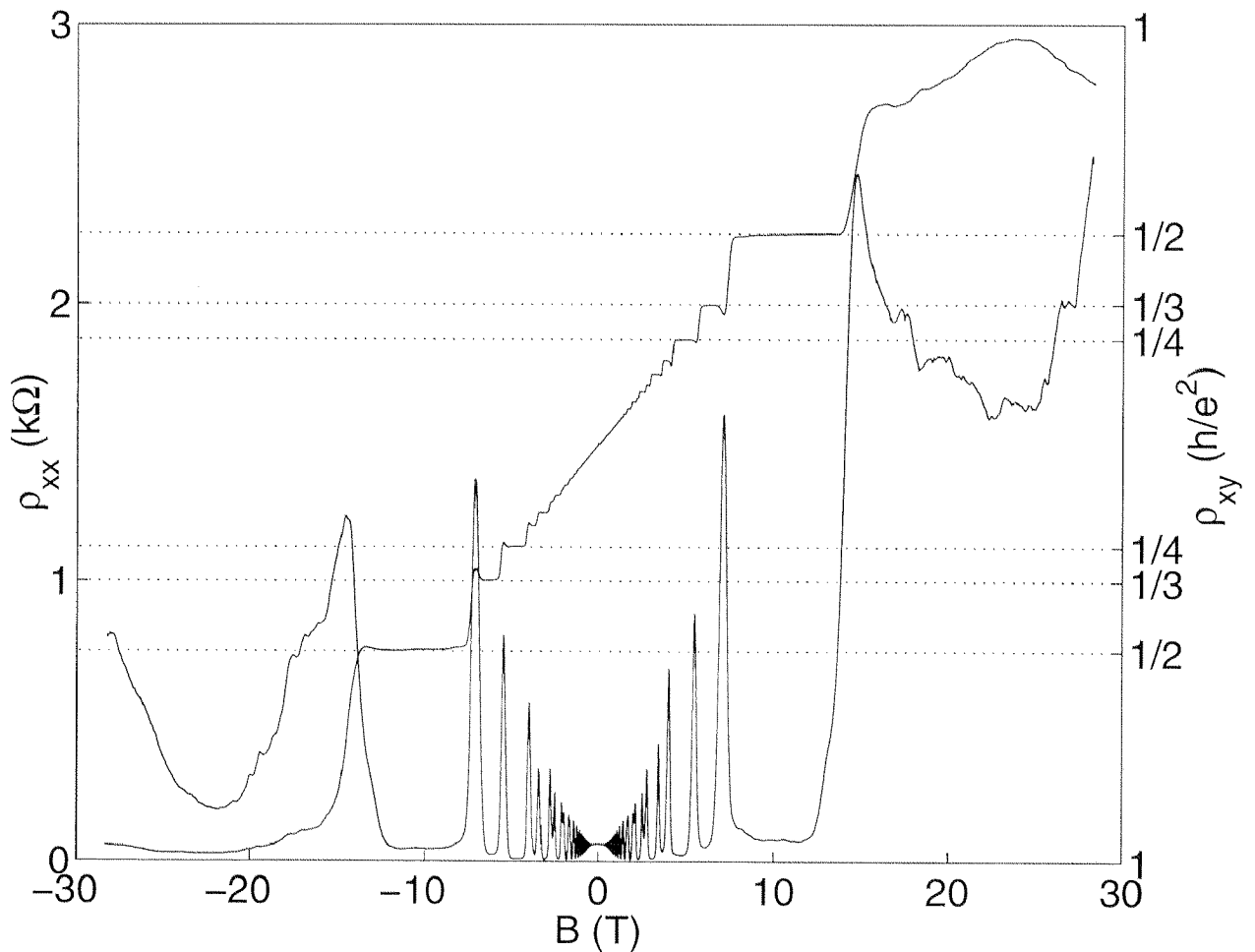


Figure 3.4: Magnetotransport over a wide field range in sample J.

In Figure 3.4 magnetotransport data for a typical sample are displayed. Some InAs-specific features are evident from this image.

The resistivity in the SdH plateaux, e.g. for $\nu = 2$ at $|B| = 10$ T, does not precisely vanish. This is found to be the case in most samples. In the ‘extreme quantum limit’, there are flat-bottomed plateaux of ρ_{xx} but there is a finite voltage drop along the sample nonetheless. If this was simply a contribution of ρ_{xy} , the sign of the finite voltage should depend on the sign of B , but that is not the case. SdH plateaux are always shifted upwards.

At the high-field end of the quantum Hall plateaux in ρ_{xy} , a dip can be seen where $|\rho_{xy}|$ is decreased below the quantized value. This cannot be a contribution of ρ_{xx} to the signal, clearly, because the sign of the dip changes with the sign of B . There is no Hall plateau at $\nu = 1$. Also, ρ_{xx} is finite at $\nu = 1$, and there is a strong asymmetry between B and $-B$. The irregular behaviour is not noise, but all the structure in the high-field part of ρ_{xx} is reproducible.

In this measurement it was specifically verified that all the ohmic contacts remain sufficiently conductive at high fields. In two-terminal measurements over each of the contacts in use, no increase in resistance was found that would account for the irregular behaviour that sample J exhibits in high fields. Instead, the expected resistance $\rho = \rho_{xx} + \rho_{xy}$ was measured in the two-terminal configuration.

In a sample with even lower density, the $\nu = 1$ plateau was seen at ~ 10 T, [Hopkins91]. In higher fields, they also found a deviation from the ‘normal’ quantum Hall behaviour: ρ_{xx} was very large in high fields, and ρ_{xy} drops and reproducible irregular features arise, similar to those in Figure 3.4.

Chapter 4

Experimental Methods

This chapter sums up the experimental procedures and methods used in this work.

4.1 Sample preparation

InSb/AlSb quantum wells were processed into Hall bars for transport measurements. This was done by photolithography and wet-etching.

Samples were split into pieces of appropriate size, mostly 3×3 mm, cleaned in acetone, isopropyl alcohol and last in DI water, and spin-coated with photoresist. After exposure in a mask-aligner through an appropriate mask which leaves the regions where the MBE layer is to remain as a Hall bar unexposed, the samples were developed in the developer solution (MF319). This solution is alkaline, and slowly etches GaSb. This means that GaSb-capped samples are attacked by the developer as soon as the resist is gone. This is not a problem, since these regions are to be etched anyway. However, if something goes wrong with the exposure or development, one can not remove the resist and simply start afresh, because the surface is already slightly patterned.

Wet-etching is done by selective etchants for Al/GaSb and InAs, respectively. The Antimonide is etched by ammonia solution 30%:water (1:5), at a rate of about 11 nm/min. This etch hardly attacks InAs, but makes the Ga/AlSb surface rough. When etching the top barrier down to the quantum well, it can be judged when the InAs is exposed completely because the surface smoothes out again and the etched part becomes mirror-smooth once more. It is not feasible to leave samples in the ammoniac solution for longer than they are due, though: the photoresist is slowly eaten away by alkaline solutions. This is a problem with very thick top barrier layers. InAs is etched by acetic acid : water : H_2O_2 (1:5:1), at about 10 nm/min. The selectivity is high, and etching stops once the InAs is taken away. It is useful to partly remove the

bottom barrier as well, because otherwise residual current paths can spoil the proper Hall geometry. Samples with a very thick top Ga/AlSb barrier could only be patterned with highly diluted HF (1:700). This etches both InAs and Ga/AlSb vigorously, and avoids the problem of the dissolving photoresist for long etch times in ammonia solution. On the other hand, mesa edges appear rougher than those achieved with the selective etchants.

Ohmic contacts are very easily applied on the InAs/AlSb material systems: the best way is to expose the InAs quantum well layer by selectively etching through an appropriate resist mask and to evaporate metal directly onto that. $100\ \mu\text{m}^2$ ohmic contacts made in this way only have $\sim 500\ \Omega$ contact resistance at room temperature. At low temperature the resistance still is well below critical values that render 4-probe measurement difficult. Another possibility is to just apply droplets of Indium metal onto the surface and alloying for a few minutes at $250\ ^\circ\text{C}$. These contacts are usually good at room temperature but sometimes, low temperature resistances are too high, especially when a magnetic field is applied.

Some Hall bar samples have been made from ‘macroscopic’ rectangles of quantum well material, say, $3 \times 5\ \text{mm}^2$, using hand-soldered In contacts only. If Indium is applied with a hot soldering iron to the *edge* of the sample, very good contact quality can be achieved.

4.2 Transport Measurements

In Fig. 4.1, a typical measurement setup is displayed. The sample resistance is measured in an AC configuration, using lock-in amplifiers. A current is passed through the current contacts of the sample by connecting the lock-in reference output voltage via some large resistor, usually $10\ \text{M}\Omega$. As long as the total sample resistance is small compared to $10\ \text{M}\Omega$, this arrangement makes up an AC current source. On voltage probes alongside and across the sample, ρ_{xx} and ρ_{xy} , respectively, can be picked up through the differential inputs of the lock-in amplifier.

4.3 Cryostat environment

The sample is immersed in a ^4He cryostat. The sample space is thermally insulated from the main Helium bath and can be evacuated with a rotary pump. A needle valve allows to let liquid Helium into the sample space at a slow rate. With this arrangement, the sample space can be maintained at some

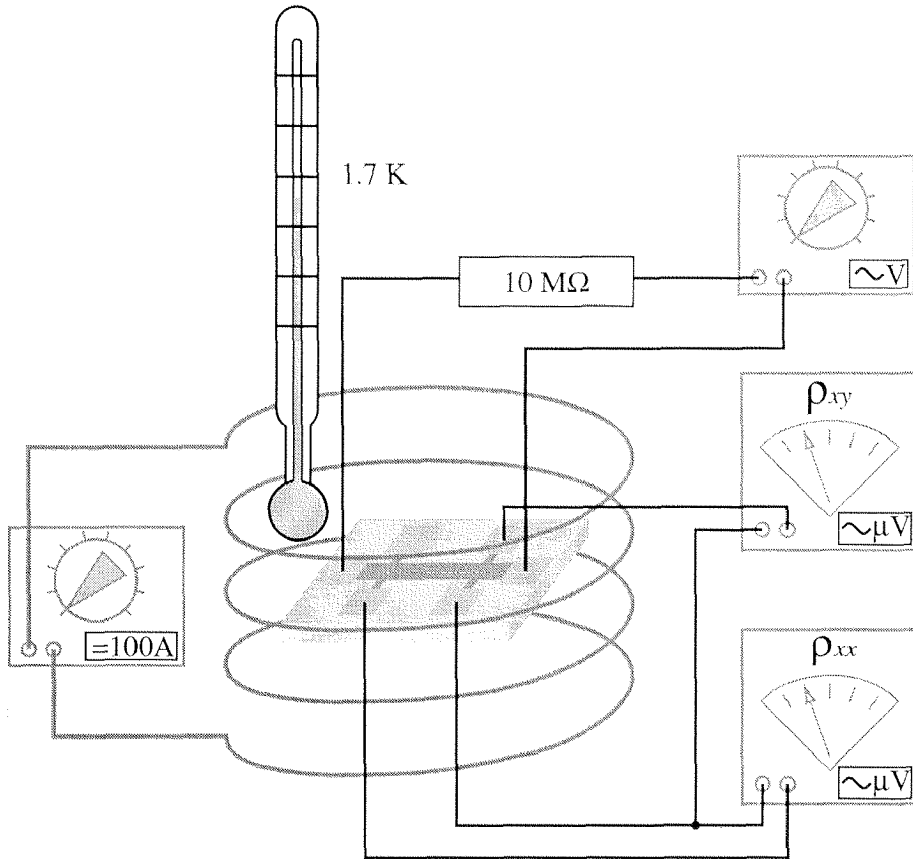


Figure 4.1: Cartoon image of the typical measurement setup: A Hall bar measured in AC 4-probe configuration, in a ^4He fridge with a superconducting magnet solenoid.

small pressure below 10 mbar. The sample is cooled by the evaporating Helium to temperatures around 1.7 K. The base temperature of this kind of cryostat is limited by the ratio of cooling power and the external heat load. A heating resistor is fitted at the He needle valve outlet, so that the temperature of the emerging gas can be increased. The temperature can be set to arbitrary values between base temperature and room temperature, and is maintained constant by a PID controller within 0.5%. Allen-Bradley carbon bulk resistors are used to measure the temperature. The Helium bath cools a superconducting magnet solenoid as well, that can be energized with ~ 100 A to a magnetic flux density of 8 T.

Measurements in extreme magnetic fields were performed with a resistive room temperature magnet (a so-called Bitter coil, see Figure 4.2). The cryostat here is a tube that extends into the bore of the magnet. The sample chamber can be flooded with ^3He , through pump-cooling the outer helium bath this is condensed to liquid. Subsequent pumping of the ^3He allows to lower the sample temperature to about 350 mK for several hours. For some measurements, a dilution refrigerator with a 15 T magnet and a base temperature of ~ 100 mK was used.

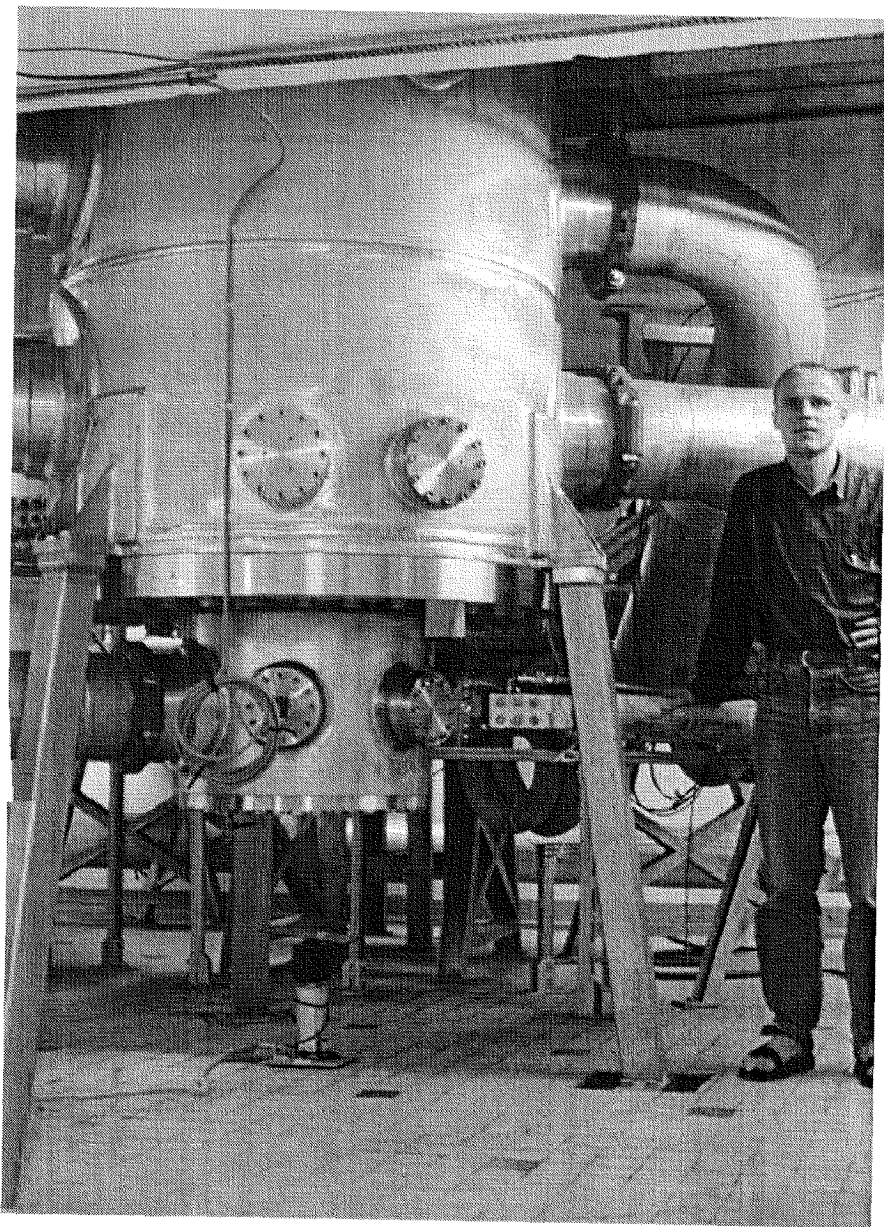


Figure 4.2: The 30 T Bitter coil magnet at Grenoble. My own person is there to give an impression of the size of the installation. The big tubes are for cooling water. My hand rests on one out of eight current leads that feed a current of up to 14 kA into the magnet at full field.

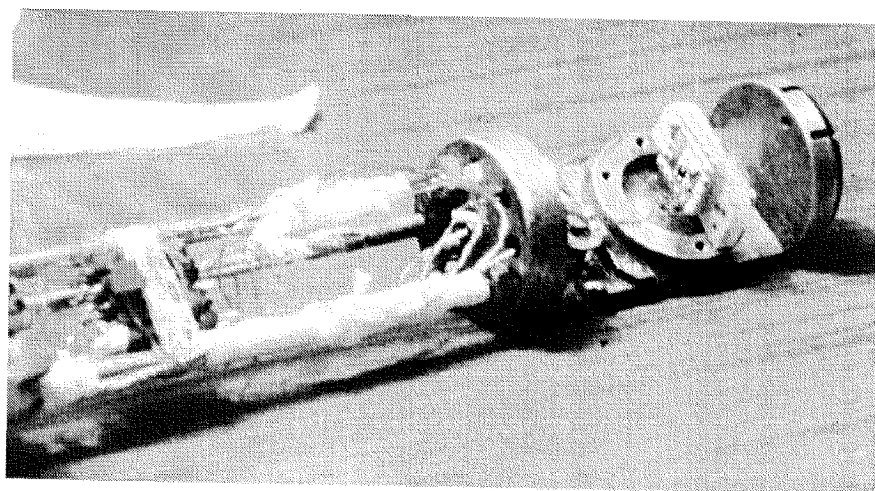


Figure 4.3: The end of the tiltable probe for the ^3He fridge at Grenoble. The sample is mounted on a revolving stage that can be adjusted with very high precision (see section 4.4.1).

4.4 Tilted Field

In order to adjust the field direction with respect to the sample normal, a tiltable sample stage is employed. In Figure 4.4 the tilt mechanism for the ^4He cryostat is displayed. The angle can be set with a resolution of 0.1° . The reproducibility of angles is of the same order. In the dilution refrigerator, the rotator is an epoxy construction that allows for very fine adjustment of the angle. The angle has to be set manually. The resolution is about 0.01° . Due to frictional heating, the sample temperature rises to several 100 mK whenever the angle is increased by some degrees, and cooling back to base temperature takes about 30 minutes. The ^3He insert for the high-field magnet at Grenoble has a tiltable stage with a resolution better than 0.005° (Figure 4.3).

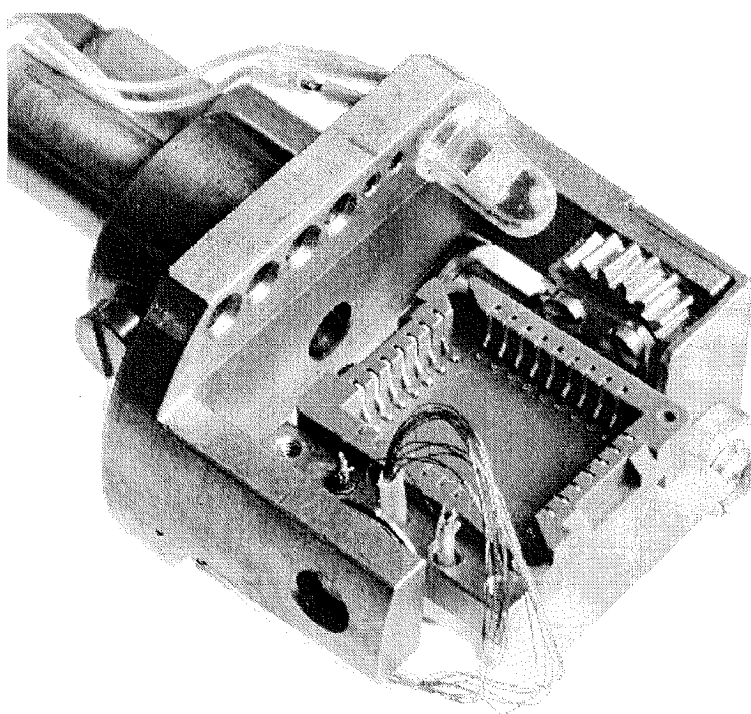


Figure 4.4: The rotatable sample stage for the ^4He cryostat. The tilt is operated by a stepper motor and controlled via a computer interface.

4.4.1 Precision of Angle Determination

In all cases, the angle readout on the dial has an offset, backlash and some intrinsic inaccuracy. In order to determine the angle precisely, the signal from the sample offers two features that depend on B_{\perp} , the field perpendicular to the sample only. Once one measurement has been made in perpendicular field, the slope R_{xy} of $\rho_{xy}(B)$ at small fields can be used to work out the angle. The angle then is simply

$$\alpha = \arccos \left(\frac{R_{xy,\alpha}}{R_{xy,0}} \right).$$

This procedure is simple and easily performed, but suffers in accuracy if the dynamic range of the amplifier forces a switch in measurement range, which introduces a systematic error in α . A more precise method is based on equation (2.13) and the fact that the degeneracy of Landau levels is dependent on B_{\perp} only. Once the angle is known roughly, directly from the dial readout or by the ρ_{xy} method, it is easy to match SdH minima to their filling factors, and by that the angle can be found. Because there is always a whole series of minima to be matched to filling factors, the accuracy is very good.

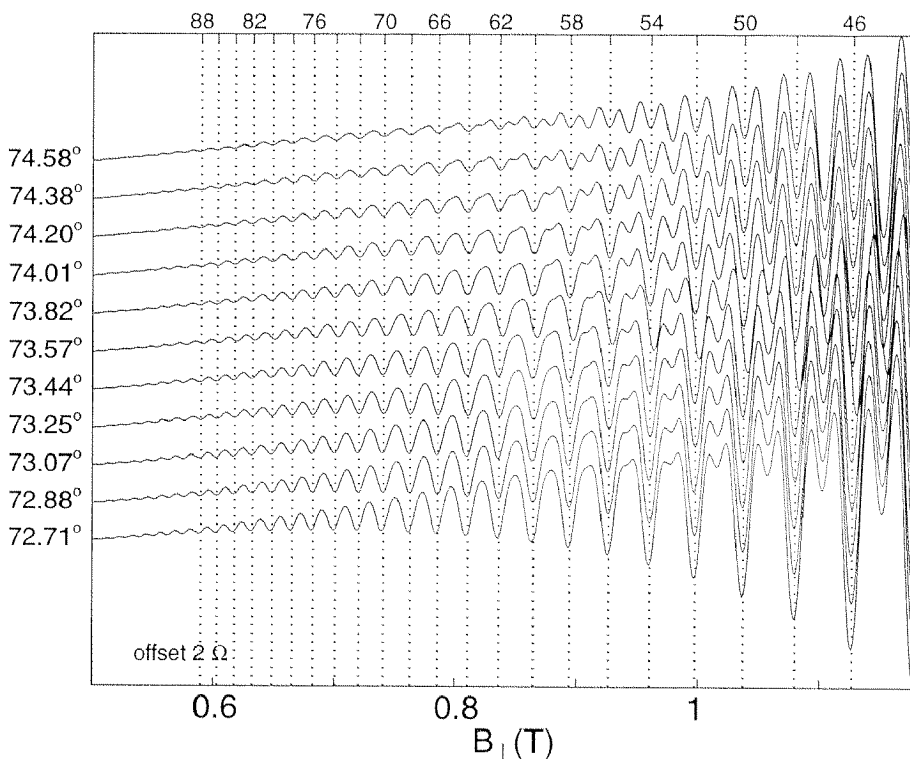


Figure 4.5: A set of angle-dependent ρ_{xx} traces. To demonstrate the sensitive angle calibration with SdH extrema, the angle of one of the traces (73.75°) has been deliberately set 0.04° too small, so that the minima of that curve do not align with the rest.

To demonstrate the effectiveness of this method, Figure 4.5 shows $\rho_{xx}(\alpha, B)$ data where the angle for one curve has been maliciously decreased by $\Delta\alpha = 0.04^\circ$. After the conversion of B into B_{\perp} this means that the minima are shifted

to larger B by a small amount. Looking closely, it is not difficult to find the curve and correct the error. In the interesting angle range of 70° and above, this method guarantees a precision of angle readout of around $\Delta\alpha = 0.04^\circ$. The process of matching filling factors to minima can be tedious, which is why we use an interactive MATLAB routine with point-and-click interface to do it. If the ρ_{xy} measurement is precise enough and care has been taken not to switch ranges during the whole measurement, the ρ_{xy} method is sufficient, the angle calibration in Figure 4.5 has been made in this way.

4.5 Hydrostatic Pressure

This section describes hydrostatic pressure measurements in principle. Details of the setup used and the handling are covered in Appendix C.

4.5.1 Pressure Cell

Pressure experiments were conducted with a clamped pressure cell. The principle of the cells is simple: The sample inside the cell is immersed in a liquid. The liquid can be compressed with a hydraulic press, and the fixing screw keeps the liquid compressed even after the cell is taken out of the hydraulic press (and is put in a cryostat for measurement). In Figure 4.6, the main parts

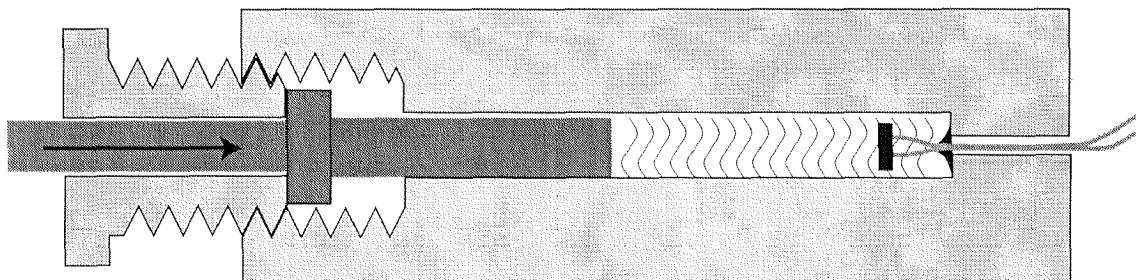


Figure 4.6: Schematic diagram of a clamped pressure cell. The pressure rod (the bit with the arrow in it) is removed once the desired pressure is set and the fixing screw is tightened.

of the cell are displayed. The pressure transmitting liquid, a mixture of thin oil and a higher alcohol, is compressed to less than half its original volume at ~ 2 GPa, the highest pressures available with this kind of setup. The actual device is more complicated than this, important details (like seals etc.) have been omitted here. A full account of the pressure cell used in this study is given in Appendix C.

4.5.2 Pressure Sensors

Two types of pressure sensors were used in this work: the manganin gauge and the InSb gauge. Each have their own advantages and disadvantages, which are discussed here.

Manganin Gauge

Manganin wire is used as a standard tool for measuring pressure in the range up to 5 GPa. The alloy is commonly used as resistive wire material and thus readily available. The resistance-pressure relationship that was used is as follows

$$R(p, T) = R(p = 0, T) [1 + \alpha p], \quad \alpha = 2.49 \cdot 10^{-2} \text{GPa}^{-1}$$

However, experience shows that meaningful pressure values can only be achieved with wire that has undergone an aging process, meaning a series of cooldown-warmup cycles as well as pressurize-depressurize cycles. The $\phi 70 \mu\text{m}$ wire is wound in a coil with about 100Ω , and connected to 2 leads on each side to allow a 4-terminal resistance measurement. The coil is small and can be fitted into a pressure cell easily. The temperature dependence of the resistance is rather strong: between room temperature and He temperature, the resistance goes down by about 10%. This has to be compared with the relative change of resistance due to the pressure change, which is only about 1% in the useful range of pressures. The resistance still has a substantial $\partial R/\partial T$ at 4 K, so that it is important to determine the temperature precisely in order to get a valid pressure readout at low temperatures.

Indium Antimonide Gauge

Indium Antimonide is a small-bandgap semiconductor. Its use as a pressure gauge has been described by Cończykowski et al. [Conczykowski78]. In highly-doped InSb the carrier density does not depend on pressure, because ionized donor impurities create no localized states due to InSb's low effective mass. The conduction electron mobility, however, depends strongly on the pressure. This effect is caused by a change in the shape of the conduction band.

The sensors used in this work have been made out of (100) InSb single crystal wafer, doped to $2 \cdot 10^{22} \text{m}^{-3}$ with Tellurium. Rectangular pieces of approx. $4 \times 0.5 \times 0.5 \text{mm}$ were cut and wired with 4 In droplets for four-point readout of the resistance, which is of the order of $10 \text{m}\Omega$. The following simple relation is used for determining the pressure from the InSb sensor 4-terminal resistance:

$$R(p)/R(p = 0) = 1 + \alpha p + \beta p^2 \quad (4.1)$$

For room temperature and low temperature, different values for α and β have to be used:

	300 K	4.2 K
$\alpha(\text{GPa}^{-1})$	0.3368	0.3928
$\beta(10^{-2}\text{GPa}^{-2})$	8.05	7.67

The values are from a commercial InSb sensor, an SPG10 gauge from Unipress (Warszawa). Comparison to a home-made sensor from InSb provided by Wafer Technology, Milton Keynes (UK), has been compared in an experiment and it appears that the same coefficients can be used with our sensors. The values in the table above show that InSb's performance as a pressure sensor is much superior to the manganin coil: the temperature dependence is rather small, in fact, below 10 K it is hardly measurable. The pressure dependence is stronger by a factor of over 100. Compared to a manganin coil, InSb sensors are bulkier, and they are easily damaged because the crystal is so soft and fragile. Making an InSb gauge requires some skill, practice, and patience.

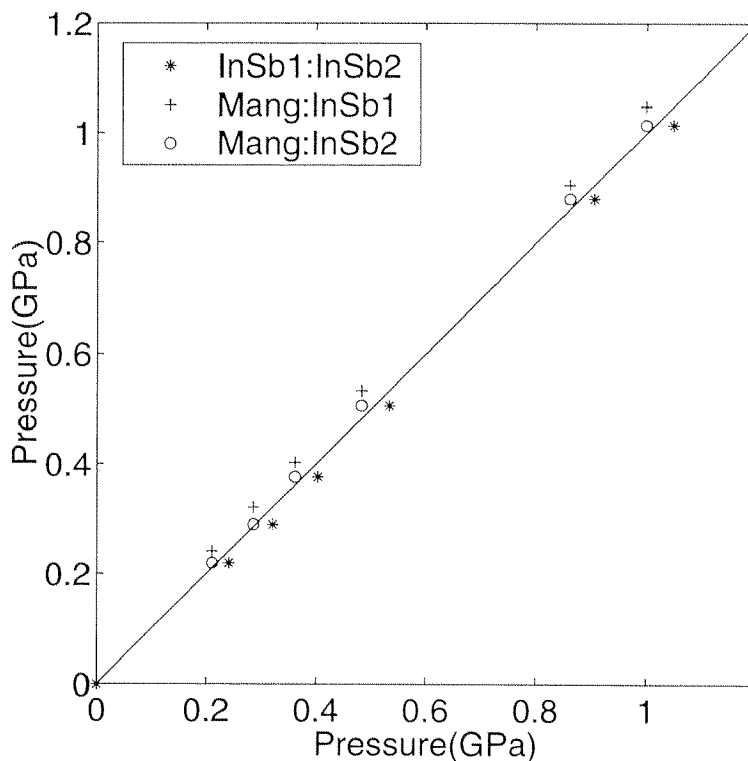


Figure 4.7: Comparison of pressure readout by different sensors. In one experiment, a manganin gauge and two specimens of InSb gauge were combined in a pressure cell (4.2 K).

Figure 4.7 shows a comparison between values from three different sensors. All sensors were mounted in one pressure cell and have been measured at room temperature and at helium temperature. The sensor labelled InSb1 delivers values ~ 20 MPa too high. This deviation is typical for these sensors and may be considered as the margin of error in pressure determination.

4.6 Effective mass determination

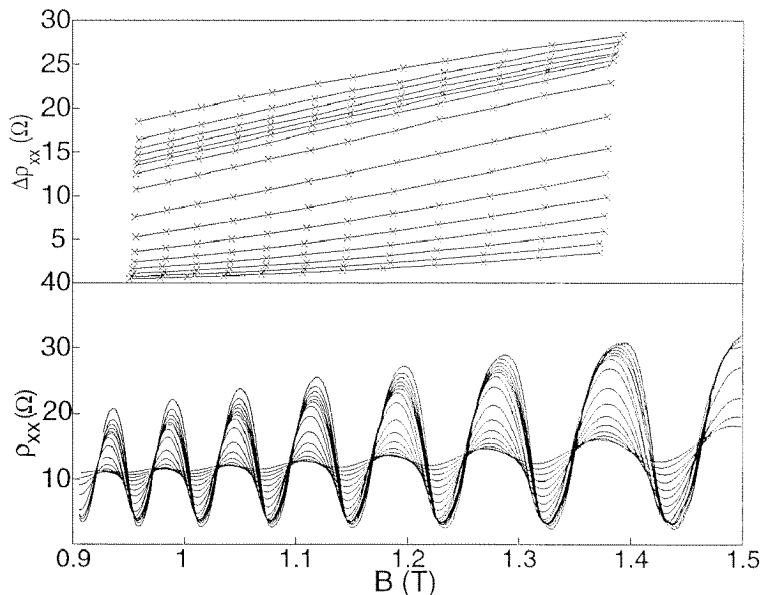


Figure 4.8: Bottom: SdH traces at temperatures from 1.7 K up to 12 K. Top: Amplitude curves of the data below. Sample F, carrier density $8.45 \cdot 10^{15} \text{m}^{-2}$.

Shubnikov-de Haas oscillations (and related magneto-oscillations) probe the density of states (DOS) of a system at the Fermi level as a function of the magnetic field. The Fermi edge at very low temperatures is sharply defined. As the magnetic field is varied and the number of electrons in a Landau level (LL) changes, the Fermi edge either lies in between two LLs or in the middle of one. The difference in DOS available for transport is responsible for the difference in conductance between the two situations and appears as the *amplitude* of SdH oscillations. As T is increased and the width of the Fermi edge approaches the energy gap between adjacent Landau levels, the SdH amplitude decreases. Thus, the temperature dependence of SdH amplitude reflects the energy difference of adjacent Landau levels near the Fermi edge, the Landau gap $\hbar\omega_c$. From $\omega_c = eB/m^*$, we see that ω_c holds information about the effective mass of the charge carriers in question. According to equation 2.15 the only temperature-dependent part in the expression for the conductivity in the SdH-domain is the term

$$\frac{2\pi k_B T / \hbar\omega_c}{\sinh 2\pi k_B T / \hbar\omega_c}. \quad (4.2)$$

This term is often referred to as the *Dingle term*. Furthermore, it does *not* contain τ_q , i.e. it does not depend on the width or shape of the Landau levels. As long as there is some gap in the DOS, the way in which its effect is washed out by temperature reveals the magnitude of the gap.

The logical next step is to measure sets of SdH data at varying temperatures. We went on to define the amplitude as shown in Figure 4.8: by constructing en-

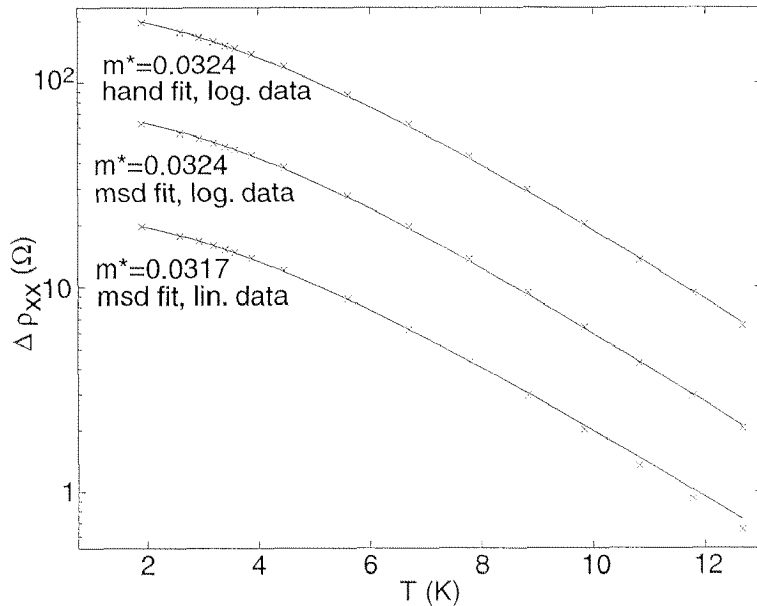


Figure 4.9: $\Delta\rho_{xx}(B)$ data (\times es and fitted curves (lines) according to expression (4.2), to figure out the effective mass. Curves have been offset for clarity. Fitting was done by minimizing the mean square deviation of data from the curve given by the model, using the data plotted linearly or logarithmically, as well as a best fit done “by hand”. The resulting m^* is given for each fit. Data is from Fig. 4.8, evaluated at $B = 1$ T.

velope curves, which interpolate between adjacent minima or maxima linearly. The difference between the two envelopes is the amplitude: this is evaluated at different constant magnetic fields to form $\Delta\rho_{xx}(B)$ -traces. The resulting traces can be fitted with the expression (4.2), as displayed in Fig. 4.9. Because the amplitude varies over orders of magnitude in the available temperature range, the results were plotted on a logarithmic scale.

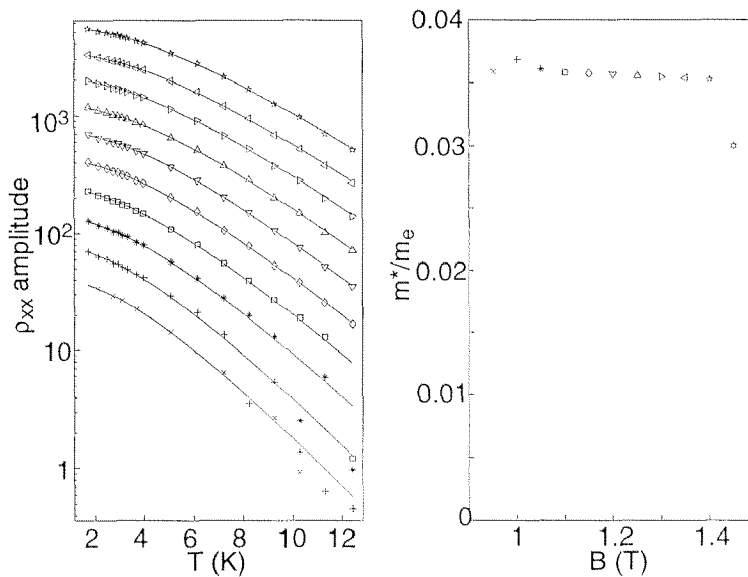


Figure 4.10: Left: SdH Amplitude data at several magnetic fields (symbols) with best fit curves (lines), curves offset for clarity. Right: effective mass determined from the fits on the left, determined at different magnetic fields. The symbols correspond to matching ones in the picture on the left.

The fit obtained by minimizing the mean square deviation (msd) looks unsatisfactory here: at the high- T end the fitted curve consistently deviates from the data points (Fig. 4.9, bottom curve). We tried to do it better by hand, and obtained the fit shown in the top of Fig. 4.9, yielding a slightly larger m^* . The same result is obtained when applying the msd fit to the log of the data. Which method is the “right one”? Clearly, fitting data by eye can

be useful if fitting algorithms end up on a dead end road and hindsight can be applied, but otherwise it is not ideal because it is subject to human errors. But since the dynamic range of the amplitude data is large, and, as can be seen in the plot, even for small amplitudes the data fits well to the curve and scatter is small, the logarithmic fit method is the feasible one, since it puts equal weight on the low and high temperature data. Consequently, it is the one applied in the analysis in this work.

The range of magnetic fields in which this method can be applied is limited: at the lower end, because the SdH amplitude is too small to be measured precisely, limiting the useful range of temperatures, on the high-field end because SdH oscillations are no longer sinusoidal, because of the onset of a visible spin splitting or because the resistivity approaches zero in the minima, yielding the model invalid. Eventually, the effective mass was evaluated at an intermediate magnetic field where the *change* of resulting mass with the magnetic field is small. Figure 4.10 shows this: within 1.1 T and 1.4 T, the result from the fit is stable.

4.7 Determination of τ_Q

The exponential term in 2.15 contains the quantum scattering time τ_Q . Exploiting this, we can extract a value for τ_Q from the magnetic field dependence of the ρ_{xx} amplitude. (Fig.4.11 a-c) It is convenient to plot the log of the amplitude divided by the Dingle term (4.2) as a function of $1/B$ (Fig.4.11 d). Then, the slope of the graph directly yields τ_Q . This way of representing the data is known as the Dingle plot.

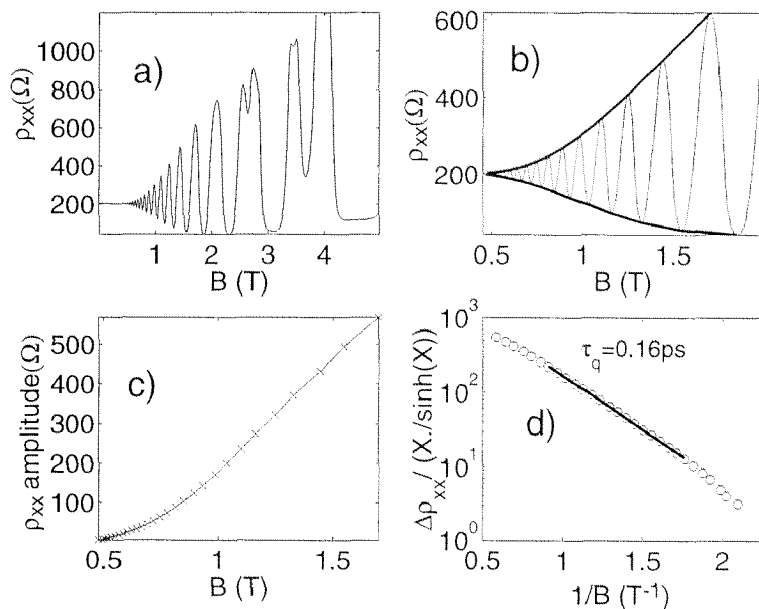


Figure 4.11: Determination of τ_Q . a) ρ_{xx} trace. b) lower and upper envelope curves of ρ_{xx} . c) ρ_{xx} amplitude: difference of both envelopes. d) Dingle plot, semilog plot of ρ_{xx} amplitude scaled by $\sinh X/X$, vs. $1/B$. Sample J.

Once again, there is only a certain range of B in which this evaluation makes any sense: B large enough for oscillations to be clearly discernible, but small enough for the model to hold at all. In Dingle plots, we assume this region to be where data lies more or less on a straight line.

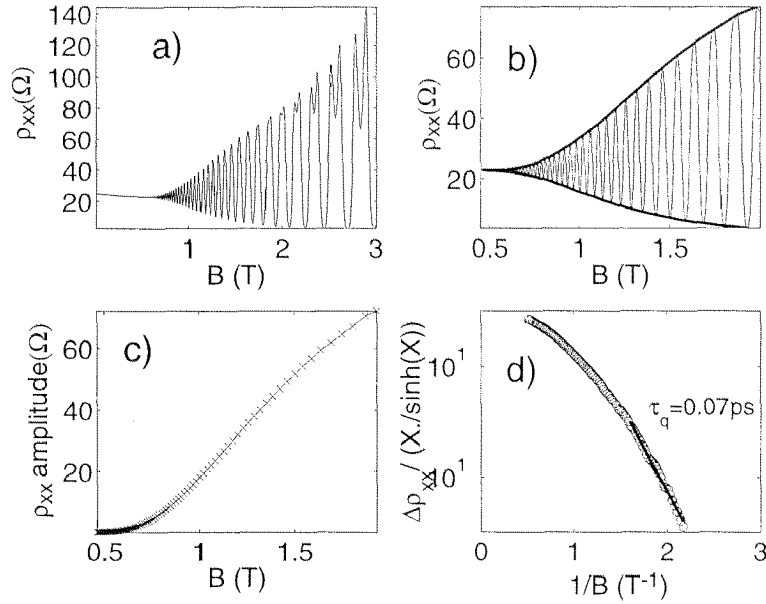


Figure 4.12: Determination of τ_Q , like 4.11, but for sample F. ($N_s=1.2 \cdot 10^{16} \text{ m}^{-2}$). No portion of the Dingle plot is a straight line. The low-field part has been fitted to equation (2.15).

As has been pointed out in 2.4, the functional dependence of the Landau level width on magnetic field is crucial in this evaluation, since the theory predicts (2.15) only for a special scattering scenario which approximately applies to silicon MOSFETs. Figure 4.12 shows data from sample F. The carrier density is higher by a factor of three compared to sample J, so effects of non-parabolicity are expected to be much stronger. In this case, the size of the Landau gap increases with B weaker than linearly. Since both m^* and Γ potentially depend on B , analyzing the SdH amplitude in a Dingle plot does not reveal one parameter clearly.

Chapter 5

Spin splitting in a tilted magnetic field

Transport and optical studies in two-dimensional electron system have been investigated in tilted magnetic fields for a long time. In 1968, Fang and Stiles [Fang68] published the first measurements of 2D electrons in inversion layers on Silicon surfaces. They managed to measure the electron g factor, dependent of the electron density, and found it to be “substantially larger than 2”. Subsequent to this, a great number of theoretical and experimental studies have been conducted in this direction. T. Ando et al. found that the spin splitting is enhanced whenever there is a population difference between the two spin states. These results are summarized in [Ando74b]. This was confirmed experimentally by Lakhani et al in [Lakhani73], in Si MOSFETS. In a study of tilted-field transport measurements on GaAs-GaAlAs heterojunctions R.J. Nicholas et al.[Nicholas88] investigated the oscillatory nature of the electron g factor. In the GaAs/AlGaAs material system this effect is strong because the bare spin splitting is small. Lately, Leadley et al.[Leadley98] found conditions for the onset of visible spin splitting in transport phenomena strongly dependent on the quantum scattering time as well as on temperature, since the exchange enhancement only sets in if there is a spin splitting to begin with.

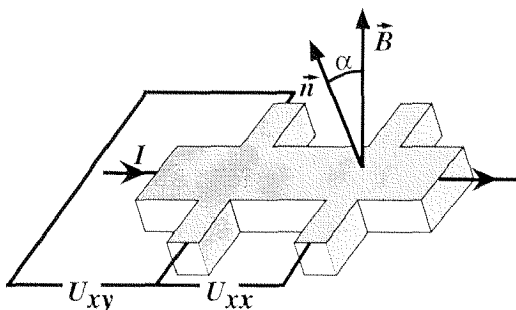


Figure 5.1: Sketch of a hall bar in tilted field. The tilt angle is measured between the sample normal \vec{n} and the magnetic field \vec{B} .

In our experiments, a revolving stage was used, where the sample can be rotated with respect to the magnetic field orientation, all inside a magnet

solenoid and a cryostat environment. The tilt angle α of the magnetic field is measured with respect to the sample normal. The determination of the tilt angle is discussed in section 4.4.

5.1 The Coincidence Method

The most basic observation in magnetotransport of two-dimensional electron systems in tilted magnetic fields is that the Landau splitting, manifesting itself in effects such as the magnetoconductance (i.e. the Shubnikov-de Haas oscillations, sec. 2.2), is dependent on the component of the field normal to the sample only, at least in small fields where the spin splitting of each Landau level (LL) is not resolved. The position of minima in $\rho_{xx}(B_{\perp})$ is constant as a function of tilt angle for a given filling factor. As the tilt angle is further increased, it becomes obvious that the effect of spin splitting is increased with respect to the Landau splitting. The five lowest-angle traces in Figure 5.4 show this: the minima at odd filling factor become deeper as α increases. The onset of a visible spin splitting moves to lower fields: the *total* field at which a ‘dip’ in SdH maxima becomes evident is roughly constant.

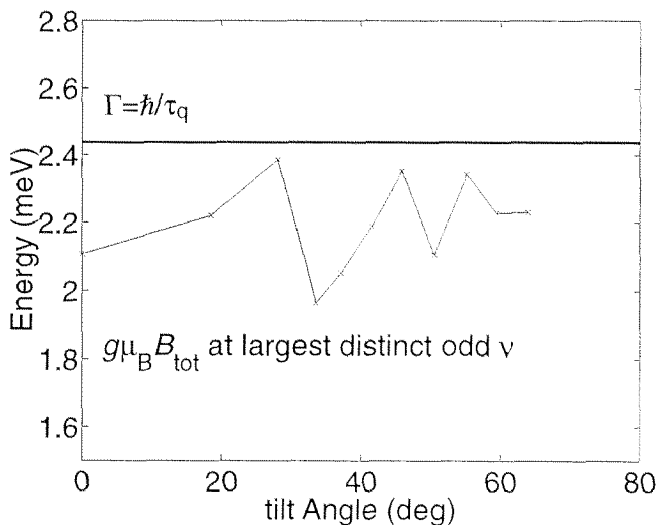


Figure 5.2: Onset of visible spin splitting. The symbols represent the Zeeman splitting energy $g\mu_B B_{\text{tot}}$ at the first discernible odd- ν dip in ρ_{xx} , while the strong straight line is the approximate Landau level width \hbar/τ_q . The line is zigzag because the onset is defined here as a discernible dip at the largest odd factor, which stays the same for more than one angle before it jumps by two.

Figure 5.2 shows a plot of these fields, plotted vs. the angle. The field is represented by the Zeeman gap $g\mu_B B_{\text{tot}}$, using $g = 14$ as in bulk InAs [LB-tables], and compared to the Landau level width. If there were not so many coarse definitions (such as the ‘discernible dip’) and vague parameters (e.g., τ_Q , see section 4.6) involved, a plot like Fig. 5.2 could yield a value for g . However, it confirms that since the spin splitting is a bulk band structure effect, it is independent of the magnetic field orientation.

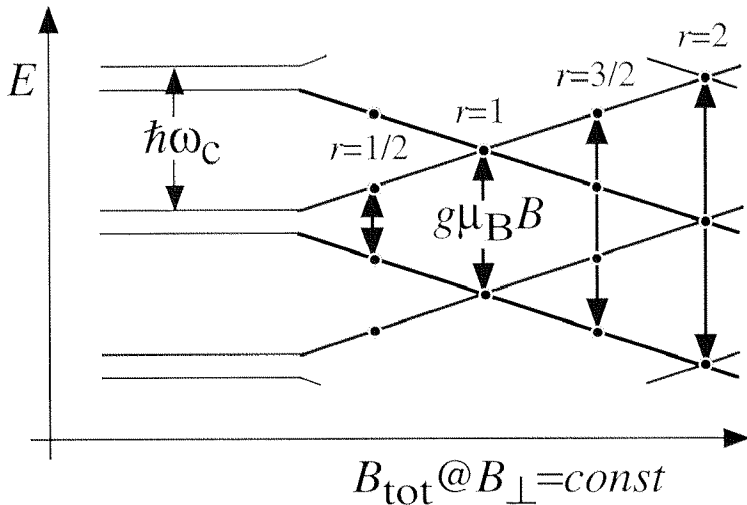


Figure 5.3: Schematic diagram of the spin-split Landau level ladder with increasing total field.

Figure 5.3 shows how Landau levels develop as the total field increases. To the left, when the field is perpendicular to the sample normal, ($\alpha = 0$) the spin splitting is roughly one fifth of the Landau splitting in our samples. We define the ratio r of the spin gap $g\mu_B B$ and the Landau gap $\hbar\omega_c$. The ratio r increases with α , and at a certain point, when $r = 1/2$, the ladder becomes evenly-spaced with gaps of $\hbar\omega_c/2$. Each level's degeneracy is half that of a spin-degenerate Landau level, so that the period of oscillations is halved. The minimum field for magneto-oscillations to appear is doubled in this case.

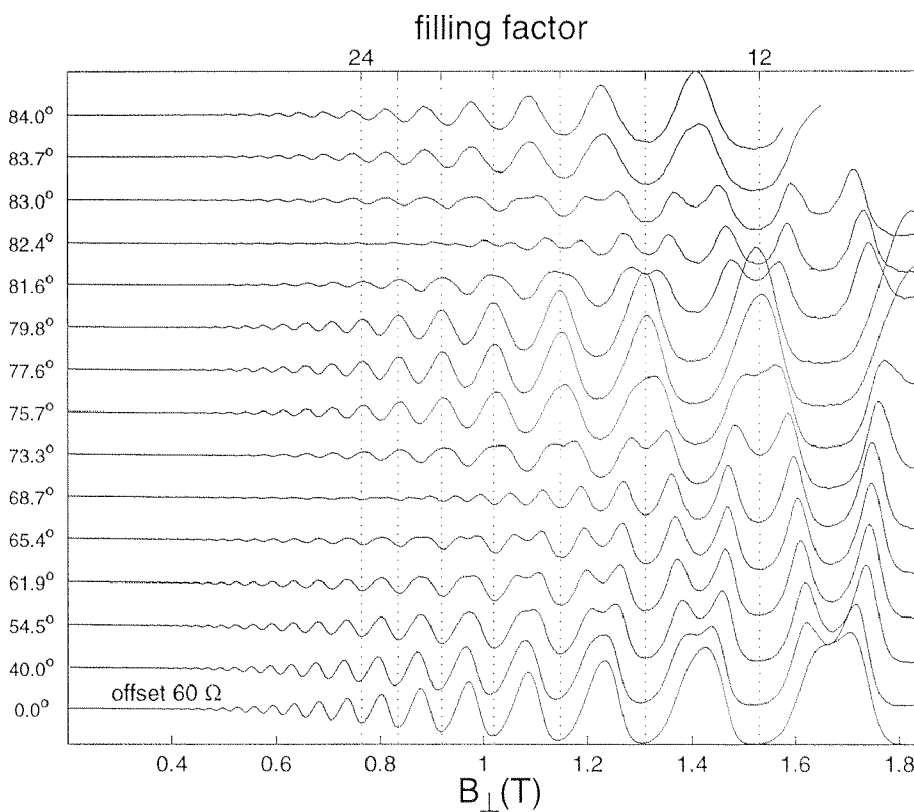


Figure 5.4: ρ_{xx} traces at different coincidence situations: Data from sample J, an offset of 60Ω for each curve has been added in the vertical. The dotted lines mark even filling factors.

This situation is evidently reached in the 68.7° curve in Fig. 5.4. As the

tilt angle is increased further, and the spin gap matches the Landau gap, spin-split sublevels of adjacent Landau levels come to overlap. In that case SdH oscillations are back to the 2-filling-factor period, but with minima at odd filling factors, because there is one unpaired level at the bottom of the ladder. At $r = 3/2$, the SdH period is halved again, while the appearance of $\rho_{xx}(B_{\perp})$ is much like that at $r = 1/2$. At $r = 2$, even-integer SdH minima are recovered. At the same time, the Hall effect shows corresponding features: see Fig. 5.5.

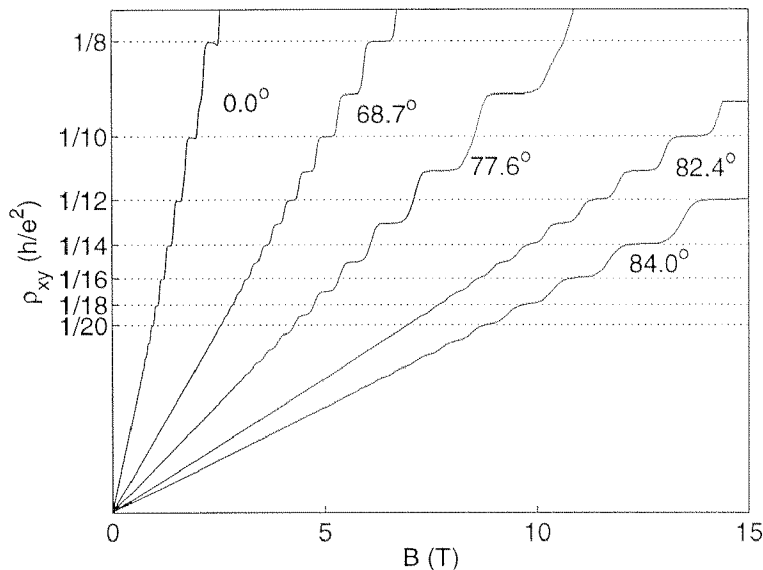


Figure 5.5: ρ_{xy} traces corresponding to ρ_{xx} curves in Fig. 5.4, for $\alpha = 0$, and where coincidences with $r = 1/2, 1, 3/2$, and 2 are met. For half-integer r , both odd and even filling factors plateaux appear, while for $r = 1$ only odd, for $r = 2$ only even filling factor plateaux are there.

If the total field is large enough for sufficient B_{\perp} at large angles, more coincidences can be produced: we have observed this up to $r = 5$, in very strong fields. Figure 5.6 shows a data set like this. The curves where each coincidence is best met are displayed. The picture is not as obvious in its interpretation as Fig. 5.4, because the minima positions are shifted to lower field values as the parallel field becomes large. This effect is examined in section 5.2. Also, in Fig. 5.6, some coincidences have not been met ideally. It is very difficult to adjust the angle exactly to the desired coincidence, since the signal varies rapidly with angle.

Evaluating the ratio r in terms of the tilt angle and the parameters g and m^* , we derive

$$r = \frac{g\mu_B B_{\text{tot}}}{\hbar\omega_c} = \frac{2gm_e}{e\hbar B_{\text{tot}}} \cdot \frac{m^*}{\hbar e B_{\perp}} = \frac{gm^*}{2m_e \cos \alpha} \quad (5.1)$$

and see immediately that at a given tilt angle, r can be used to find the product gm^* experimentally. To this end, a plot of r vs. $\cos^{-1} \alpha$ is useful, since (5.1) predicts a straight line. Consider Fig. 5.8: the experimentally determined slope

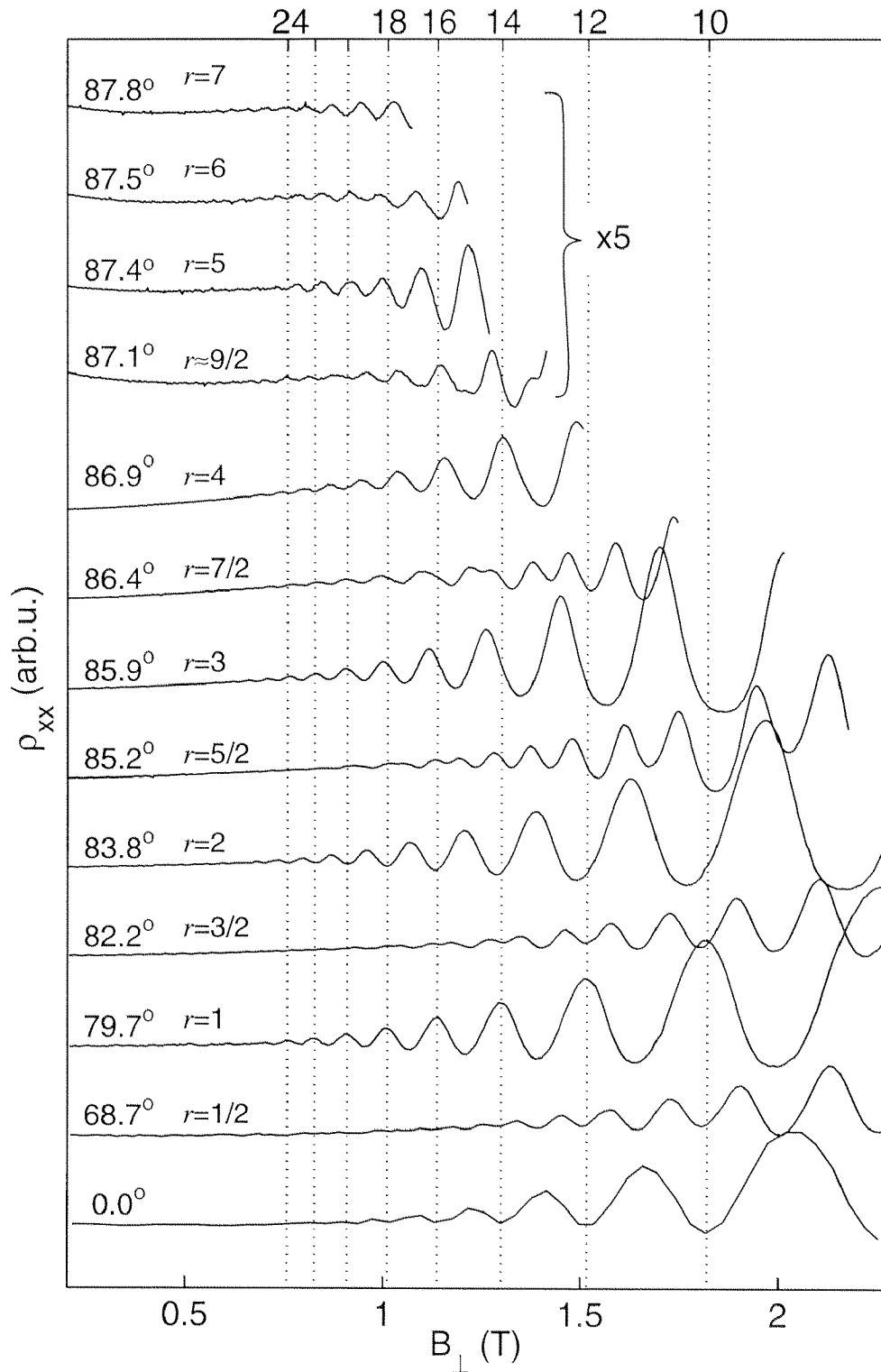


Figure 5.6: ρ_{xx} traces at different coincidence situations: Data from sample J. The top 4 curves have had a linear background subtracted and the amplitude enlarged by a factor of 5, an offset has been added in the vertical. From bottom to top, coincidences with $1/2$ (67.7°), 1 , $3/2$, and 2 (83.8°) seem to be realized exactly. At 85.2° and at 86.4° , the matching of even and odd minima is not quite precise. at 85.9° , 87.4° , and 87.8° , the coincidences with $r=3$, 4 , and 5 take place. Filling factors are not evident from the position in B_{\perp} directly, since the electron density changes in strong B_{\parallel} , see sect. 5.2. However, it is possible to identify filling factors with the ρ_{xy} traces, and by regarding intermediate angles which are not plotted here.

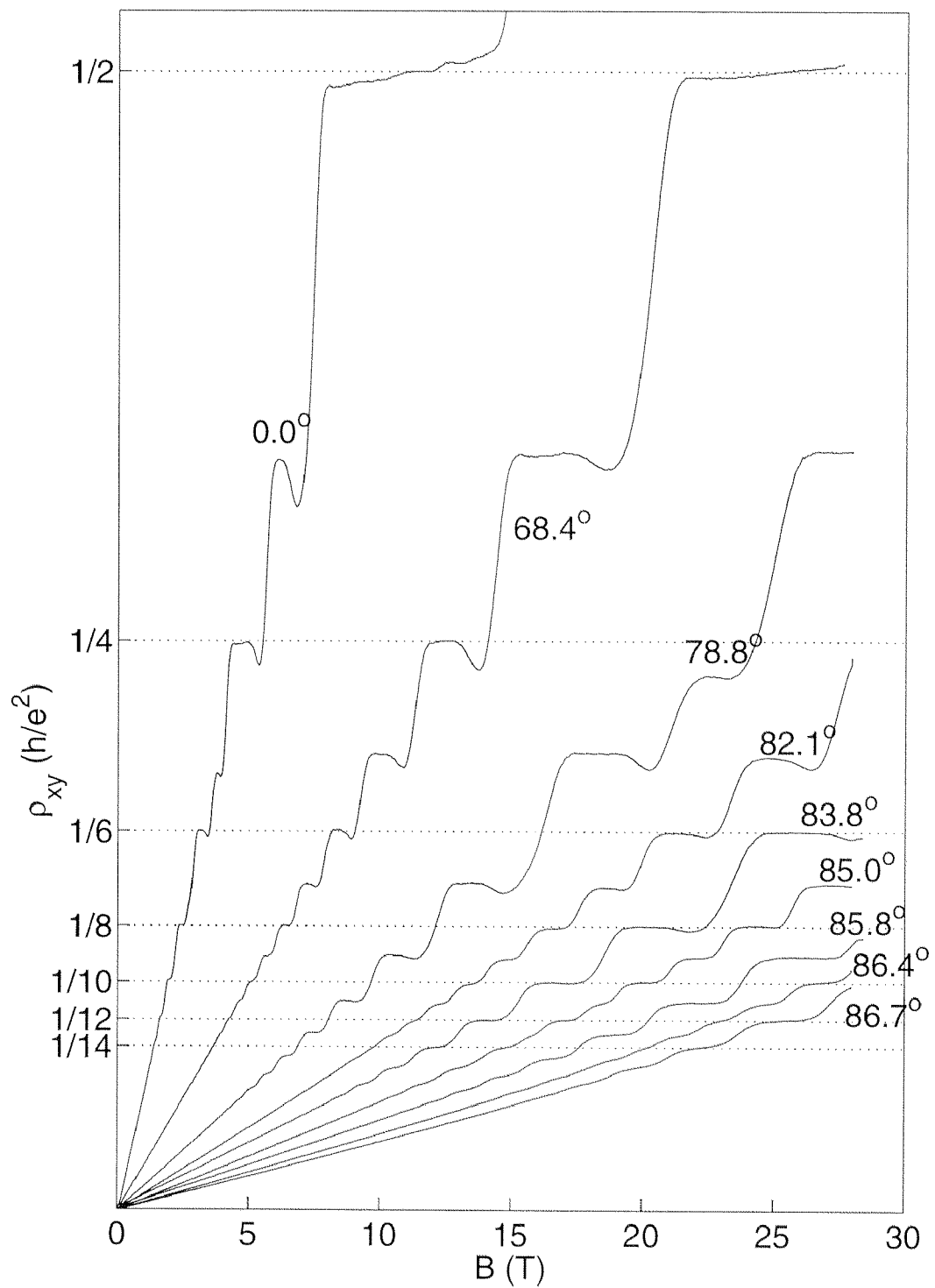


Figure 5.7: ρ_{xy} traces at various coincidence situations, from $r = 1$ to $r = 5$, with r defined as in (5.1). Data from sample J.

yields $gm^* = 0.43$. With an effective mass of $0.031 m_e$ (see sec. 4.6), this yields an electron effective g factor of 13.8, close to the value reported for bulk InAs ($g = 14$) [LB-tables].

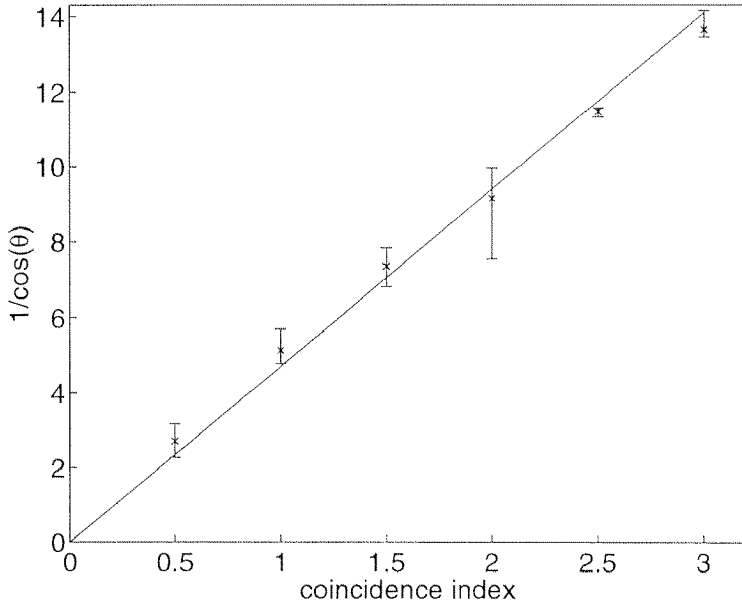


Figure 5.8: “Coincidence plot”: the ratio r of Landau and Zeeman gap, plotted vs. $1/CMOS(\alpha)$ for angles α where coincidence situations are met. Data from sample J.

At first glance it is surprising that Fig. 5.8 and the angles for each coincidence situation match so well with eqn. 5.1, since the effective mass as well as the g factor are expected to vary with increasing magnetic field, so why should their product remain constant?

In a simple two-band approximation, band non-parabolicity leads to an energy-dependent effective mass of

$$m^*(E) = m_0^* \left(1 + 2 \frac{E}{E_g} \right) \quad (5.2)$$

where m_0^* is the band edge mass of InAs. On the same grounds the effective g -factor is reduced. According to Scriba et al. [Scriba93], the g -factor in fact reads

$$g = g_0 (1 - \alpha E), \quad (5.3)$$

with the constant α a material-dependent parameter. From the spin-split cyclotron-resonance experiments reported in [Scriba93], on a quantum well system similar to ours a value of $\alpha = 0.0025 \text{ meV}^{-1}$ is deduced. The product gm^* then becomes

$$gm^* \sim m_0^* g_0 \left(\frac{E}{E_g} - \alpha E \right), \quad (5.4)$$

omitting the E^2 term. Because α is fairly precisely $1/E_g$, this reduces to

$$gm^* \sim m_0^* g_0 \left(1 + \frac{E}{E_g} \right), \quad (5.5)$$

at least for the samples investigated here.

In other words: in gm^* , energy dependence is only half of what it is in m^* .

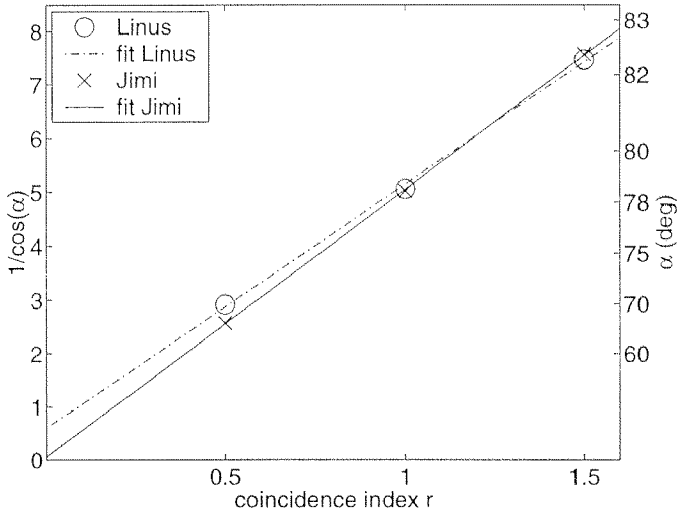


Figure 5.9: Comparison between coincidence plots of sample L and J.

We have conducted tilted field studies on two samples (L and J) with different electron densities, and found different slopes in the coincidence plot, the trend in this data can be compared to the expectation from eqn. (5.4).

In Figure 5.9, coincidences for $r = 1/2$, 1 and $3/2$ are displayed with linear fits through those three points. Data for the sample J ($N_s=4.4 \cdot 10^{15} \text{ m}^{-2}$) fits to the straight line, which goes through the origin. Data for sample L ($N_s=6.1 \cdot 10^{15} \text{ m}^{-2}$) does not match the simple relation in (5.1) quite so well: the line fit does not go through the origin. The slope is smaller, as expected from (5.4), but the value for the angle at $r = 1/2$ is higher than with sample J, in contradiction to (5.4). This may be attributed to the fact that, especially with sample J, the angle of coincidence is dependent on B , so that (5.1) does no longer apply at all.

Figure 5.10 shows a series of $\rho_{xx}(B, \alpha)$ data taken on sample L, in the high magnetic field laboratory at Grenoble. In the resistive magnet, the field is changed rapidly, consequently the small oscillations for low angles are not well-resolved. The highlighted curves are assigned to integer r values, for evaluation in the coincidence plots.

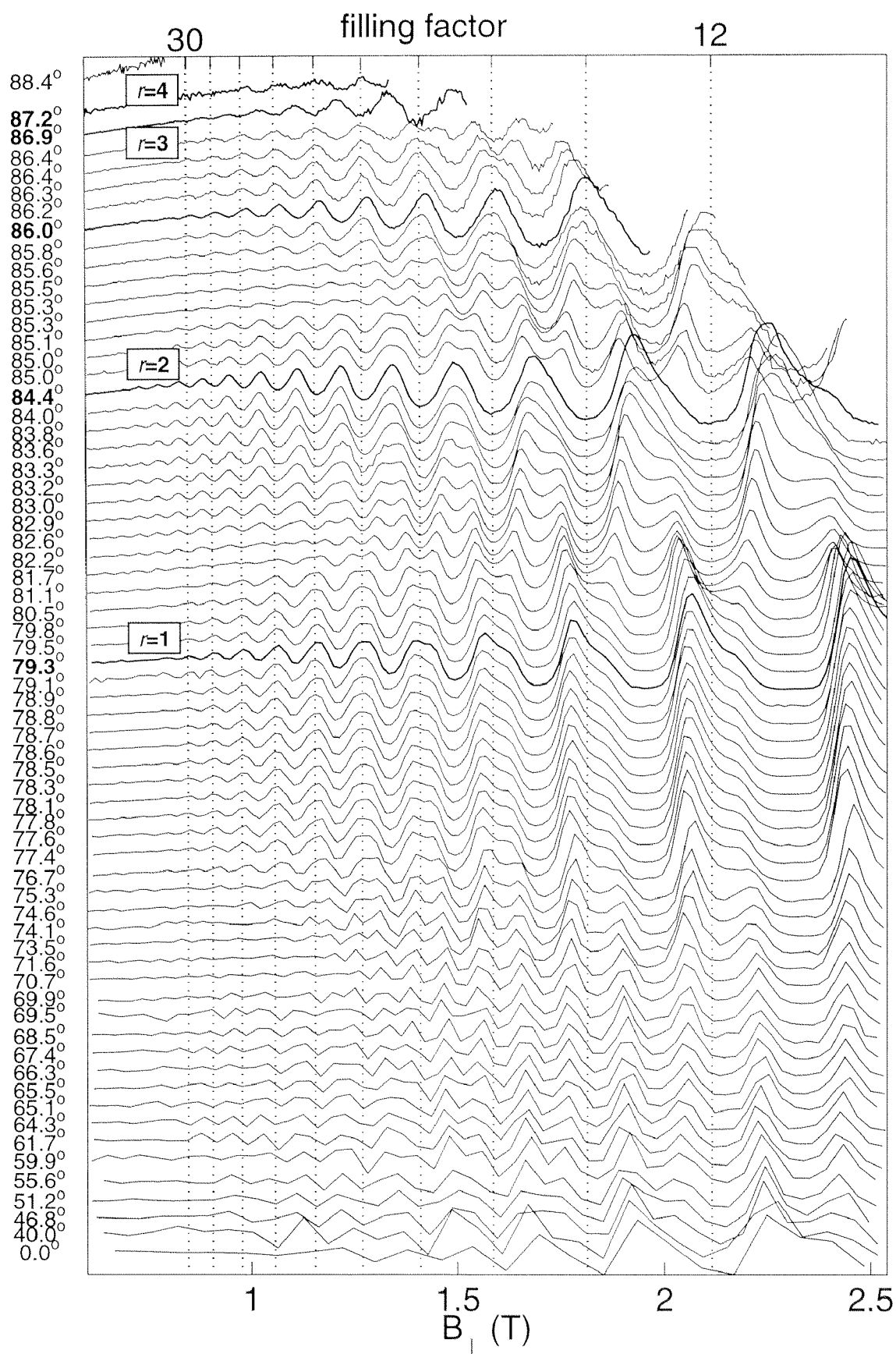


Figure 5.10: ρ_{xx} traces at different angles, sample L: in this magnetic field domain, the picture is similar to that in Sample J, Fig. 5.6. At small angles, the resolution is poor, because the sweep velocity was very high, meaning low resolution in B_{\perp} at small angles. Curves for integer r have been highlighted.

5.2 Decreasing density with strong B_{\parallel}

During the high-magnetic field experiments in Grenoble we found an obvious deviation of the expected behaviour in our data: Hall traces in a strong tilted magnetic field cease to be centered about the ordinary ‘classical’ Hall line. Instead, we found *curved* traces.

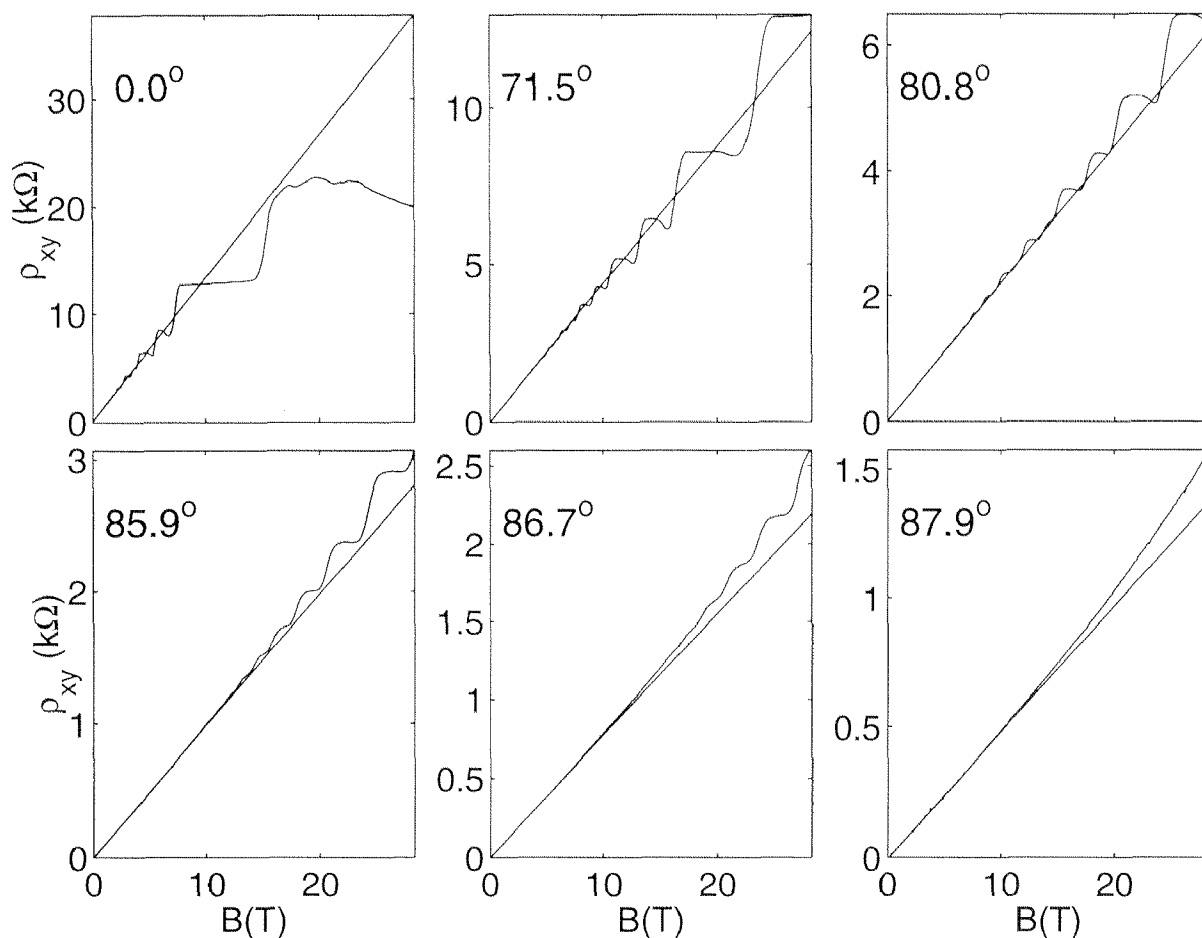


Figure 5.11: Deviation from linear Hall curve: Straight lines are linear extrapolations of ρ_{xy} from 0...4T. The density decreases at high parallel magnetic fields. Sample J.

Figure 5.11 shows this quite clearly. In perpendicular field, no deviation can be detected. There is no quantum Hall plateau for $\nu = 2$, so any deviation would be impossible to detect anyway. At 71.5° , the quantum Hall plateaux are centered around the extrapolation of the low-field $\rho_{xy}(B)$ trace. But as the tilt angle is further increased, a move to non-linear $\rho_{xy}(B)$ is evident. At 87.9° , no quantum Hall plateaux are left, but a curved line remains. The onset of the deviation from the extrapolated straight line is at about 15 T (in B_{tot}). At lower field, the effect is either not there or untraceably small, so that we never came across this in our humble superconducting magnets. The quantum Hall traces above 15 T and at high angles appear shifted to

lower field, not higher ρ_{xy} , leaving the positions of QH plateaux at the proper quantized values. Naturally, this goes along with the SdH minima belonging to each shifted plateau being shifted to lower field values, too.

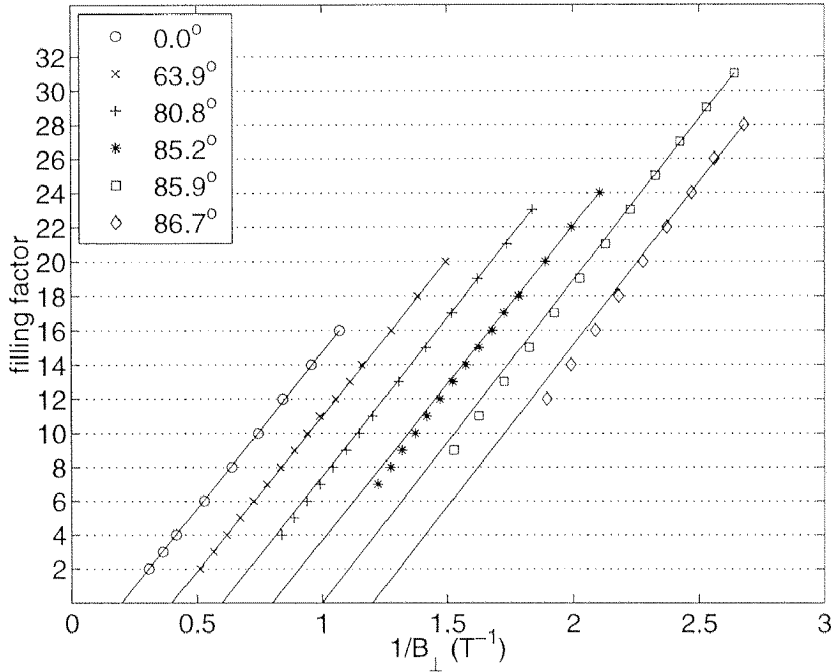


Figure 5.12: Relation of positions of ρ_{xx} minima (Symbols) in $1/B$ to the respective filling factors. As the tilt angle increases, a deviation from the straight line becomes evident. The curves are offset by a constant in $1/B$ to the left, the lines connect each curve's last point to the origin. Sample J.

Figure 5.12 shows this: positions of SdH minima in $1/B$ are plotted vs. the filling factor. At high tilt angles, the ordinary $1/B$ -dependence is no longer fulfilled. A first guess at an explanation of the effect, asymmetric Landau levels leading to asymmetric Hall plateaux (e.g. though a preferred polarity of scattering centres), is ruled out at this point, because this should leave the filling factors in their proper place in B . Instead, a decreasing total electron density in the quantum well does explain the phenomenon. It is not surprising that the ‘Hall density’

$$N_s = B_{\perp}/e\rho_{xy}(B) \quad (5.6)$$

and the ‘SdH density’

$$N_s = \nu B_{\perp}(\nu)e/h \quad (5.7)$$

yield more or less the same result even with the traces where SdH's $1/B$ dependence and the straight Hall line are broken: both, in spite of relating to altogether different physical phenomena, are related via the quantum Hall effect stating that $\rho_{xy} = h/e^2\nu$. (ref. sect. 2.3).

Figure 5.13 shows a large number of SdH minima, represented as x's, converted to electron density using relation (5.6), and ρ_{xy} traces, converted to electron density using relation (5.6). There is no perfect match of all the data, which is not surprising: a small offset in ρ_{xy} , due to an ρ_{xx} contribution, spoils

the precision of (5.6), and the positions of SdH minima have all been determined ‘by the eye’, which is, while being the best way to do it, not free of error. However, there is a clear indication of decreasing N_s for large values of α and B .

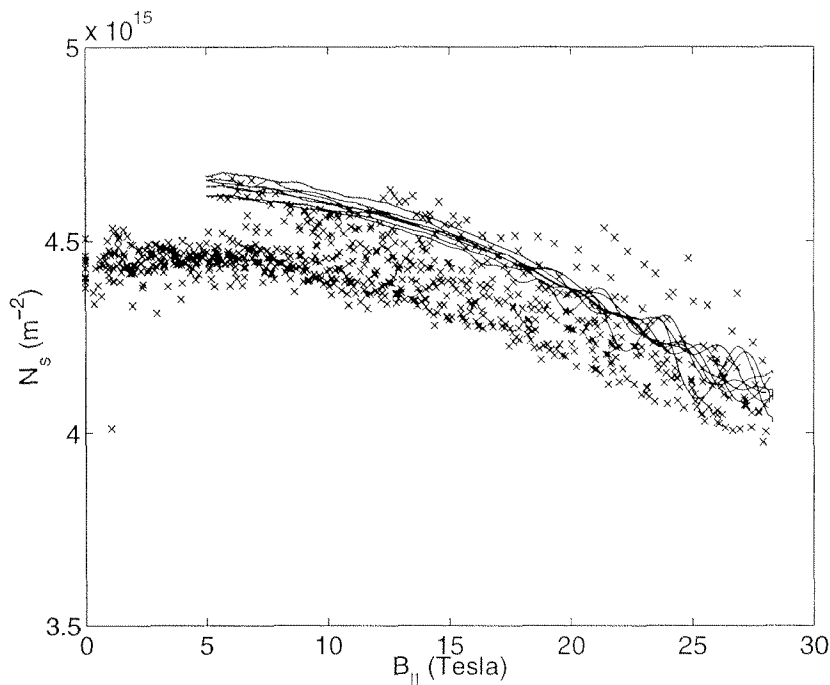


Figure 5.13: Decreasing N_s with parallel magnetic field. Each cross represents a SdH minimum, plotted at the respective parallel field vs. $\nu B_{\perp} e/h$, the lines are ρ_{xy} traces from Fig. 5.11, plotted as $B_{||}$ vs. $B_{\perp}/e\rho_{xy}$. Sample J.

5.3 Failure of the Simple Coincidence Model

5.3.1 Cross-over from Even to Odd SdH minima at constant angle

In sample L, with the field tilted about 78.2° , a significant deviation from the effects described so far occurs: at *constant angle*, there is a cross-over between even-integer and odd-integer SdH minima. Consider, as an example, the inset in Figure 5.14. This is where in large fields one observes the coincidence with matching spin and Landau gaps, with one unpaired spin-split Landau level occupied below E_F , and thus minima at odd filling factors. In the experiment shows a strikingly different picture: at low fields, up to $B_{\perp}=0.75$ T, minima occur at *even* filling factors, there is a region where the ρ_{xx} amplitude is strongly damped, and above 0.85 T minima occur at odd filling factors as expected. In the greyscale image of Figure 5.14, minima are represented as black areas, and dotted lines are drawn for even-integer filling factors. In the vertical axis, the tilt angle is plotted as $1/\cos(\alpha)$, which means that the parallel field increases linearly in the vertical. The area where the cross-over takes place can be seen as a horseshoe shape: away from 78.2° , (and $r = 1$ in

the sense of (5.1)), the crossover B_{\perp} grows.

Sample J, at the same tilt angle and magnetic field, does not show this behaviour at all: the odd ν minima persist right down to the lowest field where SdH oscillations are discernable. But, there is at least some indication that the angle of coincidence $r = 1$ is not as clearly defined as it may seem at first: the trace in Fig 5.4 with maximum SdH amplitude around $B_{\perp} = 0.8$ T is at 77.6° , but the maximum at 1.8 T still has a noticeable dent from spin splitting, while the 79.8° trace has no dip there: the point of $r = 1$ coincidence depends on B as well as on α . For the $r = 1/2$ coincidence, this is studied in detail in section 5.4.

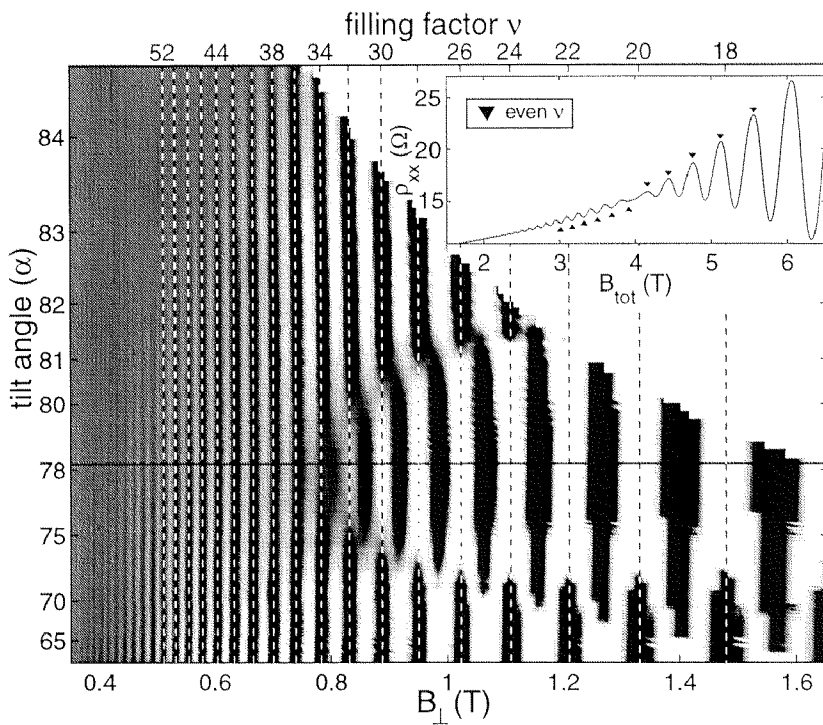


Figure 5.14: ρ_{xx} data vs. tilt angle represented as greyscale. Black represents a minimum. Data was processed heavily to increase contrast: the slowly-varying background was subtracted, and the oscillation amplitude at low fields was blown up. In the inset, one actual ρ_{xx} trace is shown, the one marked by the horizontal line in the image. Here, ‘raw’ data is displayed. Symbols point to even filling factors: minima at low fields, maxima at higher fields. Sample L.

Non-parabolicity, be it in the form of (5.2, 5.3), or in more complicated models involving more bands, causes the otherwise linear dependence of the energy of any Landau state of the magnetic field to become curved. It can thus happen that energy levels cross at constant angle when B is varied. This can lead to nodes in the SdH oscillations, like they are seen in Figure 5.14. However, non-parabolicity is only expected to lead to smoothly-varying Landau and spin levels, leading to smooth transitions from even to odd minima, unlike the experimental data suggests here. Additionally, in the two-band model the nodes always move monotonously in B with changing angle, the ‘horseshoe’ shape in Figure 5.14 can not be reproduced in this approximation.

5.3.2 Level Anticrossing

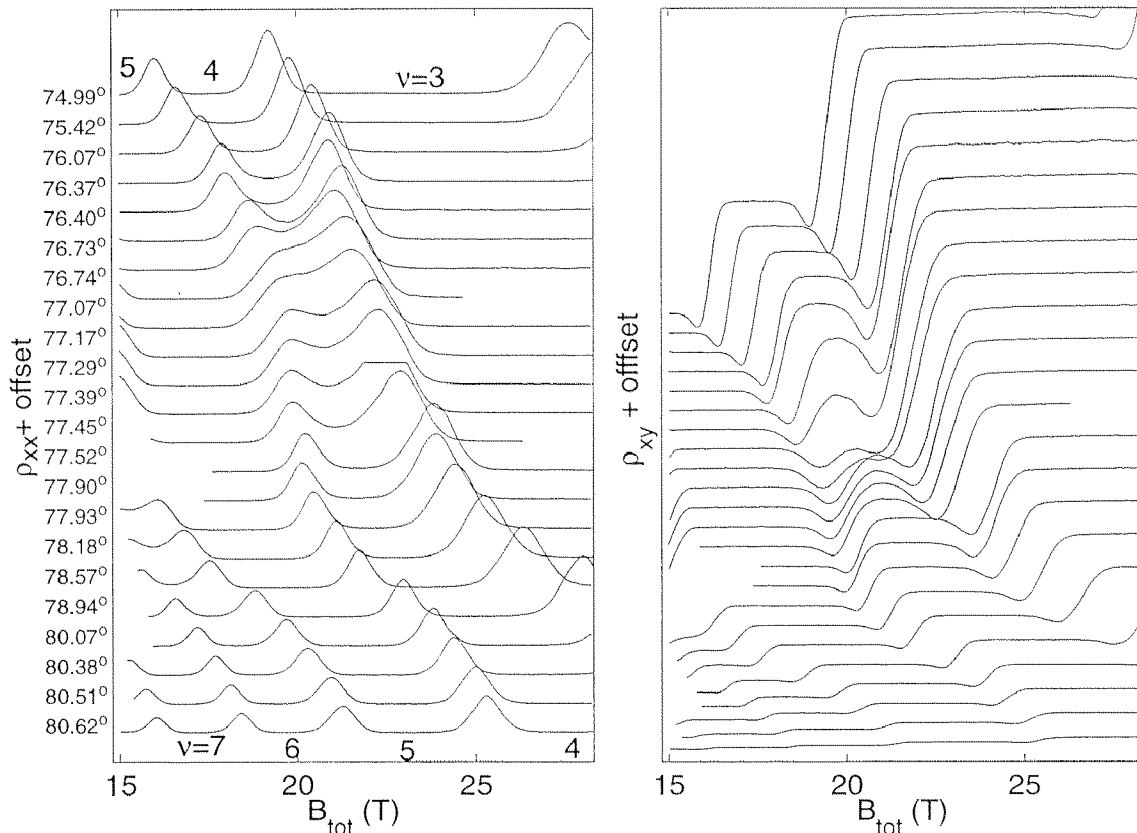


Figure 5.15: ρ_{xx} and ρ_{xy} for various angles traces around coincidence situation where $\hbar\omega_c = g\mu_B B$. Data is offset in vertical direction for clarity. The top trace ($\alpha = 75^\circ$) shows filling factors 5, 4, 3, in the bottom one ($\alpha = 80.6^\circ$) only 7, 6, 5, 4 remain. The angle has not been varied equidistantly, as can be seen from the variation of the positions of maxima. Around the centre, the angle has been adjusted by the smallest possible amount, less than 1/10 of a degree. Sample J.

When the coincidence situation $r = 1$ is met and the magnetic field is such that an even filling factor is reached, two levels with opposite spins and adjacent Landau quantum numbers lie at the fermi energy, only one of which is filled. Thus, a maximum in ρ_{xx} is expected. Generally, with large filling factors this is what we observe. In 5.10, a slight deviation from this behaviour becomes obvious: the maxima of ρ_{xx} at angles around 78° , where $r = 1$, are strongly asymmetric and have a ‘dip’, indicating a small residual splitting. Going to very high fields and low filling factors, this becomes even more obvious. For Figure 5.15, the angle was varied in the smallest possible increments around $r = 1$. At no angle, a perfect coincidence at $\nu = 4$ can be achieved. Data from sample L is even clearer on this point: the extension of Figure 5.10 to higher

fields is displayed in Fig. 5.16. Here, $\nu = 6$ is the smallest filling factor we could observe at $r = 1$ (the angle of which being greater in this sample). It is very clear that no coincidence happens. Even up to filling factors of 14 or 16, a dip remains visible in the SdH maximum.

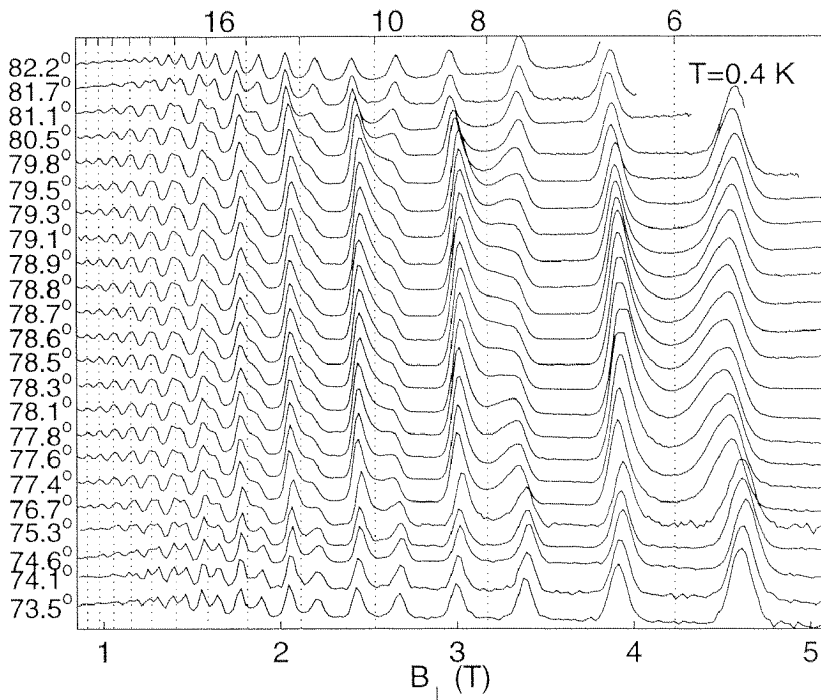


Figure 5.16: ρ_{xx} data at angles around the coincidence situation $r = 1$. At $\nu = 6$, ρ_{xx} is almost zero even where the coincidence $r = 1$ is nominally met and even minima are expected to vanish in the simple coincidence picture (Sample L).

From these pictures alone, it is not possible to determine the size of the remaining gap. For that, temperature-dependent measurements would be necessary¹. One way to get a rough idea on the size of the residual gap is to compare the shape and depth of the residual ρ_{xx} minimum at $r = 1$ with that of ρ_{xx} minima at $r = 1/2$. It is found that minima are equally distinct at $r = 1/2$ and $\nu \sim 12$, and $r = 1$ and $\nu = 6$, in sample L (Fig. 5.16). So, since the gap at $r = 1/2$ is $\hbar\omega_c/2$, and the filling factor for a similar-looking minimum is roughly doubled, it follows that the residual gap is roughly $1/4$ of the full Landau gap.

We have performed a model calculation of ρ_{xx} using the machinery described in sec. 2.4, where the Landau ladder has been modified for anti-crossing states. The model uses a Landau ladder of the form given in Fig. 5.17.

This is merely a first guess and has no deeper physical foundation, but it is convenient to use. The anticrossing parameter, estimated above to be around $1/4$, was actually chosen as 0.29 for a picture which best reproduces the data. The asymmetry of the SdH peaks is not included in the model, as well as other

¹which we could not do in the available time in Grenoble

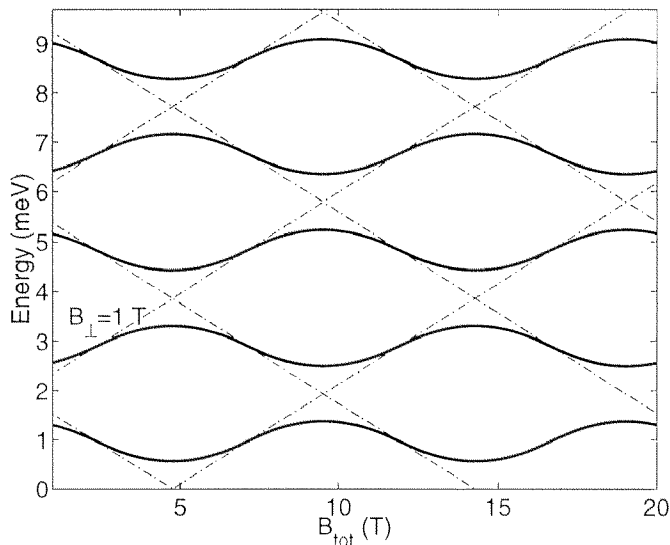


Figure 5.17: Modelled anti-crossings for Fig.5.18, in a picture comparable to Fig. 5.3. The dash-dotted lines represent the usual, crossing Landau levels. A smooth parabolic curve has been chosen to escape the crossings of different levels. The only parameter is the proportion of $\hbar\omega_c$ that remains as a gap where adjacent levels come closest (i.e. at integer coincidence index r).

subtleties, but it makes clear that the residual gap at $r = 1$ indeed lies in this range.

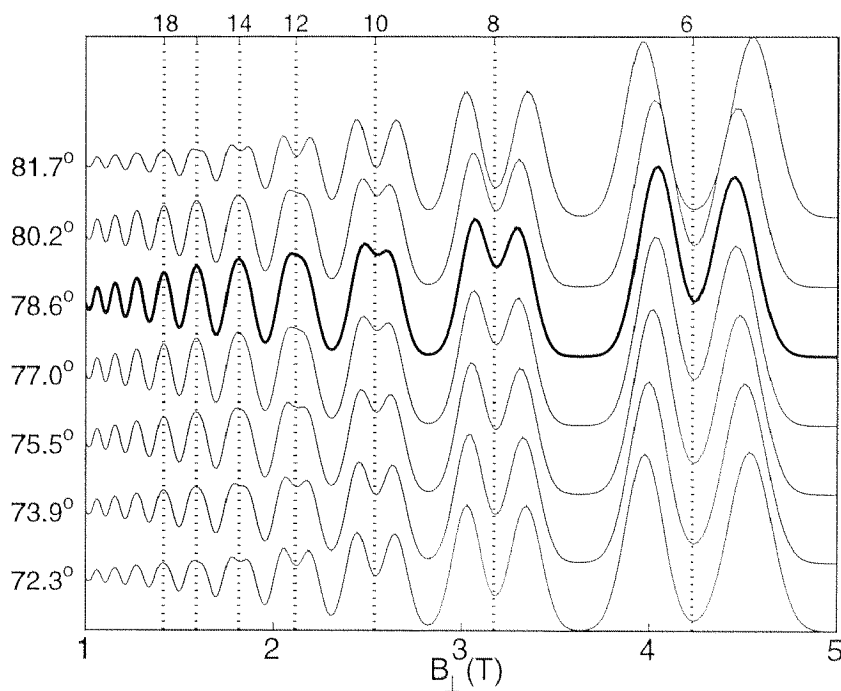


Figure 5.18: ρ_{xx} Model calculation made top best match the situation in Fig. 5.16. A residual gap of $0.29 \cdot \hbar\omega_c$ has been used to reproduce the residual even-integer gap for $\nu = 6$ and 8 at coincidence $r = 1$ (strong line). Sample L.

Figure 5.18 shows the calculated ρ_{xx} traces. The strong line is calculated for the angle where the relation $\hbar\omega_c = g\mu_B B$ is met exactly. The even- ν residual minima in this trace are weakest in this trace and increase in intensity towards larger and smaller angles. The general features of Figure 5.16 are reproduced. Apart from the omitted asymmetry of the Landau levels, more differences between the model calculation in 5.18 and the actual experiment in 5.16 are evident on close examination: the $\nu = 6$ residual minimum is deeper in the measurement, but the $\nu = 8$ minimum looks stronger in the modelled curve. At $\nu = 14$, there is still a clear ‘dent’ in the measured SdH maximum, which

is not reproduced in the model.

In a similar experiment [Koch93], Koch et al. found the minimum at filling factor 2 not to vanish with coincidence, if the Landau level broadening was small enough. They used a GaInAs/InP heterostructure. For filling factors 4 and above, coincidence could always be achieved in their sample. It remains to be said that *any* mechanism that introduces coupling between different energy levels, as for example the non-parabolicity does, could ultimately lead to an anticrossing of levels. Koch et al. ascribe the observed suppression of the LL coincidence to a first-order phase transition, as predicted in [Giuliani85], when the electron system at $\nu = 2$ crosses over from being half spin-up and half spin-down to a spin-polarized state when the spin-up half of the second LL crosses below the spin-down half of the bottom LL. At this point, according to the authors, the magnetization is unstable, because of the competing Zeeman energy and the extra energy to be paid for the ferromagnetic ordering. In a follow-up publication [Yarlagadda91] it was pointed out that the signature for this instability, in a transport experiment with sufficient electron mobility, would be the remaining of $\rho_{xx}=0$ for all angles through the $r = 1$ coincidence.

5.3.3 More B_{\perp} -dependent Structure

At very low temperatures and if measured with high resolution (i.e. sweeping the magnetic field slowly), structure appears in low field ρ_{xx} data which is no longer periodic in $1/B_{\perp}$. Fluctuations like these are displayed in Fig. 5.19. The fact that individual peaks retain their position in B_{\perp} when the angle is varied by a small amount is indicating that the two-dimensional nature of the quantum well plays a role in this effect. The fluctuations are perfectly reproducible, and remain in place even after days. When measured over a different set of contact pairs, the image changes completely, meaning that the effect could be due to the layout of scattering centres or other peculiarities of a single sample, rather than being a fundamental consequence of the quantum well material's properties. The features seem reminiscent of the magnetoconductance fluctuations in narrow wires due to phase-coherent scattering at very low temperatures, first reported by [Umbach84] and now known as universal conductance fluctuations. Our sample, $40\mu\text{m}$ wide, however, was not a narrow wire, in comparison to the phase-coherence length of these samples.

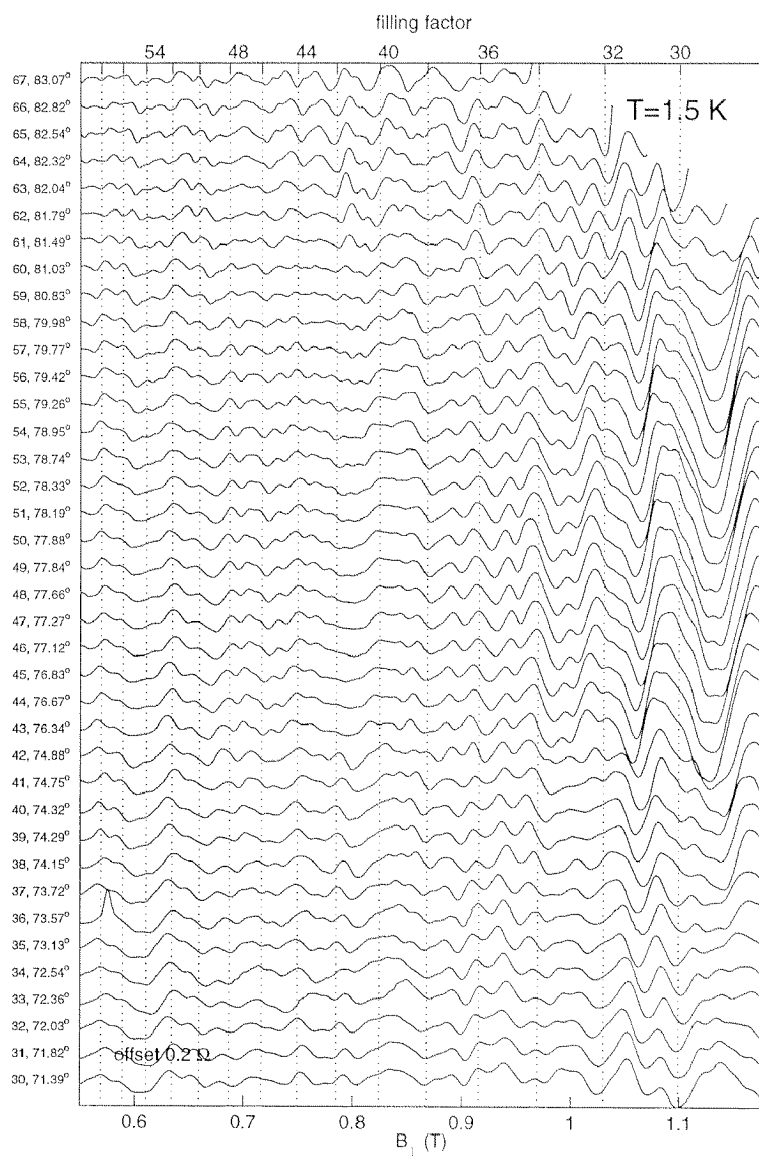


Figure 5.19: ρ_{xx} at low fields and if measured with high enough resolution, structure appears in ρ_{xx} which has no evident connection to filling factors. Individual peaks appear at a fixed position in B_{\perp} , and disappear as the angle is increased by a small amount. Sample L.

5.4 Measuring the Zeeman and Landau gap simultaneously

By recording SdH data at various angles *and* temperatures, we were able to determine the energy separation of spin-resolved Landau levels for varying B_{\parallel} . For two angles, some curves are plotted in Fig. 5.20. Data was taken at 14 temperatures from base temperature (1.69 K) to about 13 K. Great care was taken to remove an offset in the magnetic field measurement (due to delays in the instrument readout) and to determine the angle precisely: both were achieved by ensuring that ρ_{xx} -minima occur periodic in $1/B$.

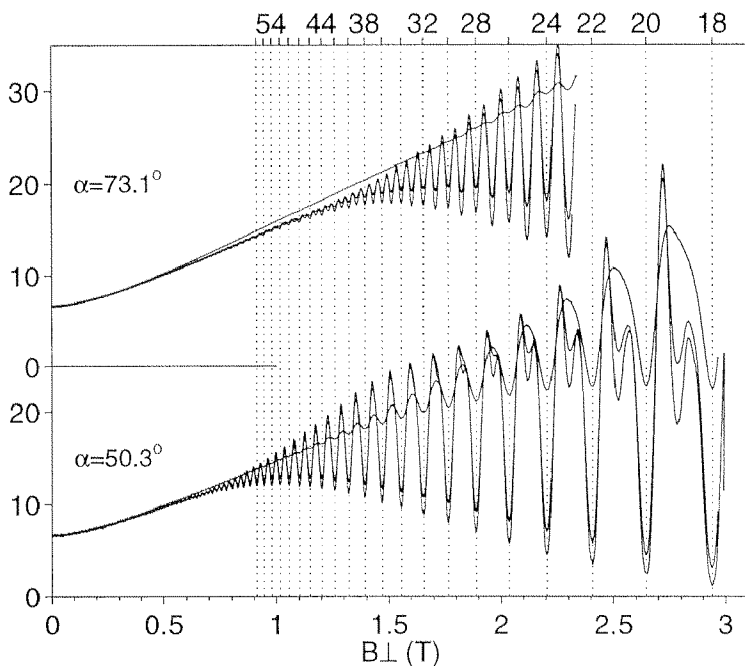


Figure 5.20: ρ_{xx} traces at 3 temperatures (1.7 K, 4 K, 13 K). Note that the minima at odd filling factors (the ones due to Zeeman splitting) are washed out at much lower temperature. This is analyzed in detail in Fig. 5.22. Data from sample F.

After this, parabolae were fitted to the $\rho_{xx}(B)$ in the region of all integer filling factors, and at half-integer ν as well, where minima occur at even and odd ν , and consequently there are maxima in between. Each ρ_{xx} minimum was assigned a ‘depth’: the difference between the ρ_{xx} value at the minimum and the average of the ρ_{xx} values at the adjacent maxima. Figure 5.21 shows where the $\delta\rho_{xx}$ values were measured.

Gap energies were computed by fitting a series of ‘depth’ values for various temperatures to the LK-formula (see 2.15). Results are given in Fig. 5.22. Filled symbols stand for fits in regions where the oscillation period is 2 filling factors: the usual, spin-degenerate SdH-Oscillations at low fields. Empty symbols indicate regions where the SdH frequency is doubled due to strong spin splitting at higher fields, diamonds for even- ν minima and circles for odd- ν minima.

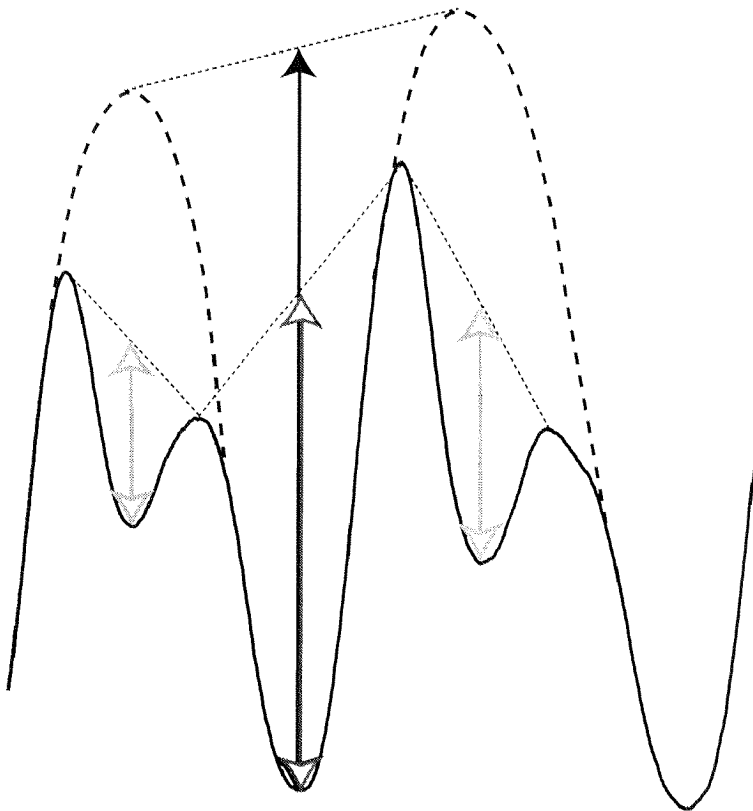


Figure 5.21: The arrows indicate how the ‘depth’ of each SdH minimum was measured. The hollow arrows measure the smaller odd- ν minima, the filled arrows measure the even- ν minima. The temperature dependence of each of the depths gives the gaps presented in Figure 5.22. Data from the previous Figure.

At $\alpha = 0^\circ$, the solid line for $\hbar\omega_c$ coincides with the filled diamonds. This is so because the effective mass was chosen to achieve that. At the angle of 72.9° the curves for even minima and the one for odd minima cross each other. We thus conclude that the relation $\hbar\omega_c/g\mu_B B = 2$ holds. Using this to find the g -factor, dotted lines for $g\mu_B B$ and dash-dotted lines for $\hbar\omega_c - g\mu_B B$, the ‘remaining’ Landau gap are plotted. The fact that these coincide with the experimental curve may be seen as a confirmation of the validity of the applied method: it works well if the gap size is effectively cut in half.

Looking closely, it can be observed that the angle of crossover, where the ‘even gaps’ and ‘odd gaps’ are equally wide, depends on the magnetic field.

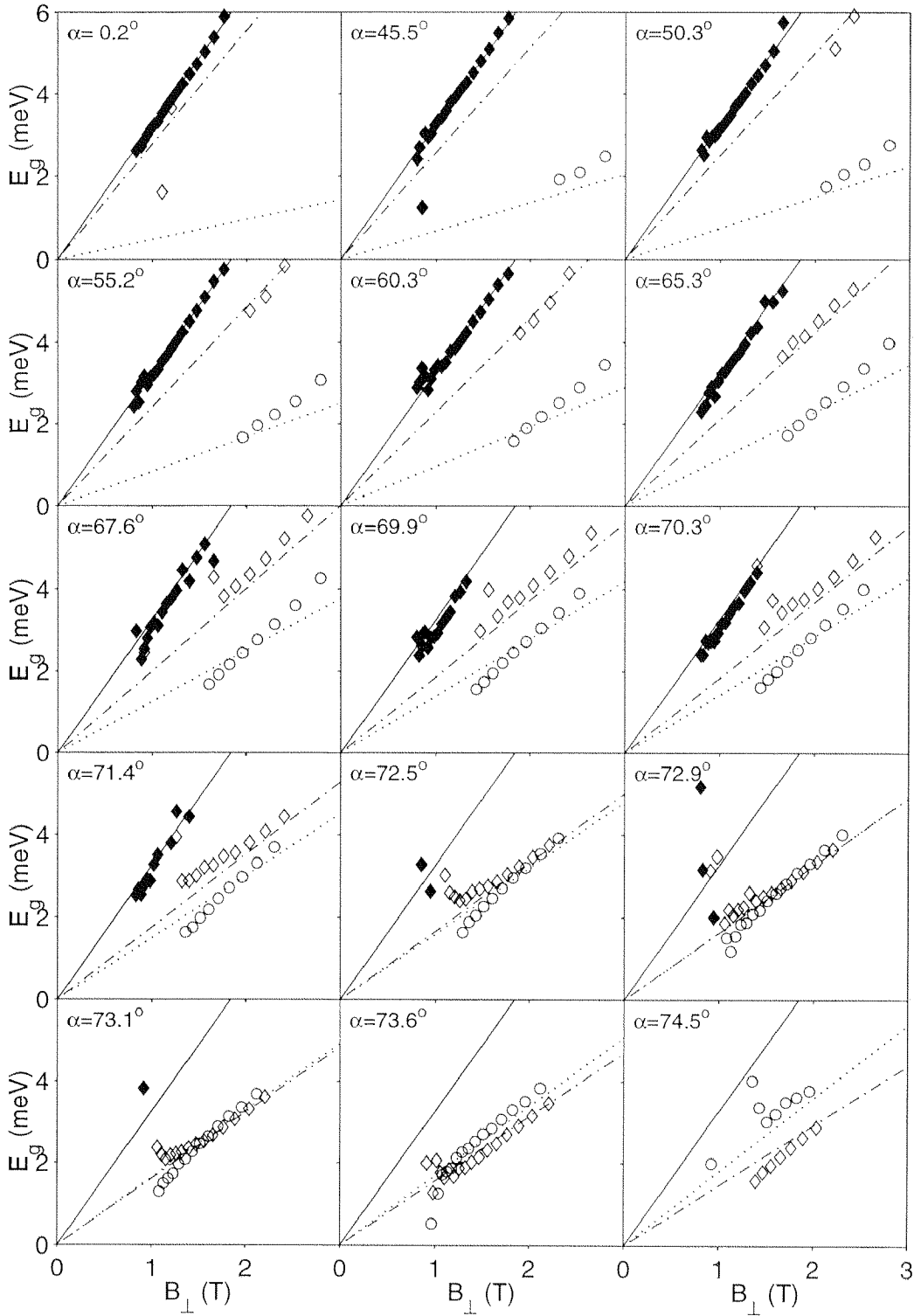


Figure 5.22: Evaluation of temperature-dependent data like in 5.20, for 15 different angles. In each plot, the solid line represent $\hbar\omega_c$, which does not depend on the tilt angle. The dashed line is the Zeeman splitting $g\mu_B B$. The dash-dotted line is $\hbar\omega_c - g\mu_B B$, the ‘remaining’ Landau gap. The symbols represent gaps fitted to the temperature-dependence of minima at individual filling factors. Diamonds stand for even ν , while circles stand for odd ν . Filled symbols are used where the SdH period is 2 filling factors, as in the spin-degenerate case, open symbols were used in the spin-split case where the SdH period is doubled.

Chapter 6

Zero-Field Spin-Splitting, and its absence

In an ideal, noninteracting 2DEG, the electron states are twofold spin-degenerate, unless an external magnetic field is applied. The Zeeman splitting, the lifting of the spin-degeneracy in an applied magnetic field, is described by the term $g\mu_B B$, with Bohr's magneton μ_B and the electron spin g factor, which has been shown to depend on many-body effects and is influenced by the crystal structure of the host system. It has been argued that the spin-degeneracy of the electron system in AlGaSb/InAs quantum well systems should be lifted even at zero magnetic field. Two mechanisms contribute to this effect:

- (a) the inversion asymmetry of the underlying zincblende crystal structure, see section 3.2.1. For this contribution, the spin splitting is proportional to k^3 .
- (b) the time-reversal asymmetry following from an electric field parallel to the surface normal of the quantum well. This is the so-called Rashba mechanism, with the spin splitting proportional to k .

In small-bandgap semiconductors, the Rashba mechanism is believed to dominate, while in GaAs, for example, the bulk-inversion asymmetry is the most important contribution to the zero-field spin splitting [Lommer88]. A possible application has been proposed in [Datta90], in the form of a device where spin-polarized electrons are injected from ferromagnetic contacts, and a conductivity modulation is achieved by the application of an electric field. Recently, experiments have been successful with such a 'spintronic' device [Gardelis99]. However, a magnetic field is needed to induce the spin-valve effect. The authors claim that the two-state nature of spin systems makes this device a candidate for the implementation of a quantum computer.

An expected experimental manifestation of the zero-field spin splitting is a beating pattern in SdH traces. The effect are not a unique property of InAs/AlSb wells: Nonzero spin splitting at $B \rightarrow 0$ has been demonstrated in $\text{In}_x\text{Ga}_{1-x}\text{As}/\text{In}_{0.52}\text{Al}_{0.48}\text{As}$ heterostructures [Das89, Das90]. In the high-density 2DEGS, up to six beat nodes could be observed in $\rho_{xx}(B)$. In the InAs/GaSb system, similar experiments have been shown, [Luo88, Luo90] and the results were related to the Rashba spin splitting. Gate-controlled $\text{In}_x\text{Ga}_{1-x}\text{As}/\text{InP}$ [Engels97] and HgTe [Schulz96] quantum wells show the same behaviour, here the spin splitting can additionally be tuned by application of a gate voltage. Some inconsistencies between different samples from the same wafer remain in a study of InAs/AlSb quantum wells [Heida], also controlled by a metallic front gate: the measured spin-splitting parameters are different in different samples. The conductance quantization in 1D-wires also changes in the presence of a lofted spin-degeneracy, as has been shown experimentally [Thomas96, Tscheuschner96].

We have conducted several experiments where this beating pattern clearly fails to occur. We can thus give an upper limit to the zero-field spin splitting, if it exists in the samples at all.

There are other mechanisms that can produce beating patterns in magnetoresistance oscillations. Transport in more than one subband yields a separate oscillation period for each of these. Rarely, however, the densities and scattering times in two subbands will be nearly equal, which is the obvious prerequisite for beating patterns with clear nodes separated by many oscillations of the SdH period. Secondly, if the electron density varies across the area probed by the experiment, different regions can contribute different oscillations, all of which combine to the resulting magnetoresistance trace. Common sense would suggest that this will lead to a strong damping in the oscillations, since adjacent regions will have slowly-varying densities. We have observed instances of these inhomogeneity-induced beating patterns with two periods.

6.1 Theory of zero-field spin splitting

6.1.1 Rashba term calculated in the $\mathbf{k} \cdot \mathbf{p}$ approximation

$\mathbf{k} \cdot \mathbf{p}$ theory was developed as a technique to calculate an approximation for the electronic structure of solids at extremal points in \mathbf{k} -space. At symmetry points, i.e. at points where the Hamiltonian exhibits some form of rotational symmetry, the corresponding wave function transforms according to the respective symmetry group. The particular “point of interest” in cubic semi-

conductors is the Γ -point ($\mathbf{k} = 0$). Electronic states can be classified as being s-type, p-type and so on, very much like in atomic states. Input to $\mathbf{k} \cdot \mathbf{p}$ is detailed information about the dispersion of each of these states, while as a result one obtains the energy level structure of the system in proximity to the \mathbf{k} -point considered.

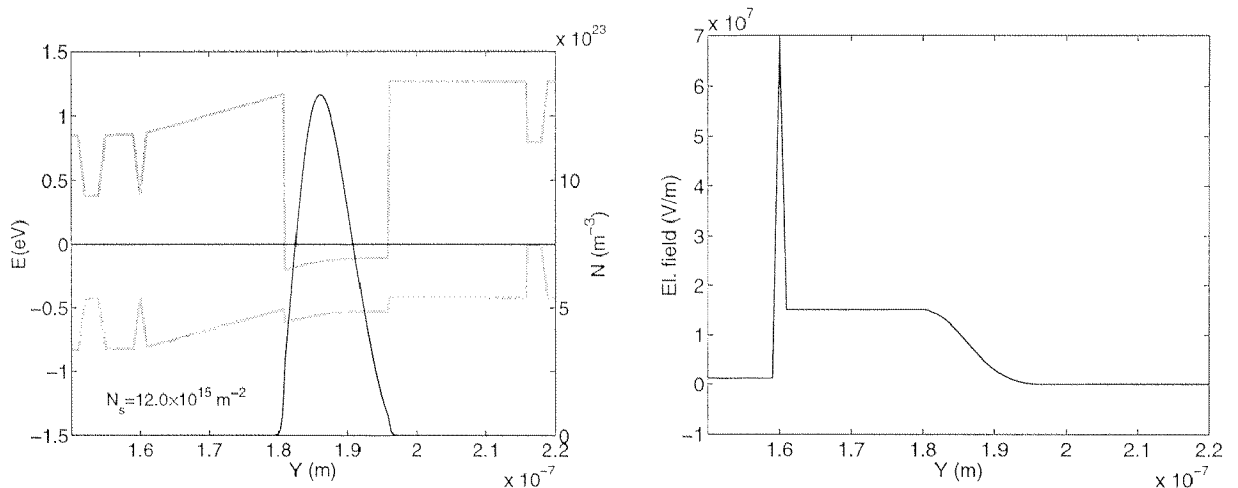


Figure 6.1: Calculated band edges, carrier distribution(left) and electric field (right) in Sample F. The δ doping layer sits at 160 nm approx., leading to a spike in the calculated field. Over the quantum well (from 180 nm to 195 nm) the field drops from 10^7 V/m to essentially zero.

As a result of this calculation, da Silva [eSilva94] states for the energy level structure in the conduction subband of the narrow-gap III-V compounds

$$\epsilon = \left\langle f_{\pm} \left| \frac{\hbar^2}{2m^*} \left(\frac{d^2}{dx^2} + k^2 \right) - a \frac{\left[\frac{\hbar^2}{2m^*} \left(-\frac{d^2}{dx^2} + k^2 \right) \right]^2}{E_g + \Delta} + V(z) \mp \alpha k \right| f_{\pm} \right\rangle \quad (6.1)$$

where the non-parabolicity constant a is

$$a = \frac{(2E_g + \Delta)^2 + E_g^2}{E_g(3E_g + 2\Delta)},$$

and the spin-splitting parameter

$$\alpha = \frac{\hbar^2}{2m^*} \frac{\Delta}{E_g} \frac{2E_g + \Delta}{(E_g + \Delta)(3E_g + 2\Delta)} eE$$

is the Rashba spin-orbit coupling parameter for an electric field in the z -direction only. The wave function used to evaluate this in [eSilva94] is the Fang-Howard function for heterointerfaces. We use the wave function envelope obtained from the Poisson-Schrödinger-Solver (see Figure 6.1) and obtain a value of 3.9 meV for the spin splitting $2 \langle f | \alpha k_F | f \rangle$.

6.2 Experiments

To clarify whether or not beating patterns in the magnetooscillations exist, we looked at the low-field SdH traces of several samples, with different carrier densities, and different built-in electric fields.

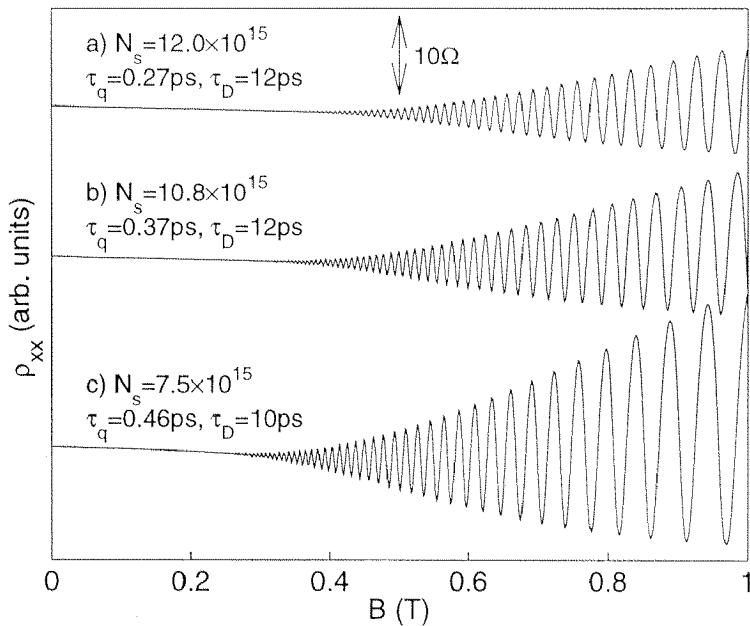


Figure 6.2: SdH oscillations for various carrier densities achieved by illuminating the sample. In spite of the high measurement resolution, no beating patterns can be observed. Sample F.

6.2.1 Modifying the carrier density by illumination

By using a red or infrared LED the carrier density can be reduced in InAs/AlSb quantum wells. This effect, known as the negative photoconductivity, is described in Chapter 8. The sample used is F (see p.95), a high carrier density sample with one-sided doping. Due to the strongly asymmetric layout of the sample, with dopants on the surface side of the well only, one expects a strong electric field across the well. A calculation of the band edges using the 1D-Poisson-solver [Snider90] yields an electric field of about 10^7 V/m. Here, we have ascribed a contribution of $4 \cdot 10^{15} \text{ m}^{-2}$ electrons to the bulk and interface donors, which are symmetrically distributed and do not give a net electric field, and the rest to the donor layer, (the surface electrons not playing an important role, since the cap layer is 210 nm thick). The result of this calculation is given in Fig. 6.1. The initial carrier density is about $12 \cdot 10^{15} \text{ m}^{-2}$ at cooldown, by illumination it can be brought down to $7 \cdot 10^{15} \text{ m}^{-2}$.

We observed SdH-oscillations at various densities in this range, but no indication of a beating pattern could be observed. Figure 6.2 shows some typical results: with the carrier density decreasing from a) to c), the overall appearance of the pattern does not change at all.

6.2.2 Changing the carrier density by hydrostatic pressure

Essentially the same picture is obtained when we change the carrier density by applying hydrostatic pressure: no indication of a beating pattern is observed. Experimental results (using sample N, see p. 97) are shown in Fig. 6.3.

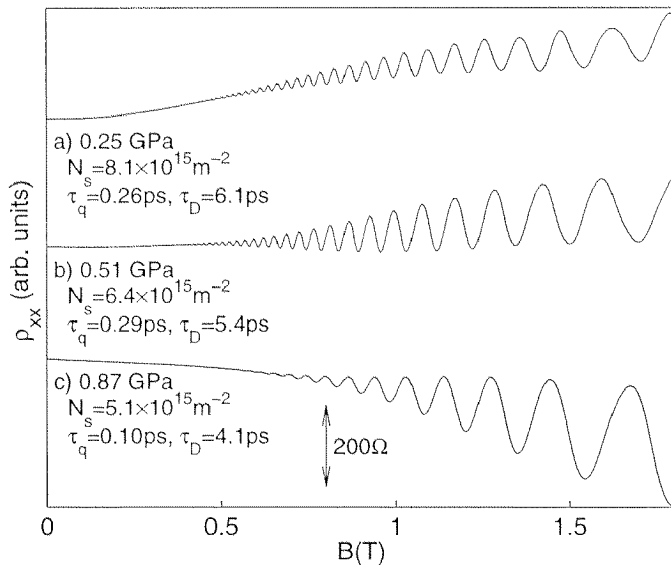


Figure 6.3: SdH traces for 3 different N_s , obtained by applying hydrostatic pressure. The same negative result: no indication of a beating pattern. Sample N.

There is an observable change in slowly-varying background magnetoresistance, which actually changes its sign from positive to negative as pressure is increased. This may be due to an increase in contact resistance with pressure. With this particular sample, contact resistance increased at even higher pressures to values that render transport measurements of the 2DEG impossible.

6.2.3 SdH beatings induced by inhomogeneous illumination

In some cases, though, we did find a beating pattern in the oscillations. Especially when the part of the sample that was electrically connected to have its ρ_{xx} measured was relatively large, in some cases a beating pattern was seen. Upon further illumination this beating vanishes completely, and it cannot be reproduced in every cooldown cycle. Possibly it is due to an uneven illumination in the tiltable sample stage, depending on the angle. Details are stated in section 8.3.

If a beating pattern were due to Rashba-type spin splitting, and the density changes from high to lower, there is no way that the beating pattern should appear at a specific density and vanish again at lower densities: the electric field, which causes such a splitting, can only decrease or change its sign while N_s goes down. The opposite case, where a beating pattern vanishes with decreasing N_s and then shows up again at still lower density could be explained by the

expected change in electric field, but it does not happen in the experiment.

From a single ρ_{xx} trace like in Fig. 6.4, it is more or less impossible to judge whether the beating pattern comes about through an inhomogeneous carrier density or through a physical effect like zero-field spin splitting. In the chapter on illumination, a whole series of B -sweeps for subsequent states of illumination is shown: Figure 8.1 on page 87. The carrier density is decreased in steps from $12.5 \cdot 10^{15} \text{ m}^{-2}$ down to $8.1 \cdot 10^{15} \text{ m}^{-2}$. The electric field over the quantum well decreases proportionally with N_s . If the electric field was responsible for the beating pattern, the intensity of beats would decrease with the density. Only when the electric field is reversed, where the donors in the bottom barrier outweigh the donors from the cap, a beating pattern could emerge again. This behaviour is not observed, beats occur and disappear randomly after illumination. The pattern also changes as a function of time, when the sample is left for some hours, as a redistribution of donors appears to take place. In the case of measurements like those of [Engels97], there is no doubt that a Rashba-type spin splitting has been observed: The splitting changes with an applied electric field, all explained well by the Rashba theory. There are, however, other experiments where one could imagine that an unfortunate coincidence like an inhomogeneous carrier density could lead to false conclusions.

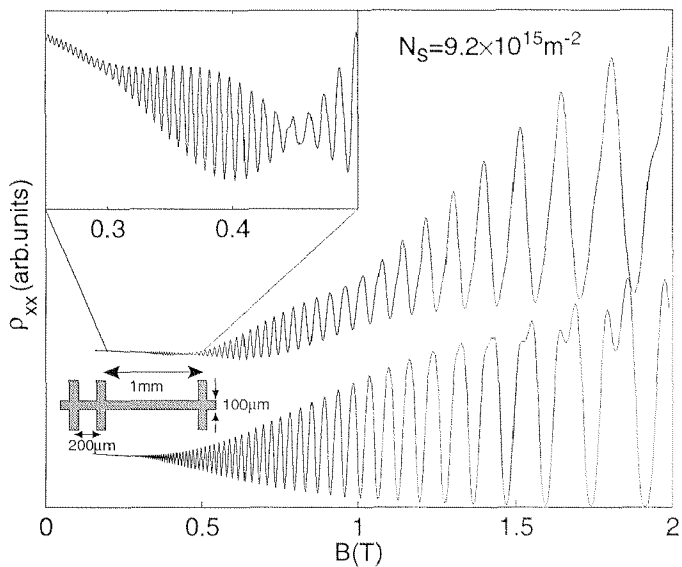


Figure 6.4: SdH oscillations for one carrier density, measured at different places along the same hallbar. The upper curve was measured along the 1 mm pair of voltage probes, the lower curve was measured along the 50 μm pair. The inset magnifies the low-field details of the beating pattern. Sample F.

There is another lesson to be learned from this: any experiment that evaluates the amplitude of SdH oscillations is prone to suffer inaccuracies when there are regions of unequal carrier density involved. If the effect is not strong enough to lead to a beating pattern, the shape of the SdH envelope curve can still be substantially modified.

6.2.4 More beats

Sample B is a high-density InAs/AlSb quantum well, similar to F but with bulk doping in the cap, and with even higher carrier density. Magnetotransport traces for Sample B look rather complicated: there is a beating pattern with nodes at 0.6 T, 0.9 T (see insert) and one just below 2 T (main graph) in Figure 6.5. Above 2 T, interference with a third period appears. This behaviour is there in all individual pieces of sample B, which makes it unlikely that it is only an effect of inhomogeneity as in Figure 6.4. Data in Figure 6.5 has been averaged from two B -sweeps, and symmetrized, i.e. $\rho_{xx} = (\rho_{xx}(B) + \rho_{xx}(-B))/2$.

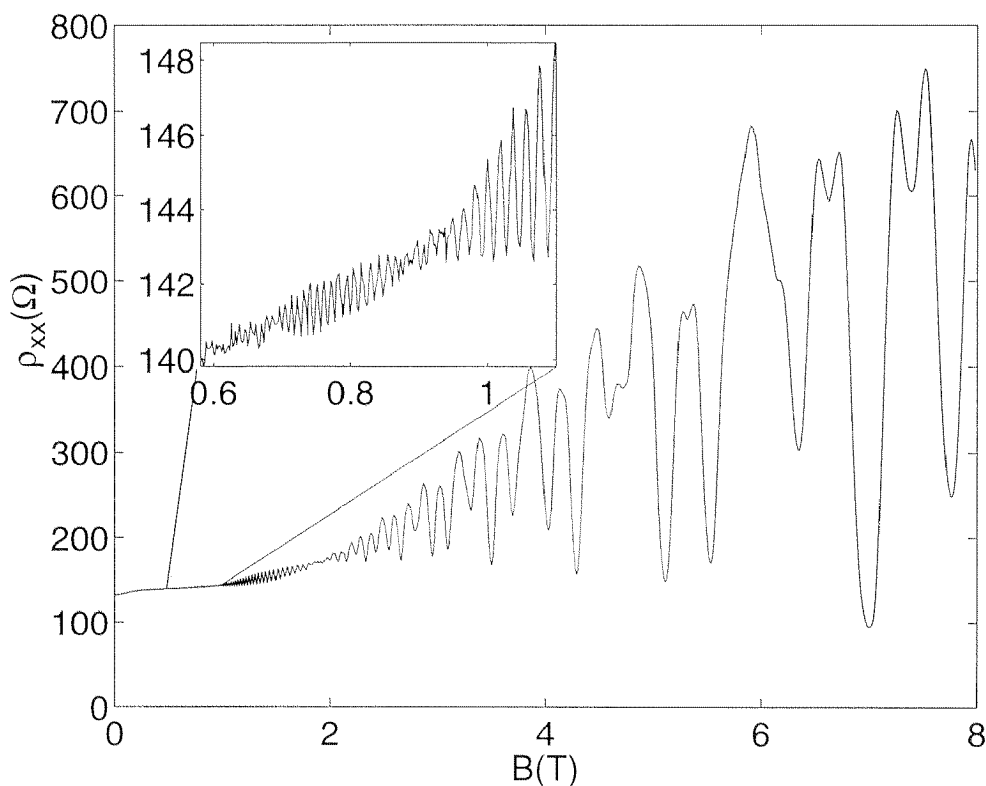


Figure 6.5: At low magnetic fields, sample B exposes a beating pattern in the SdH oscillations. The electron density as found from the Hall resistance at low fields is $3.85 \cdot 10^{16} \text{ m}^{-2}$.

The Hall electron density is $N_{\text{Hall}} = 3.85 \cdot 10^{16} \text{ m}^{-2}$ in sample B. The SdH period of the small period oscillation (in the range $[0.6 \text{ T} \dots 2 \text{ T}]$) yields a density of around $2.7 \cdot 10^{16} \text{ m}^{-2}$. If the beating was due to two electric subbands, the total density would be $5.4 \cdot 10^{16} \text{ m}^{-2}$ from these two bands alone, which is incompatible with N_{Hall} . To attempt an interpretation of Figure 6.5, a Fourier transform has been made of the SdH data (re-sampled equidistantly in $1/B$).

Figure 6.6 shows the Fourier transform for two different ranges of magnetic field. One possible interpretation of the spectral lines that are visible is indicated in the plot: One subband with $1.06 \cdot 10^{16} \text{ m}^{-2}$, and another with $2.7 \cdot 10^{16} \text{ m}^{-2}$, the latter being spin-split into two different densities. This splitting is clearly visible in the low- B data on the left side of Figure 6.6. The trans-

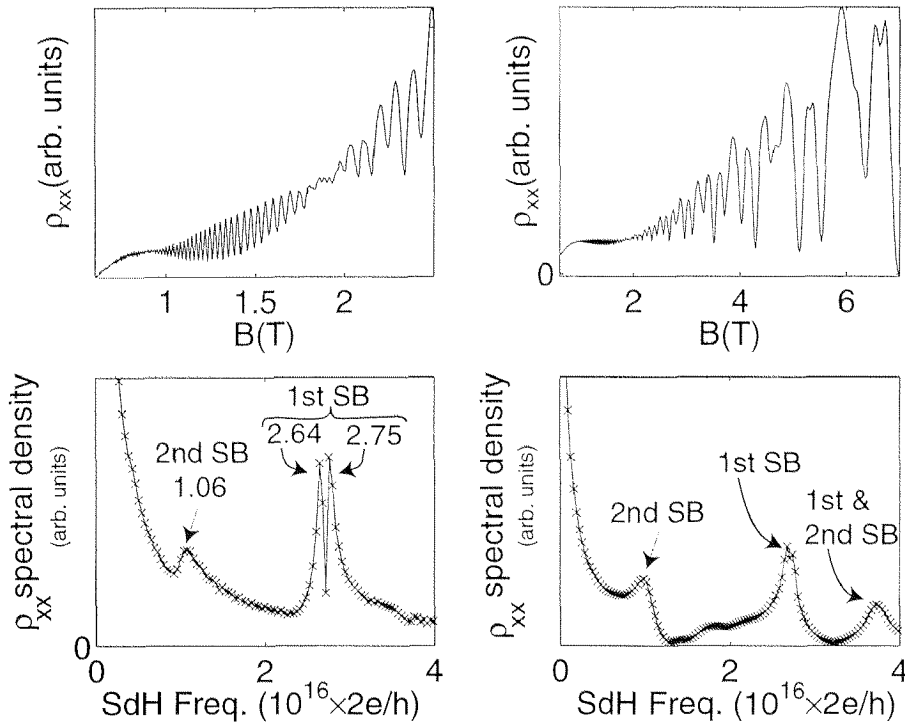


Figure 6.6: Fourier analysis of the data in Figure 6.5, for 2 different ranges of magnetic field. Left: [0.6 T... 2.5 T]. Right: [0.6 T... 7 T]. The top graphs give the ρ_{xx} data after re-sampling, Fourier transform, and reverse-transform. The bottom graphs show the power spectra of $\rho_{xx}(B^{-1})$. Two densities are visible, with one of them split into two lines.

form that includes the higher magnetic fields does not show the splitting as clearly. Instead, the sum of the two densities form another peak at $3.8 \cdot 10^{15} \text{ m}^{-2}$. The appearance of a sum frequency can be an artifact of the Fourier method. The sum of the three densities, taking into account the spin-resolved lower subband, are $[(2.64+2.75)/2+1.06] \cdot 10^{16}, \text{ m}^{-2} = 3.76 \cdot 10^{16} \text{ m}^{-2}$. This value approximately matches the measured Hall density of $N_{\text{Hall}} = 3.85 \cdot 10^{16} \text{ m}^{-2}$. There may be other ways of interpreting this data, but together with the total density N_{Hall} that has been found in the experiment, this gives a consistent image.

We follow Das, Miller, Datta et al. in the following procedure to determine the zero-field spin splitting from the position of beat nodes [Das89]. The highest-field node is where the spin splitting δ is just 1/2 the Landau splitting $\hbar\omega_c$. In general, the i th node (with i increasing to lower fields) occurs where

$$\delta(B) = \hbar\omega_c(i + 1/2) \quad (6.2)$$

holds. From the B -field where nodes occur, a plot of $\hbar\omega_c$ vs. $\delta(B)$ can be made. The Ansatz for the total spin splitting is

$$\delta = \delta_0 + \delta_1 \hbar\omega_c + \delta_2 (\hbar\omega_c)^2 + \dots, \quad (6.3)$$

but all but the first two terms may be omitted in small magnetic fields. The remaining linear relationship allows an extrapolation to $\omega_c = 0$ and thus, from the plot of $\hbar\omega_c$ vs. $\delta(B)$, the zero-field spin splitting δ_0 can be determined.

Figure 6.7 shows this evaluation for data from Figure 6.5. The smallest- B beat node is not well-resolved in the original data, and so the error margin is quite large. We estimate δ_0 to be $7 \pm 0.5 \text{ meV}$.

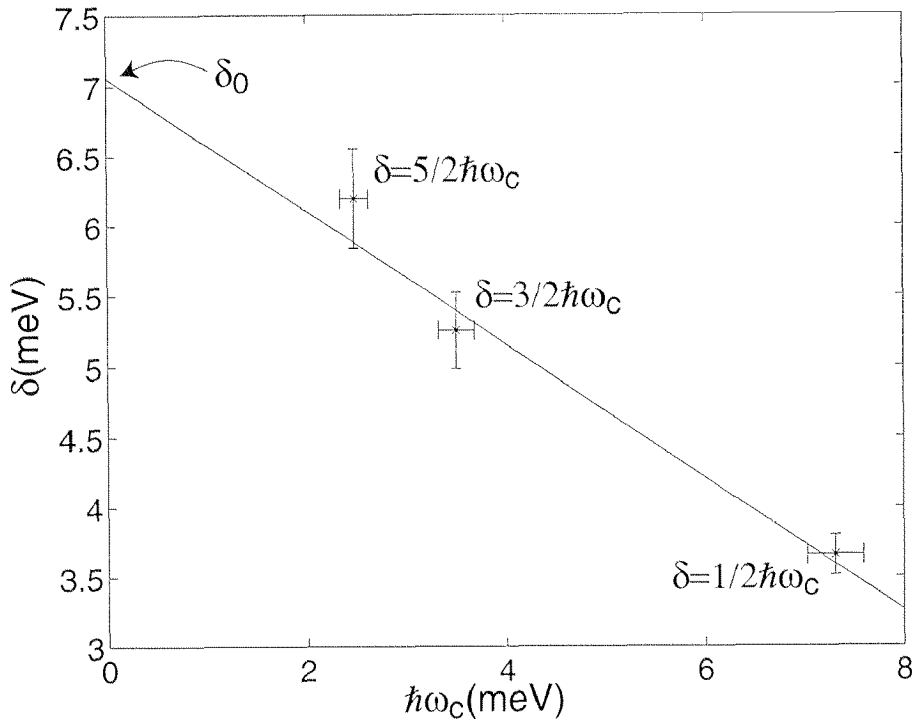


Figure 6.7: Cyclotron energy at the beat nodes (in Figure 6.5), plotted vs. the spin splitting $\delta(B)$. The intercept of the line fit with the $\hbar\omega_c = 0$ axis gives the zero field spin splitting δ_0 , 7 ± 0.5 mV in this case.

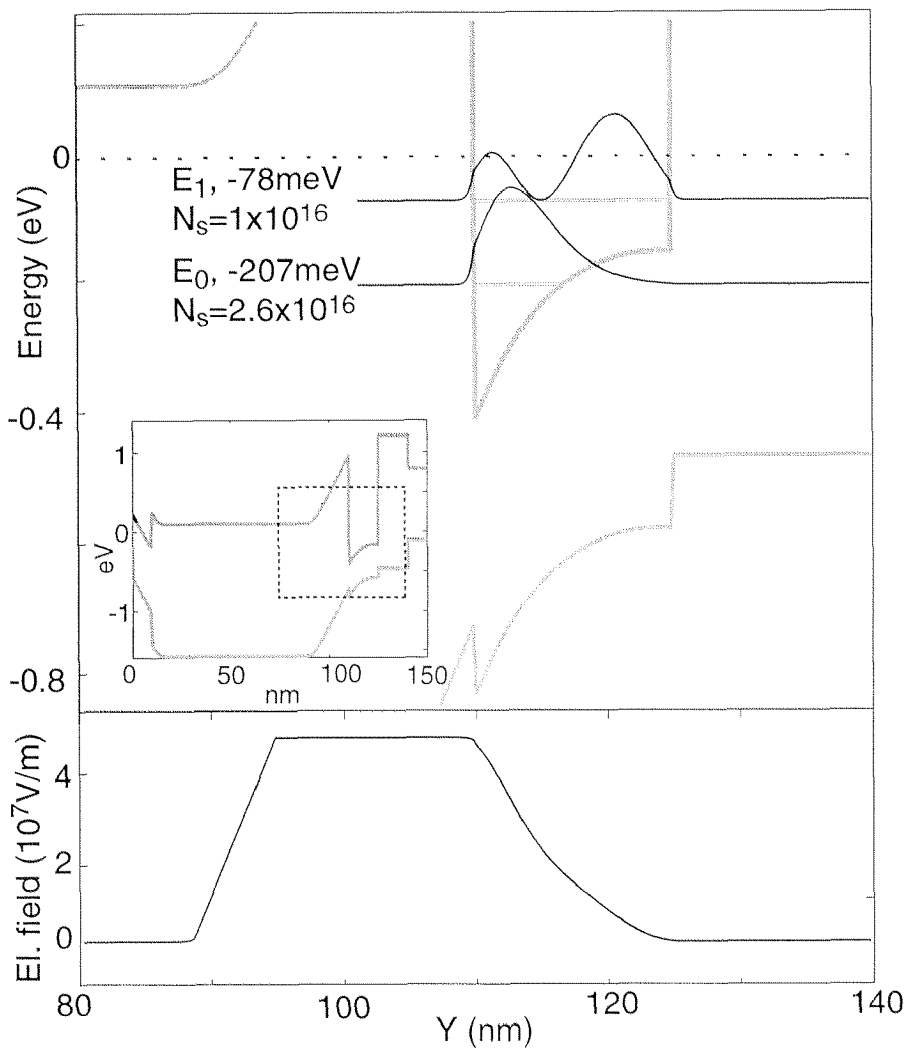


Figure 6.8: Band structure calculation for sample B. The electron density in the quantum well is so high that two electric subbands are filled. The inset shows the structure of the whole sample, while the main picture is a magnification of the active region, with both energy levels and their respective squared wave functions displayed (top). The lower part displays the strength of the electric field perpendicular to the sample normal. The field is three times as strong as in sample F, Figure 6.1.

Figure 6.8 displays the calculated band structure [Snider90] for sample B. The strong bulk doping in the top barrier pulls the conduction band edge in the doped region right down to the Fermi edge (see inset). The calculation finds two occupied subbands with densities similar to those proposed in Figure 6.6. The electron distributions in both subbands are strongly asymmetric, the lower band being biased towards the cap, the upper more towards the substrate side. The calculation also yields the electric field strength. The magnitude of the electric field is almost proportional to the carrier density, which is obvious because nearly all of the carriers in the well have their donors on the cap side of the sample.

This value can be compared to the result out of equation (6.1). The calculation, using the lower subband wave function and the field distribution from the Schrödinger/Poisson Solver, results in $\Delta_{\text{spin}} = 30 \text{ meV}$ for the total spin splitting ($\langle \psi_1 | \alpha k_F | \psi_1 \rangle$ in the sense of equation 6.1). Hence, the measured zero-field spin splitting in sample B is detectable, but once again it is much smaller than the value expected from theory.

Chapter 7

Effect of hydrostatic pressure on InAs/AlSb quantum wells

This chapter describes experiments on InAs/AlSb quantum wells at hydrostatic pressure. First, the pressure-related properties of the bulk materials are discussed in brief. The dependence of the carrier density on hydrostatic pressure has been investigated for several samples.

7.1 Bulk materials

When hydrostatic pressure is applied to a crystal, the lattice constant is expected to shrink, of course. Given the elastic constant of the material under pressure and the pressure that is technologically available, the amount by which the atoms move closer together is small: typically of the order of 0.1%. However, as the crystal lattice is responsible for the band-like dispersion of electrons in a semiconductor (or indeed, any) crystal, the parameters of the band structure change along with the lattice constant. The separation of bands being an effect of the periodicity of the underlying potential, it is clear that as the lattice constant is *decreased*, the band gaps should *increase*. Typically, for the available pressures in our setup the change in bandgap is of the order of 0.1 eV, i.e. it is appreciable.

In most III-V semiconductors, the indirect gap (from the valence band maximum at the Gamma point Γ^v to the X^c point minimum in the conduction band) has a negative, but smaller pressure coefficient.

Indium Arsenide

Indium Arsenide has a direct band gap of $E_g=0.40$ eV. The pressure dependence of E_g has been investigated by Zallen et al [Zallen67] in 1967, deploying optical techniques. They reported a value of 100 meV/GPa. This value is

similar to the pressure coefficients of other direct-gap semiconductors Shubnikov et al. studies magnetophonon absorption in InAs [Shubnikov76] under hydrostatic pressure. Their result is 115 ± 7 meV/GPa.

Aluminium Antimonide

The smallest gap between conduction band and valence band in AlSb is at the X point in k space, sized 1.696 eV. The direct gap, at the Γ point, is 2.32 eV large. There is contradictory information in the literature on pressure coefficients of the Γ^v to X^c point gap: [Laude70] reports $dE_g/dp = -35$ meV/GPa at 295 K while [Bhargava67] measured $dE_g/dp = -15$ meV/GPa at 2 K. The different temperature alone cannot explain the discrepancy. The more recent study by Strössner gives a possible explanation for this: it could have to do with the hygroscopicity of the material: “AlSb single crystals crumble within weeks when left in the open air”. The direct and indirect gap were measured carefully in a diamond anvil pressure cell at room temperature [Stroessner86]. The authors state value of 106 meV/GPa for the Γ^v to Γ^c gap.

Gallium Antimonide

GaSb is a direct semiconductor, the fundamental gap is 0.81 eV, the pressure coefficient of E_g is known to be $dE_g/dp = 145$ meV/GPa [Noack78].

7.2 InAs/AlSb Quantum Wells

Figure 7.1 shows ρ_{xx} traces from sample J at different pressures. The lowest trace is just a plain measurement of a Hall bar inside the pressure cell, but without pressure-transmitting liquid. The next trace up (0.03 GPa) is very similar but with carrier density just slightly higher than in the zero-pressure case. The pressure is still very low. With the pressure increasing further, the density is strongly reduced. An interesting observation is that the SdH amplitude does not decrease at the same time. The quantum scattering time even increases with decreasing N_s from 0.18 ps at zero pressure to 0.25 ps at $p=0.65$ GPa. At some high pressure, the quality of observable SdH oscillations is no longer good. The two topmost traces in Figure 7.1 show irregular ‘dropouts’, indicating a poor contact, and the SdH amplitude becomes small. These curves can still be evaluated in terms of the frequency, but absolute values of ρ_{xx} can not be taken seriously: the two-terminal resistance of the sample is high.

This is the typical behaviour of InAs/AlSb quantum wells: a change at zero pressure due to the applied pressure transmitting liquid, the decrease in density with increasing pressure, and finally the degradation of the sample quality in high pressures. This degradation could have various causes:

- the narrow voltage probes are depleted as the carrier density drops below a critical value
- the Ohmic contacts turn bad at high pressure, or due to mechanical strain in the pressure cell

Mostly, the good SdH oscillations are recovered as the pressure is decreased again, no permanent damage is done to the sample. In some cases, there *is* permanent damage, in the shape of a fine crack in the sample, rendering it unusable after the pressure is released.

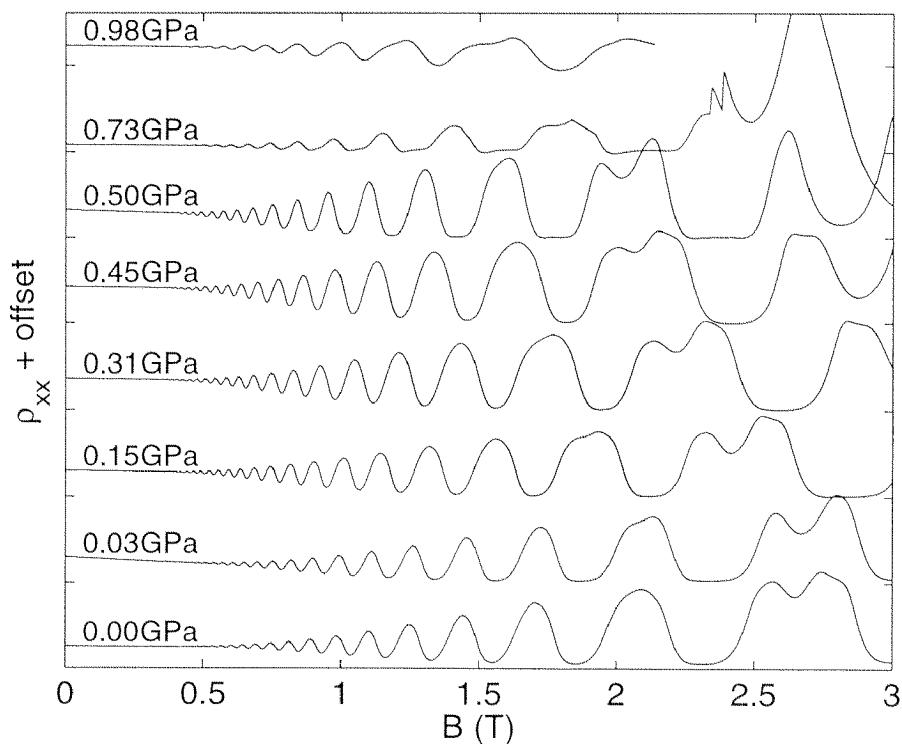


Figure 7.1: Magneto-transport at different pressures, Sample J. The bottom trace was measured without liquid in the pressure cell. Curves are offset in the vertical by $800\ \Omega$ each, the zero line for each curve is indicated by the tick marks.

The decrease in N_s as a function of pressure for sample J is given in Figure 7.2. Two measurements are presented, the crosses refer to the same data as Figure 7.1.

In sample N (with GaSb cap), very similar behaviour is observed up to 1 GPa. The highest pressure yields a *higher* carrier density again. This point has not been included in the fit for $\partial N_s/\partial p$. Again, the wet sample without pressure shows a substantially increased carrier density.

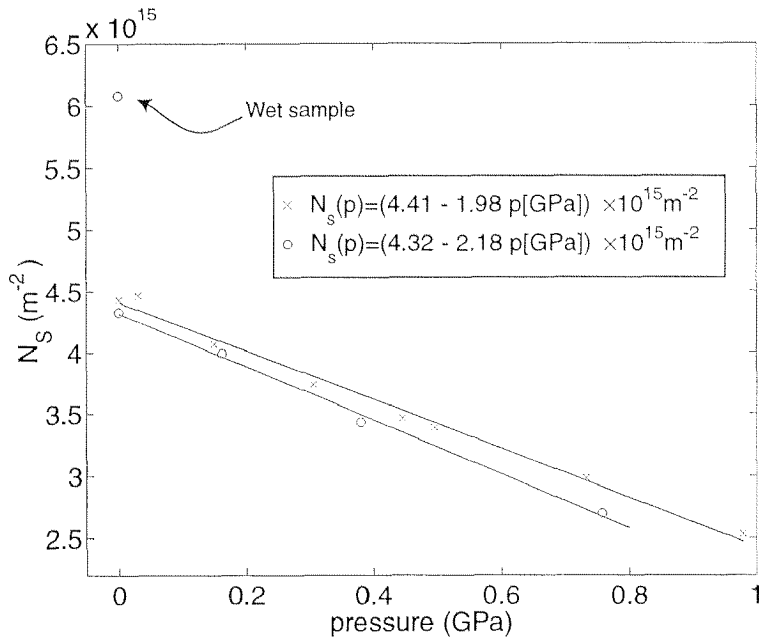


Figure 7.2: Decreasing N_s with pressure in Sample J. Crosses and circles refer to two independent measurements of different chips. Crosses correspond to the data given in Figure 7.1. The increase at \sim zero pressure is much stronger in the other measurement. Pressure coefficients of N_s are similar in both cases.

Sample R has a very thin cap layer (5 nm GaSb). As can be seen in Figure 7.4, there is no qualitative difference in $N_s(p)$. The quantum scattering time has been measured via the SdH amplitude, and shows no significant change with carrier density. The Drude scattering time is much reduced at the point where N_s goes below $12 \cdot 10^{15} \text{ m}^{-2}$. Above this density, more than one electric subband is populated in the well, and intersubband-scattering reduces the mobility.

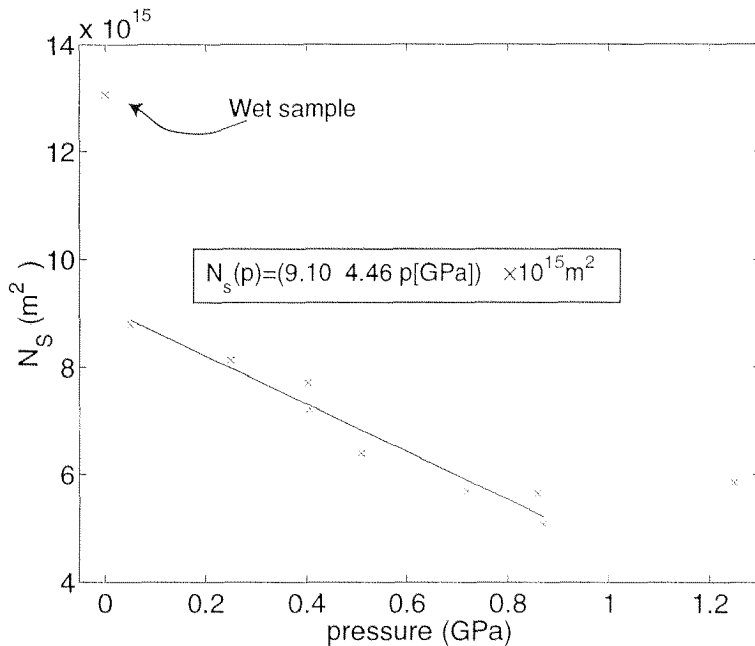


Figure 7.3: Pressure transport data from sample N. The highest pressure yields a *higher* carrier density that is not consistent with what was measured in other samples.

Figure 7.5 shows ρ_{xx} traces from sample E at ambient pressure and three different hydrostatic pressures applied in the experiment. Sample E is an InAs-capped quantum well similar to J but with lower mobility. Even filling factors

have been marked with dotted lines, $\nu = 4$ is marked in each plot. Evidently, the carrier density decreases with pressure. At the highest pressure that was measured, the Hall plateau at $\nu = 2$ is distorted towards lower ρ_{xy} values. This behaviour has been observed in many samples at low filling factors, with or without pressure (see, e.g., Figure 3.4). The carrier densities have been determined in the manner shown in Figure 7.5, just by finding the magnetic field for $\nu = 4$. Looking closely, however, the other minima do *not* fall onto the dotted lines, plotted $1/B$ -periodic as expected. (This is not due to an offset in B : all traces have been measured in both field directions, and $\rho_{xx}(\rho_{xy})$ traces were (anti-)symmetrized. The small experimental offset from hysteresis effects was subtracted.) This effect is rather drastic in the bottom row of Figure 7.5: the dotted line for $\nu = 2$ is clearly not in the centre of the $\nu = 2$ SdH minimum.

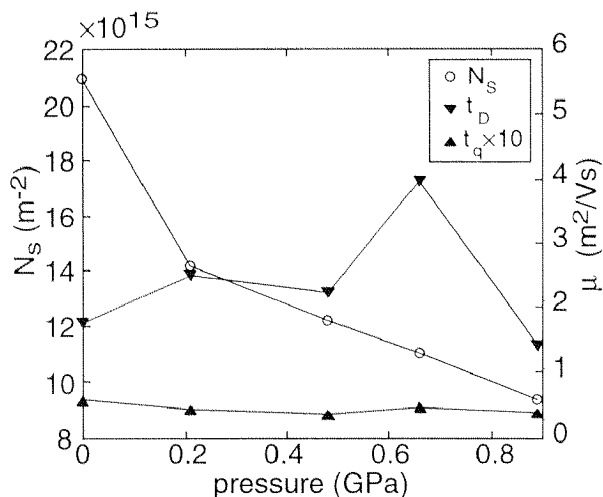


Figure 7.4: Sample R (with 5 nm GaSb cap). The initial density is very high due to the thin cap. Once inter-subband scattering is quenched below $N_s=12 \cdot 10^{15} \text{ m}^{-2}$, the Drude scattering time is increased.

In the top three measurements, the Hall density matches the density determined from the position of $\nu = 4$ quite well. In the lowest trace, this is not the case: ρ_{xy} is too small, only when ρ_{xy} is multiplied by a constant such that the $\nu = 4$ plateau is at the correct value, the Hall density comes out right. The $1/B$ periodicity of SdH oscillation is broken in this sample.

Table 7.1 summarizes the coefficients of density decrease from the measurements presented above. A general trend to be observed is that the thinner the cap, the more the carrier density decreases with pressure. Thin cap layers mean that most of the electrons come from surface states. This suggests that surface states are affected by the pressure change stronger than the deep AlSb donors and interface states on the InAs/AlSb boundary (see chapter 3.2.2. However, no clear relationship between cap thickness and $\partial N_s/\partial p$ can be established.

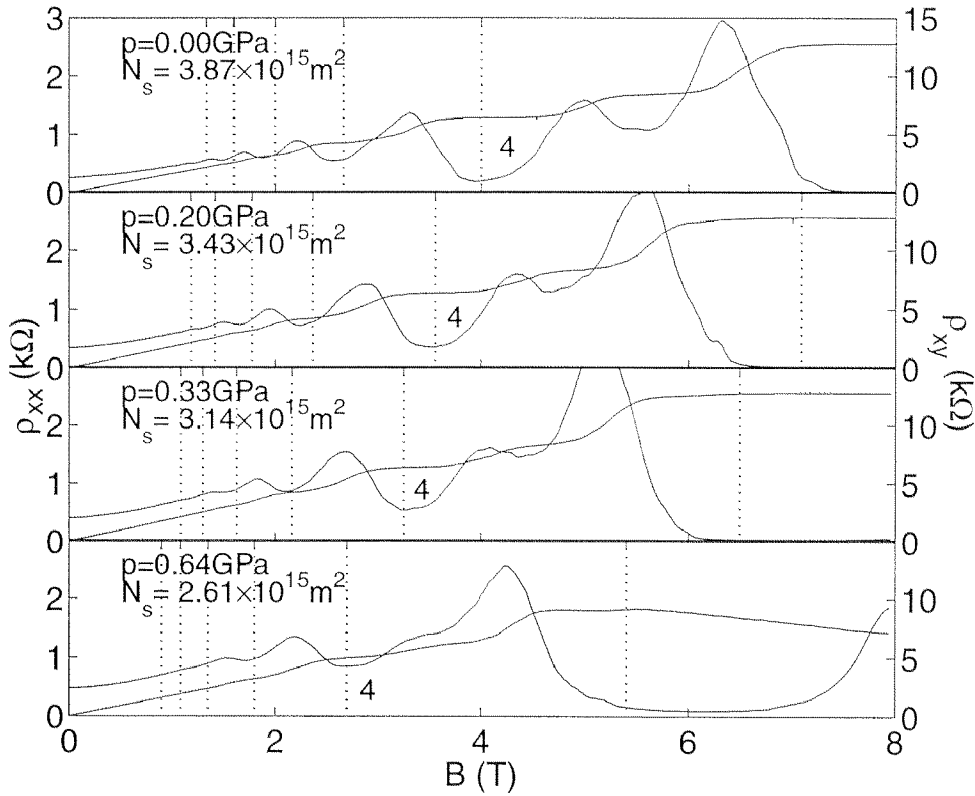


Figure 7.5: Magnetotransport data at different pressures. Sample E.

epilayer	cap nm	name	carr. dens. 10^{15} m^{-2}	$\partial N_s / \partial p$ $10^{15} \text{ m}^{-2} / \text{GPa}$	Figure
9701-09	5	R	21	-6.0	7.4
9602-24	56	N	9.1	-4.4	7.3, 6.3
9401-38	28	J	4.32	-2.0	7.2
9503-18	56	E	3.8	-2.0	7.5
9701-08	450	C	7.79	-0.98	
9211-10	50		7.3	-0.83	

Table 7.1: Samples and their pressure coefficients of N_s

7.3 Conclusion

Hydrostatic pressure experiments have proven to be difficult, for various reasons. Sample cannot be prepared in standard chip carriers and bonded because the available space is too small, samples with scratches on the back or at the edges are prone to cleave when pressure is applied, when the cell leaks under pressure, the whole content of the cell is often destroyed. This is especially disadvantageous where good QW material is scarce, as is the case with INAs/AlSb wells.

Furthermore, 2DEG samples often show slightly different properties in different cooldown cycles, and changing the pressure in a low temperature clamped pressure cell is only possible after warming up, thus no pressure-series can be measured in a single cooldown cycle (Even the expensive, complicated and hazardous technique with Helium as a pressure-transmitting medium demands warming up to liquid nitrogen temperature before the pressure can be changed). On the other hand, the high-pressure technique allows to change a very fundamental property of the material in question: the lattice constant. This is why pressure measurements have been necessary to identify band structure parameters of semiconductors. On InAs/AlSb quantum wells, hydrostatic pressure can be the only method to lower the carrier density. Experiments show that this carrier decrease does not always go along with a strong increase in the scattering rate: a very favourable circumstance for experiments. Decreasing the density by illumination seems to affect the scattering rate more, possibly because of inhomogeneities introduced in the sample.

Devising an experiment with a pressure cell under a tilted magnetic field would be very interesting because the spin-polarised filling factor 2 could be studied in sufficiently low fields. For that, either a small pressure cell has to be devised, that can be rotated inside the magnet bore, or the sample is mounted at an angle to begin with, so that the pressure cell only has to be tilted by a relatively small angle: a range of 20° would be sufficient. In this case, no zero-angle measurement could be made, which is inconvenient because the carrier density is most easily determined with B parallel to the sample normal.

Chapter 8

Negative Persistent Photoconductivity Effect

In some InAs/AlSb quantum well samples, the electron density is reduced on illuminating the sample in the cryostat. This is known as the negative persistent photoconductivity effect (NPPC). In InAs/Al_{0.6}Ga_{0.4}Sb quantum wells, this effect was first reported by [Tuttle89], additional experiments are presented in [Lo92]. In a more recent study [Wang96], InAs/AlSb quantum wells with a grown-in back gate electrode could be fabricated that allowed to ‘reset’ the effect of NPPC electrically: the trapped electrons can be redistributed by applying a small electric field. It is suggested that aluminium atoms in anti-mony sites can act as a deep donor or a deep acceptor, and that the transition between these two modes is responsible for the photoeffect.

8.1 Experiments with Illumination

Light emitting diodes (LED) are used to illuminate the sample in the cryostat. Not all LEDs are functional at low temperatures. Specifications for these devices usually state a minimum operating temperature of -40°C. Some types of LED still operate in liquid Helium when they are initially switched on at room temperature, but fail to ignite in the cold. It is believed that carriers freeze out and disallow low temperature operation. The new highly-doped GaN LEDs work well in lHe conditions. The ignition voltage for LEDs can be as high as 30 V or more. Therefore, LEDs were driven by a ‘flasher’ device that consists of a 100 V DC pulse source with a 10 kΩ series resistor to limit the current to 10 mA. Applying the voltage in reverse bias direction is fatal for the LED, because the depletion layer in highly-doped diodes is thin.

8.2 Sample Dependence

Illuminating the sample is an elegant and easy way to modify the carrier density, albeit not applicable to all samples.

The low-density InAs capped samples (J and N) show no trace of susceptibility to light. Neither does Sample L, a non-intentionally doped QW with $\sim 12.5 \cdot 10^{15} \text{ m}^{-2}$ electrons. Sample F can be tuned from $\sim 12.5 \cdot 10^{15} \text{ m}^{-2}$ to $\sim 8 \cdot 10^{15} \text{ m}^{-2}$. The thick-cap sample C allows a change in density by illumination from $8 \cdot 10^{15} \text{ m}^{-2}$ to $6.2 \cdot 10^{15} \text{ m}^{-2}$.

8.3 Inhomogeneous Illumination

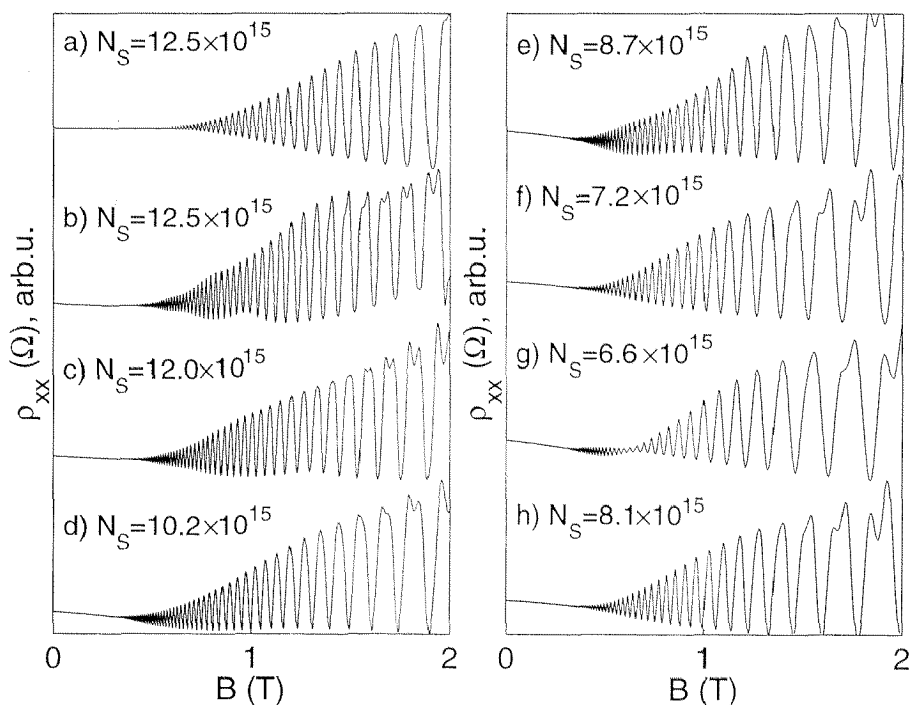


Figure 8.1: Magnetoconductance curves for various states of illumination. a) was taken after cooldown in the dark. The sample was exposed to a short flash before each curve and left to equilibrate for a few minutes. Traces b, c, e, and g show beating patterns. Before curve h was taken, the sample was illuminated a longer period and left alone for 6 hours.

In an attempt to vary the carrier density, sample F was illuminated with short light pulses and magnetoconductance traces were taken after a settling time of some minutes. The surprising result was that super-periods just like beating patterns appear in $\rho_{xx}(B)$ in some instances. Upon further illumination, these patterns go away and come back. Figure 8.1 shows ρ_{xx} traces that were taken in the order a)-h). After cooldown in the dark, the onset of SdH-oscillations is at higher field than in the other curves. The same holds for the onset of spin splitting, barely discernable in trace a) but clear in b)-h). This indicates that small-scale potential fluctuations, on the order of the magnetic length, level out under illumination, so that the quantum scattering time is increased. But, apparently, the large-scale potential fluctuations are increased, because

more than one period of oscillations appears, indicating areas with different electron density. A similar experiment has been shown in the context of expected beating patterns, in section 6.2.3. Figure 6.4 on page 74 shows the data. In that measurement, it was demonstrated that a small portion of the sample, with voltage probes separated by $200\ \mu\text{m}$, shows homogeneous SdH oscillations, while a larger part, 1 mm in size, shows a beating pattern.

8.4 Decay of NPPC, Temperature Dependence

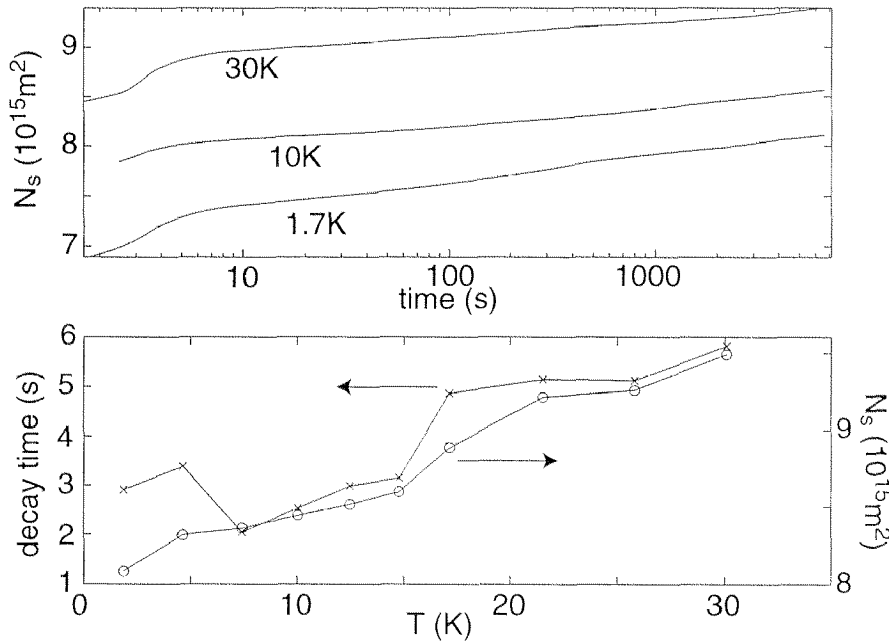


Figure 8.2: Electron density after flashing, sample F. The carrier density is decreased on illumination but creeps back towards a saturation value. Top: three curves of $N_s(t)$, at different temperatures. Bottom: fit results: ‘saturation’ carrier density and ‘decay time’ as a function of temperature.

Sample F has been exposed to light from an LED for 30 s, and after switching off the light, the Hall carrier density was monitored for one hour, by application of a small magnetic field. During the first few seconds after the illumination, the carrier density increases rapidly. After that, the density increase slows down. Plotted to a logarithmic time scale, this is displayed in the top half of Figure 8.2. No qualitative difference can be made out between the curves at 1.7 K and 30 K. The initial and final carrier densities increase with temperature. To quantify this, a simple model has been fitted to the data:

$$N_s(t) = N_{S,\infty} - N_{S,1}e^{-\frac{t}{\tau}} \quad (8.1)$$

In the bottom half of Figure 8.2, the resulting data for the saturation density $N_{S,\infty}$ and the time constant τ is plotted for various temperatures. Data in the time range between 1000 s and 6000 s has been used for the fit. It is evident that the saturation density (circles in the figure) increases with temperature. This

can be understood qualitatively, because the ‘natural’ carrier density is higher than these values, and the NPPC is a low-temperature effect. The ‘hotter’ the sample gets, the closer does the density creep towards its original value. The proposed ‘decay time’ τ in equation (8.1) increases with temperature, too. This result is more surprising: If, say, temperature-activated tunneling out of some acceptor state was responsible for the change in carrier density, the opposite temperature dependence of τ would be expected. Anyway, the model does not really fit the data over a long time range. All curves show a weak, but peculiar reduction in slope at around 10^3 s (to be seen most clearly in the 1.7 K trace in Figure 8.2) . Most likely, a multitude of different and competing slow transport processes are responsible for this long time-range behaviour.

Whether after a very long period of time the density would arrive at a constant density, and whether this density is temperature-dependent, cannot be judged from the data: very long waiting periods would be necessary to investigate this. However, after several hours at low temperature, the density is stable enough to assume it as constant. The useable range of densities accessible through the NPPC is limited by the decay effect.

Appendix A

Gating InAs/AlSb Samples

One of the drawbacks of the InAs/AlSb material system is the difficulty of applying good metal frontgates, i.e. metal films that can be biased with a potential so as to influence the carrier density in the sample. Some successes with gates have been demonstrated, but the absence of *good* gates probably impose the greatest difficulty in the application of the InAs/AlSb system.

In the first 2DEG samples, which were silicon MOSFETS (metal oxide semiconductor field effect transistor), the gate was the whole point of the operation: by controlling the number of carriers in the channel, the desired ‘gating’ effect is achieved. For the purpose of insulation, a silicon oxide layer is formed on the surface of the silicon. With silicon, a very homogeneous and highly oxide forms more or less by itself, while exposed to oxygen or water vapour at high temperature. This, by the way, is one of the reasons why the history of silicon as a material is such a success story.

On AlGaAs/GaAs quantum wells, a metal gate can be applied directly to the cap layer of the semiconductor: the Schottky barrier between the metal and the GaAs is sufficient to allow for useful gate voltages. Typically, in a range of -1 V to 0.6 V the gate is current-free. The commercially available HEMTs (high electron mobility transistor) out of GaAs work in the same fashion, they are used for high-speed applications (or at low temperatures, where in conventional semiconductor devices all electrons freeze out).

A.1 Silicon Oxide-Insulated Gates

Metal films on InAs/AlSb structures do not exhibit the Schottky barrier. An insulating film has to be introduced in order to produce working gates. We have tried to use a vacuum-deposited SiO_2 film of 20 nm in between the cap and the metal gate. The resulting IV-curve of the gate leakage current vs. the applied voltage is shown in Figure A.1. In a range of $\pm 600\text{ mV}$, the leakage

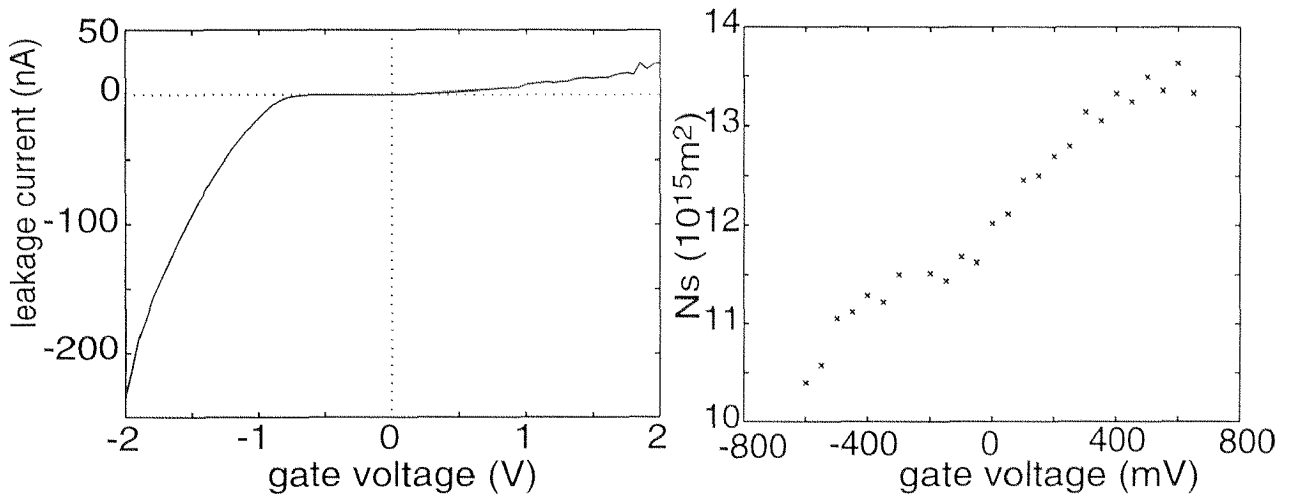


Figure A.1: Left: Gate IV curve. Right: Gate voltage vs. carrier density for a SiO_2 -insulated top gate on sample J. The change of carrier density is small. Also, the carrier density of the sample is much higher than that of the ungated sample.

current is small, so that this range has been used to investigate $N_s(V_{\text{gate}})$. The right side of Figure A.1 has the somewhat disappointing result: the available range of densities spans a factor of 1.3 only. What is more, the total density is very high to begin with. InAs/AlSb QWs naturally have a high carrier density, and the interest of the experimentalist is to bring the density down, in order to reach low filling factors at moderate magnetic fields. Clearly, the gated device presented here does not lead into this direction. Apparently, the silicon oxide changes the InAs surface in a way that it does not capture electrons as it normally does (see section 3.2.2).

Subsequent points in Figure A.1 alternate in N_s by up to $0.5 \cdot 10^{15} \text{ m}^{-2}$. This is because the density was determined from the SdH period, and the B -sweeps were taken in alternating directions. The density changes as a function of time after a gate voltage has been set. The ‘history’ of gate voltages also plays a role, as can be seen in Figure A.2. The time-dependence of the density was measured by applying a magnetic field 0.5 T and recording ρ_{xy} , while changing the gate voltage in steps of $\pm 0.5 \text{ V}$. An exponential law can be used to describe $N_s(t)$ after a change of V_g , with a time constant of $\tau \sim 30 \text{ s}$, with the exception of the voltages $V_g \leq -1 \text{ V}$. The considerable gate currents that flow here cause the ρ_{xy} signal to be more unstable, and for some reason is the relaxation N_s bigger for $V_g = -1 \text{ V}$ larger than the one for $V_g = -0.5 \text{ V}$. The time constant is $\tau = 60 \text{ s}$ in this case.

To sum up, the experiment with a SiO_2 -insulated gate shows that ‘slow transport processes’ already mentioned in the connection with NPPC also render the use of this density-changing device limited. High speed response of

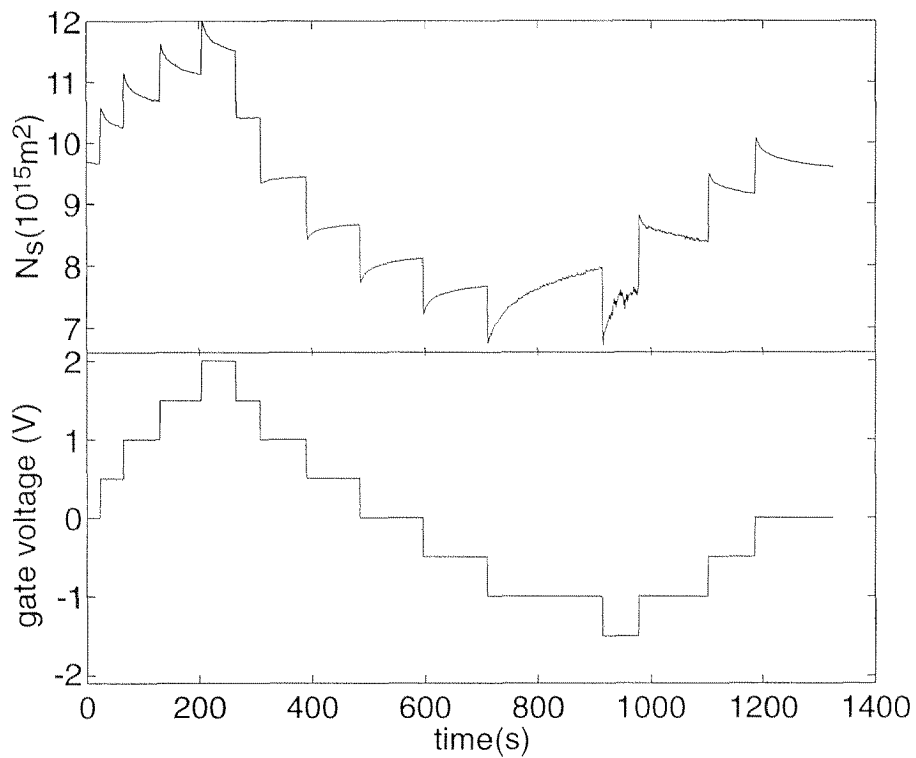


Figure A.2: Time dependent density change as a function of gate voltage. After each step in V_g , the carrier density always tends back to the previous value exponentially.

the gate has not been investigated, but possibly these drawbacks would not influence the performance in the same way.

Appendix B

Samples

This section summarises information about the samples used throughout this thesis. It compiles the growth reports from Santa Barbara as well as transport data gathered in this work. The UCSB reference numbers identify the samples. The first four digits give the growth date (YYMM), the rest is a running counter. Thus, 9211-52 is the 52nd sample grown in November 1992. To make them easier to memorize, I have given the different wafers proper names, and short numbers or letters as identifiers for the individual samle chips, i.e. hallbars etc. I refer to wafers in the text with their (unique) initial letter.

The information about the sample growth does not always give details about the nucleation layers, but the structure beneath the bottom barrier is always similar and is not assumed to play a decicive role for the experiments presented here.

Bulak

UCSB reference: 9103-17

AlAs/InAs QW with one-sided Te bulk doping

The only sample in which two electric subbands are occupied

N_s : $3.8 \cdot 10^{16} \text{ m}^{-2}$

Layers:

GaSb 10 nm

AlSb 85 nm

Te-doped $N_d = 6 \cdot 10^{16} \text{ m}^{-2}$

AlSb Barrier 15 nm

InAs Well 15 nm

AlSb Barrier 15 nm

...

Carl

UCSB reference: 9701-08

high- μ AlAs/InAs QW with extra-thick top barrier.

GaSb is used for most of the top barrier material, because

AlSb does not grow well in thick layers

Layers:

GaSb 400 nm

AlSb Barrier 50 nm

InAs Well 15 nm

AlSb Barrier 50 nm

GaSb Buffer 1.1 μm

AlSb nucleation 80 nm

Ernesto

UCSB reference: 9409-20

N_s : $4.4 \cdot 10^{15} \text{ m}^{-2}$

low- N_s AlAs/InAs QW, InAs cap

The exact layers sequence is not documented,

but is similar to sample J.

Frank

UCSB reference: 9211-52

high- μ AlAs/InAs QW with one-sided Te δ doping

N_s : $12.5 \cdot 10^{15} \text{ m}^{-2}$

μ_D : $80 \text{ m}^2/\text{Vs}$

Layers:

GaSb 15 nm

GaSb+AlSb SL 20 periods (2.5+5)nm (150 nm)

δ -Te-Sheet

AlSb Barrier 50 nm

InAs Well 15 nm

AlSb Barrier 20 nm

AlSb+GaSb smoothing SL 10 periods (2.5+2.5) nm

GaSb Buffer $2 \mu\text{m}$

AlSb nucleation 100 nm

Jimi

UCSB reference: 9401-38

low- N_s AlAs/InAs QW, InAs cap

N_s : $4.4 \cdot 10^{15} \text{ m}^{-2}$

Layers:

InAs 3 nm

GaSb 5 nm

$\text{Al}_{0.8}\text{Ga}_{0.2}\text{Sb}$ 20 nm

InAs Well 15 nm

AlSb 2.5 nm

...

Linus

UCSB reference: 9503-18

AlAs/InAs QW, GaSb cap

N_s : $6.2 \cdot 10^{15} \text{ m}^{-2}$

Layers

GaSb Cap 5 nm

$\text{Al}_{0.8}\text{Ga}_{0.2}\text{Sb}$ 21 nm ('digital' alloy)

AlSb 2.5 nm

InAs Well 15 nm (In-Sb both interfaces)

AlSb+GaSb SL $20 \times (2.5 + 1.5) \text{ nm}$ (AlSb nearest QW)

GaSb Buffer $2 \mu\text{m}$

Nadja

UCSB reference: 9602-24

N_s : $9 \cdot 10^{15} \text{ m}^{-2}$

μ_D : $80 \text{ m}^2/\text{Vs}$

Layers:

GaSb 28 nm

GaSb+AlSb SL 2 periods (7+7)nm (28 nm)

InAs Well 15 nm (InSb-like interfaces)

AlSb+GaSb SL 20 periods (7+7) nm (280 nm)

GaSb Buffer $2 \mu\text{m}$

...

Rodjin

UCSB reference: 9701-09

AlAs/InAs QW with thin GaSb top barrier

this was grown with AFM lithography applications in mind.

the mobility isn't so hot but for a QW practically at the surface.

N_s : $2.2 \cdot 10^{16} \text{ m}^{-2}$

μ_D : $1.5 \text{ m}^2/\text{Vs}$

Layers:

GaSb 5 nm

InAs Well 15 nm

AlSb Barrier 50 nm

GaSb Buffer $1.1 \mu\text{m}$

AlSb nucleation 80 nm

Appendix C

The making and use of a clamped pressure cell

This chapter explains the making use of the clamped pressure cell as used in this work. It is intended as a guide to anyone who wants to try using this technology himself (or herself), even though it does not claim to be complete. It just compiles what information seems useful and necessary to me for reproducing this technology.

C.1 Making Pressure Sensors

C.1.1 Manganin Gauge

Manganin gauges are made by simply winding a little coil of enough wire to give a resistance of about $100\ \Omega$, and fix two wires on either end to allow 4-terminal resistance measurement. The manganin wire has to be artificially aged by subjecting it to many pressure cycles and cooldown cycles, until the wire's $R(T, p)$ does not change any more.

C.1.2 InSb Gauge

The material that has been used is highly Te-doped bulk InSb, which is a brittle material. To fabricate a pressure sensor, a tiny rod has to be cut, about $4 \times 0.5 \times 0.5\ \text{mm}^3$ in size. This can be done by cleaving or employing a wire saw. Four indium droplets are fixed with a soldering iron, and gold bond wires are applied to allow four-terminal measurement. In order to obtain a useable device, a small piece of epoxy print board is made with four $100\ \mu\text{m}$ copper wires attached, and the InSb crystal is connected. Soldering the gold wire to the solder points has to be done with care, because with a hot soldering iron the gold will dissolve in the solder before it is connected properly. To protect

the device it is useful to place a short piece of Teflon tube around the whole arrangement. These sensors have proven to be reliable and can be used many times if handled with some care. The two-terminal resistance of the contacts is a few Ohms, the four-terminal resistance is $10\text{ m}\Omega - 50\text{ m}\Omega$, at ambient pressure. The pressure readout at room temperature and at low temperatures is treated in section 4.5.2.

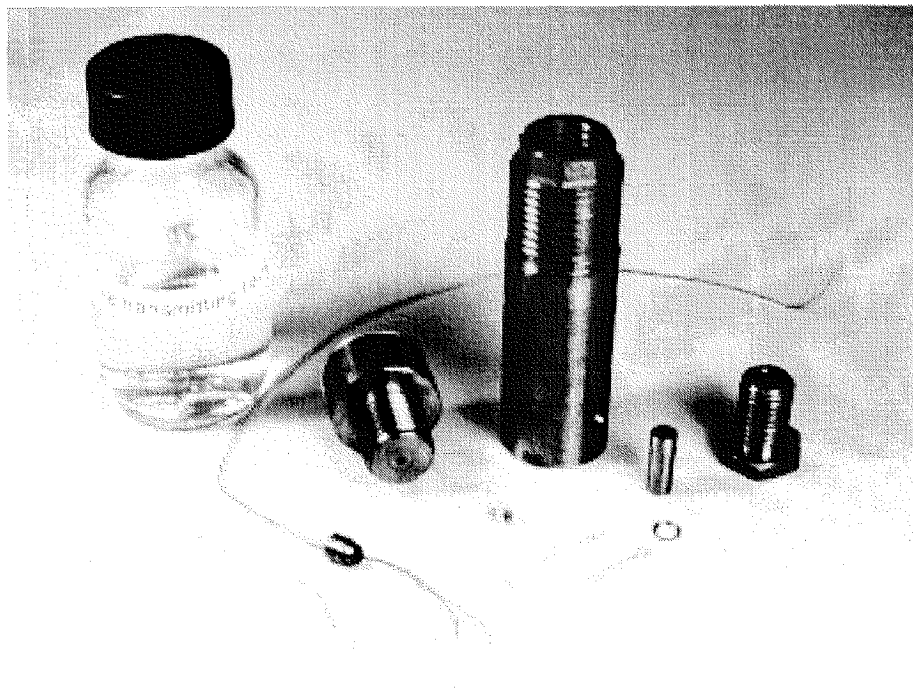


Figure C.1: A still life: parts of the pressure cell

C.2 Parts

Most of the parts of the pressure cell are made out of beryllium-copper. This material comes from the manufacturer in a 'soft' state in which it is machined easily. After the parts have been made, they undergo a tempering process at 350°C , to give them the final strength. Only the seal ring (3) is left in the soft state. The cell main cylinder is turned with a slightly smaller inner diameter. After hardening, it is stopped up with the bottom screw, then filled with a block of lead and pressurized with a hard metal stamp, until the soft metal comes oozing out of the $2\text{ mm}\phi$ hole at the bottom. After this, the bore is opened up to the final $6\text{ mm}\phi$. This 'pre-straining' reduces the creep of the material when the cell is set under pressure later. Table C.1 lists the parts used in the assembly, Figure C.3 shows a technical drawing of the device. A simpler representation is given in Figure 4.6 on page 41 .

No.	Part	material
1	Cylinder	beryllium-copper
2	plug & wire feedthrough	beryllium-copper, Stycast
3	seal ring	beryllium-copper(soft)
4	anvil	beryllium-copper
5	bottom screw	beryllium-copper
6	Teflon capsule	Teflon
7	top ring	beryllium-copper
8	pressure rod	G30
9	pill	G30
10	fixage screw	beryllium-copper
11	pressurizing liquid	n-pentane:3-Methyl 1-Butanol (1:1)

Table C.1: Parts of the pressure cell

C.3 Making Wire Feedthroughs

The small plug with up to 16 wires leading into the pressure chamber has to be prepared with great care since it is the ‘weakest point’ in the pressure cell, and prone to burst, leaving sample and pressure sensor in crumbles.

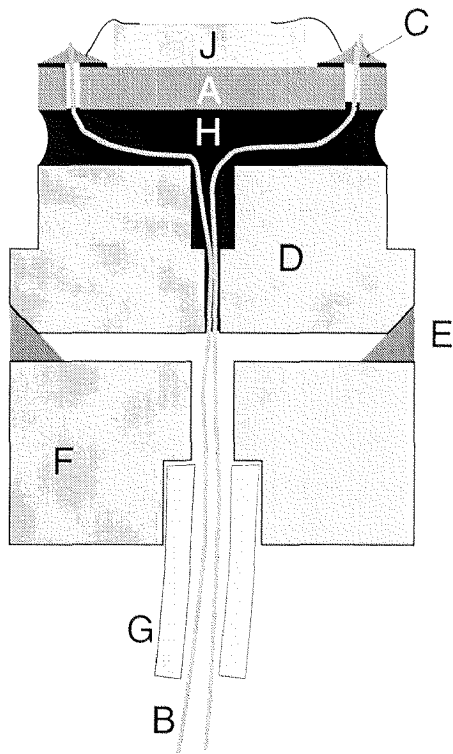


Figure C.2: Parts of the wire feedthrough: A epoxy disc, B wires, C solder, D plug (berylco), E seal ring (soft berylco), F anvil (berylco), G teflon tube, H stycast resin, J sample.

I start off with a 4.2 mm ϕ copper-plated epoxy disc with 12 contact seg-

ments around the edge, and 0.3 mm holes bored in each segment. A square area of about $3 \times 3 \text{ mm}^2$ is left for installing the sample later. A $70 \mu\text{m}$ varnished copper wire about 25 cm long are threaded through each hole and soldered in place. For use with the pressure sensor, it is useful to insert 4 extra wires that stick out about a cm. It is a good idea to make the length of the wires about 1 cm longer from each one to the next, so that later the numbers can be identified easily. All the wires are threaded through plug (part 2), seal ring and the anvil (parts 3 & 4), and pushed into into a 22 cm piece of Teflon tube, outer diameter 1.1 mm.

Stycast 2048FT resin is warmed up to $\sim 60^\circ\text{C}$ and stirred well before use, pumped for several hours to get rid of air trapped in bubbles, and thoroughly mixed with hardener No.11 (5%). After cleaning the wires and the plug in acetone in an ultrasonic bath, a droplet of Stycast resin is applied in between the epoxy disc and the plug, making sure that

- no air bubbles get trapped
- all wires are nicely coated in the resin
- the epoxy disc is fixed in level position
- the wire bundle that comes out the other end is not coated with stycast, for it will be inflexible then and break.

The whole is baked at 150°C for 1 h, after which the Stycast is set and very hard. The teflon tube is threaded through the seal ring (3), anvil (4) and bottom screw (5). All the wires are connected up to a DIL16 connector.

C.4 Assembly

The sample chip is connected to the little contact segments on the epoxy disk, employing gold bond wires and Indium as solder. It is not a good idea to glue the sample in place, for if there are bubbles of air trapped underneath, the chip will crumble to oblivion if hydrostatic pressure is applied. The chip is best held in place by the wires only, during measurement it is immobilized by the frozen pressure transmitting liquid.

Then, the pressure gauge is connected by its four wires, and they are bent so that the Teflon capsule will fit over the whole assembly, and about $1/2$ of the whole space is still free, to allow for the piston to come down.

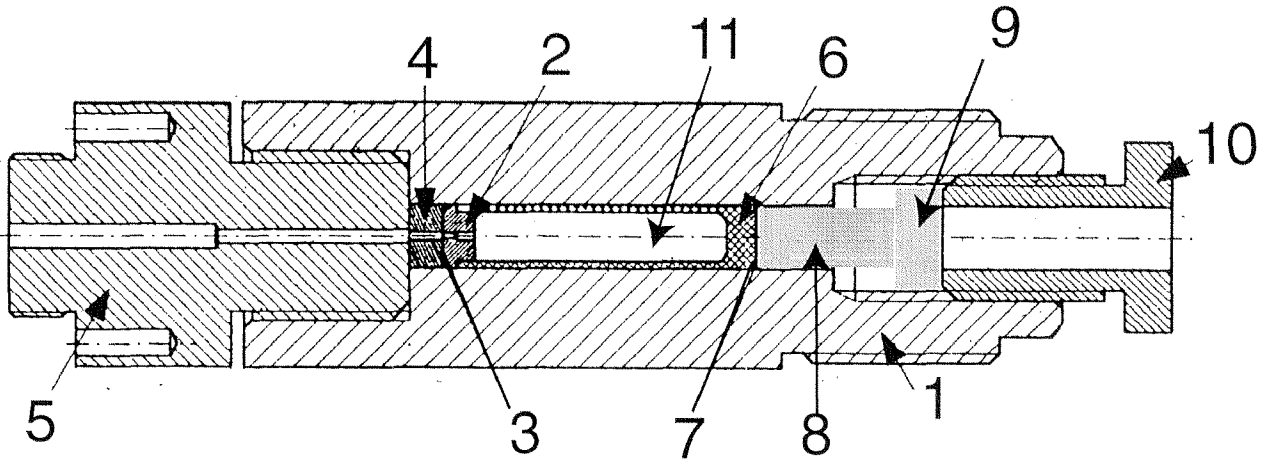


Figure C.3: Drawing of the pressure cell assembly

It is wise to do a measurement of the whole arrangement without any pressurizing liquid first, to check the sample connectors, and to determine the sensor's $R(p = 0)$ at low temperature.

C.5 Pressurizing

After the 'trial run' has succeeded, we can fill the teflon capsule with pressurizing liquid and carefully insert the plug, sample and sensor assembly. The capsule is inserted into the cylinder, nudged in so that the bottom of the anvil is level with the edge of the inner bore, and insert the bottom screw. On the other end, the top ring (7) and pressure rod (8) go in, then the plug, fixed by the top screw. We keep the pressure gauge readout connected during all this, so that we will notice immediately if something goes wrong with it. It is not a good idea to tighten the top screw just now, because the sealing of the teflon capsule is not effective at low pressure. A brass shield is fitted to the bottom end so as to protect the wire bundle, and prevent damage in the case that the feedthrough will burst.

C.6 Cooldown and Warmup

The whole assembly is now ready to be inserted in a cryostat to perform the measurements. It is important to cool the cell slowly, otherwise the pressure will have strong uniaxial components. It is believed that cooling down to Helium temperature in about two hours is a sensible rate.

After the measurement, the pressure cell is taken out of the cryostat and

warmed up at room temperature. This has proven to be the critical moment where the wire feedthrough is likely to burst. If it does burst, the mechanical energy that is stored in the compressed liquid is released and the whole content of the cell can be destroyed. The enenergy is about one Joule, which is enough to slightly deform the brass shield. If habdled with the appropriate care, immediate danger of injuries can be avoided when handling pressure cells.

Appendix D

Glossary

Acronyms

aka also known as

e.g. exempli gratia (\equiv for example)

i.e. id est (\equiv it is, in other words)

LED Light Emitting Diode

MBE Molecular Beam Epitaxy

NPPC Negative Persistent Photoconductivity Effect

QW Quantum Well

SdH Shubnikov-de Haas

Symbols

B Magnetic Field

\mathbf{E} Electric Field

E_F Fermi energy

\mathbf{k} wave vector

k magnitude of wave vector

k_F Fermi Wave Vector

μ Mobility

μ_B Bohr's Magnetron

- N_s Electron density per unit area
- ν Filling Factor
- ω_c Cyclotron Frequency
- p Hydrostatic pressure
- ρ_{xx} Longitudinal Resistivity, parallel to current
- ρ_{xy} Transversal Resistivity, perpendicular to current
- σ Conductivity
- τ_D Drude (aka Transport) Scattering Time
- τ_Q Quantum (aka Single Particle) Scattering Time
- z the space coordinate in growth direction,
i.e. perpendicular to the electron plane

Bibliography

- [Ando79] T. Ando. Theory of intersubband cyclotron combined resonances in the silicon space-charge layer. *Phys. Rev. B*, **19**, 2106 (1979).
- [Ando82] T. Ando, A. B. Fowler, and F. Stern. Electronic properties of two-dimensional systems. *Rev. of Mod. Phys.*, **54**, 437 (1982).
- [Ando74b] T. Ando and Y. Uemura. Theory of oscillatory g factor in a mos inversion layer under strong magnetic fields. *J. Phys. Soc. Jap.*, **37**, 1044 (1974).
- [Ando74a] T. Ando and Y. Uemura. Theory of quantum transport in a two-dimensional electron system under magnetic fields. i. characteristics of level broadening and transport under strong fields. *J. Phys. Soc. Jap.*, **36**, 959 (1974).
- [Arahanov59] Y. Arahonov and D. Bohm. Significance of electromagnetic potentials in the quantum theory. *Phys. Rev.*, **115**, 485 (1959).
- [Ashcroft76] N. W. Ashcroft and N. D. Mermin. *Solid State Physics*. HRW International (1976).
- [Beerens87] J. Beerens, G. Grégoris, S. B. Amor, J. C. Portal, E. E. Mendez, L. L. Chang, and L. Esaki. GaSb-InAs-GaSb Heterostructures studied under hydrostatic pressure. *Phys. Rev. B*, **36**, 4742 (1987).
- [Berry84] M. V. Berry. Quantal phase factors accompanying adiabatic changes. In *Proc. R. Soc. London, Series A*, volume 392, 45 (1984).
- [Bhargava67] Bhargava and Nathan. Stress dependence of photoluminescence in GaAs. *Phys. Rev.*, **161**, 1436 (1967).
- [Blank96] H.-R. Blank, M. Thomas, K. C. Wong, and H. Kroemer. Influence of the buffer layers on the morphology and the transport properties in InAs/(Al,Ga)Sb quantum wells grown by molecular beam epitaxy. *Appl. Phys. Lett.*, **69**, 2080 (1996).
- [Brosig99] S. Brosig, K. Ensslin, R. J. Warburton, C. Nguyen, and B. Brar. Zero-field spin splitting in InAs-AlSb quantum wells revisited. *Phys. Rev. B*, **60**, 13989 (1999).
- [Chang82] C.-A. Chang, H. Takaota, L. L. Chang, and L. Esaki. Molecular beam epitaxy of AlSb. *Appl. Phys. Lett.*, **40**, 983 (1982).

- [Cho71] A. Y. Cho. Growth of periodic structures by the molecular-beam method. *Appl. Phys. Lett.*, **19**, 467 (1971).
- [Claessen86] L. M. Claessen, J. C. Maan, M. Altarelli, and P. Wyder. Pressure dependence of band offsets in an InAs-GaSb superlattice. *Appl. Phys. Lett.*, **57**, 2556 (1986).
- [Conczykowski78] M. Cończykowski, M. Baj, E. Szafarkiewicz, L. Kończewicz, and S. Porowski. Narrow gap semiconductors as low temperature pressure gauges. In C. W. Chu and J. A. Woollam, editors, *High Pressure and Low Temperature Physics*. Plenum Press, New York and London (1978).
- [Das90] B. Das, D. C. Miller, S. Datta, and R. Reifenberger. Zero-field spin splitting in a two-dimensional electron gas. *Phys. Rev. B*, **41**, 8278 (1990).
- [Das89] B. Das, D. C. Miller, S. Datta, R. Reifenberger, W. Hong, P. Battacharya, and J. S. M. Jaffe. Evidence for spin splitting in $\text{In}_x\text{Ga}_{1-x}\text{As}/\text{In}_{0.52}\text{Al}_{0.48}\text{As}$ heterostructures as $B \rightarrow 0$. *Phys. Rev. B*, **39**, 1411 (1989).
- [Datta90] S. Datta and B. Das. Electronic analog of the electrooptic modulator. *Appl. Phys. Lett.*, **56**, 665 (1990).
- [eSilva94] E. A. de Andrada e Silva, G. C. L. Rocca, and F. Bassani. Spin-split subbands and magneto-oscillations in III-V asymmetric heterostructures. *Phys. Rev. B*, **50**, 8523 (1994).
- [Engels97] G. Engels, J. Lange, T. Schäpers, and H. Lüth. Experimental and theoretical approach to spin splitting in modulation-doped $\text{In}_x\text{Ga}_{1-x}\text{As}/\text{InP}$ quantum wells. *Phys. Rev. B*, **55**, R1958 (1997).
- [Fang68] F. F. Fang and P. J. Stiles. Effects of a tilted magnetic field on a two-dimensional electron gas. *Phys. Rev.*, **174**, 823 (1968).
- [Fowler66] A. B. Fowler, F. F. Fang, W. E. Howard, and P. J. Stiles. Magneto-oscillatory conductance in silicon surfaces. *Phys. Rev. Lett.*, **16**, 901 (1966).
- [Gardelis99] S. Gardelis, C. G. Smith, C. H. W. Barnes, E. Linfield, and D. Ritchie. Spin-valve effects in a semiconductor field-effect transistor: A spintronic device. *Phys. Rev. B*, **60**, 7764 (1999).
- [Gerhards76] R. Gerhards. Cumulant approach to the two-dimensional magneto-conductivity problem. *Surf. Sci.*, **58**, 227 (1976).
- [Giuliani85] G. F. Giuliani and J. J. Quinn. Spin-polarization instability in a tilted magnetic field of a two-dimensional electron gas with filled Landau levels. *Phys. Rev. B*, **31**, 6228 (1985).
- [Gobsch88] G. Gobsch, D. Schulze, and G. Paasch. Interpretation of Shubnikov-de Haas oscillations and the quantum Hall effect in a heterojunction with two populated subbands. *Phys. Rev. B*, **38**, 10943 (1988).
- [Guenther58] K. G. Günther. Aufdampfschichten aus Halbleitern der III-V Verbindungen. *Z. Naturforschung*, **13a**, 1081 (1958).

- [Heida] J. P. Heida, B. J. van Wees, J. J. Kuipers, and T. Klapwijk. Spin-orbit interaction in a 2 DEG in a InAs/GaSb quantum well with gate-controlled electron density. *Phys. Rev. B*, **57**, 11911 (1998).
- [Hopkins91] P. F. Hopkins, A. J. Rimberg, R. M. Westervelt, G. Tuttle, and H. Kroemer. Quantum hall effect in InAs/AlSb quantum wells. *Appl. Phys. Lett.*, **58**, 1428 (1991).
- [Kane57] E. O. Kane. Band structure of indium antimonide. *J. Phys. Chem. Sol.*, **1**, 249 (1957).
- [Kawaji94] S. Kawaji. Quantum transport in semiconductor surface and interface channels. *Surf. Sci.*, **299**, 563 (1994).
- [Koch93] S. Koch, R. J. Haug, and K. von Klitzing. Suppression of the Landau-level coincidence: A phase transition in tilted magnetic fields. *Phys. Rev. B*, **47**, 4048 (1993).
- [Kroemer92] H. Kroemer, C. Nguyen, and B. Brar. Are there Tamm-state donors at the InAs-AlSb quantum well interface? *J. Vac. Sci. & Tech.*, **10**, 1769 (1992).
- [Laihkthman94] B. Laikthman and E. A. Altshuhler. Quasiclassical theory of Shubnikov-de Haas effect in 2D electron gas. *Annals of Physics*, **232**, 332 (1994).
- [Lakhani73] A. A. Lakhani and P. J. Stiles. Experimental study of oscillatory values of g^* of a two-dimensional electron gas. *Phys. Rev. Lett.*, **31**, 25 (1973).
- [Laude70] L. D. Laude, M. Cardona, and F. P. Pollak. Deformation potentials of the indirect and direct absorption edges of AlSb. *Phys. Rev. B*, **1**, 1436 (1970).
- [Leadley98] D. R. Leadley, R. J. Nicholas, J. J. Harris, and C. Foxton. Critical collapse of the exchange-enhanced spin splitting in two-dimensional systems. *Phys. Rev. B*, **58**, 13036 (1998).
- [Lo92] I. Lo, W. C. Mitchel, M. O. Manasreh, C. E. Stutz, and K. R. Evans. Negative persistent photoconductivity in $\text{Al}_{0.6}\text{Ga}_{0.4}\text{Sb}/\text{InAs}$ quantum wells. *Appl. Phys. Lett.*, **60**, 751 (1992).
- [Lommer88] G. Lommer, F. Malcher, and U. Rössler. Spin splitting in semiconductor heterostructures for $B \rightarrow 0$. *Phys. Rev. Lett.*, **60**, 728 (1988).
- [Luo90] J. Luo, H. Munekata, F. F. Fang, and P. J. Stiles. Effects of inversion asymmetry on electron energy band structures in GaSb/InAs/GaSb quantum wells. *Phys. Rev. B*, **41**, 7685 (1990).
- [Luo88] J. Luo, H. Munekata, F. F. Fang, and P. J. Stiles. Observation of the zero-field spin splitting of the ground electron subband in GaSb-InAs-GaSb quantum wells. *Phys. Rev. B*, **38**, 10142 (1988).
- [Maan84] J. C. Maan. Combined electric and magnetic field effects in semiconductor heterostructures. In G. Bauer, F. Kuchlar, and H. Heinrich, editors, *2D Systems, Heterostructures and Superlattices*, volume 53 of *Springer Series in Solid State Sciences*, 183. Springer (1984).

- [LB-tables] O. Madelung, editor. *Intrinsic Properties of Group IV elements and III-V, II-VI and I-VII Compounds*, volume 17a and 22a of *Landolt-Börnstein New Series III*. Springer, New York (1992).
- [Morpurgo98] A. F. Morpurgo, J. P. Heida, T. M. Klapwijk, B. J. van Wees, and G. Borghs. Ensemble-average spectrum of Aharonov-Bohm conductance oscillations: evidence for spin-orbit induced Berry's phase. *Phys. Rev. Lett.*, **80**, 1050 (1998).
- [Nakagawa89] A. Nakagawa, H. Kroemer, and J. H. English. Electrical properties and band offsets of InAs/AlSb $n - N$ -isotype heterojunctions grown on GaAs. *Appl. Phys. Lett.*, **54**, 1893 (1989).
- [Nguyen93] C. Nguyen, B. Barr, and H. Kroemer. Surface-layer modulation of electron concentration in InAs-AlSb quantum wells. *J. Vac. Sci. & Tech.*, **11**, 1706 (1993).
- [Nicholas88] R. J. Nicholas, R. J. Haug, K. von Klitzing, and G. Weimann. Exchange enhancement of the spin splitting in a GaAs-Ga_xAl_{1-x} heterojunction. *Phys. Rev. B*, **37**, 1294 (1988).
- [Noack78] Noack and Holzapfel. Photoluminescence of GaSb under hydrostatic pressure. *Sol. St. Comm.*, **28**, 177 (1978).
- [Oelting88] S. Oelting, A. D. Wieck, E. Batke, and U. Merkt. Cyclotron masses of inversion electrons in tilted magnetic fields. *Surf. Sci.*, **196**, 273 (1988).
- [Rahman98] F. Rahman, B. L. Gallagher, M. Beth, and J. D. Boeck. Gating of InAs/GaSb quantum wells using a silicon monoxide gate. *Appl. Phys. Lett.*, **72**, 88 (1998).
- [Ren97] S.-F. Ren and J. Shen. *Ab initio* pseudopotential calculation of InAs/AlSb heterostructures. *J. Appl. Phys.*, **81**, 1169 (1997).
- [Schulz96] M. Schulz, F. Heinrichs, U. Merkt, T. Colin, and S. Løvold. Rashba spin splitting in a gated HgTe quantum well. *Sem. Sci. Techn.*, **11**, 1168 (1996).
- [Scriba93] J. Scriba, C. Gauer, A. Wixforth, J. Kotthaus, C. Bolognesi, C. Nguyen, and H. Kroemer. Spin- and Landau splitting of the cyclotron resonance in a non-parabolic two-dimensional electron system. *Sol. St. Comm.*, **86**, 633 (1993).
- [Shubnikov76] M. L. Shubnikov, D. V. Mashovets, and R. V. Parvenev. Magnetophon resonance in hydrostatically compressed indium arsenide. *Sov. Phys. Semicond.*, **9**, 989 (1976).
- [Snider90] G. L. Snider, I. H. Tan, and E. L. Hu. A self-consistent solution of Schrödinger/Poisson equations using a non-uniform mesh. *J. Appl. Phys.*, **68**, 4071 (1990). URL <http://www.nd.edu/~glsnider/>.
- [Stroessner86] K. Strössner, S. Ves, C. K. Kim, and M. Cardona. Dependence of the direct and indirect band gap of AlSb on hydrostatic pressure. *Phys. Rev. B*, **33**, 4044 (1986).

- [Symons98] D. M. Symons, M. Lakrimi, R. J. Nicholas, D. K. Maude, J. C. Portal, N. J. Mason, and P. J. Walker. Magnetic breakdown in the semimetallic InAs/GaSb system. *Phys. Rev. B*, **58**, 7292 (1998).
- [Symons94] D. M. Symons, M. Lakrimi, R. J. Warburton, R. J. Nicholas, N. J. Mason, P. J. Walker, and M. I. Eremets. Orientation and pressure dependence of the band overlap in InAs/GaSb structures. *Surf. Sci*, **9**, 118 (1994).
- [Sze81] S. M. Sze. *Physics of Semiconductor Devices*. John Wiley & Sons (1981).
- [Thomas96] K. Thomas, J. Nicholls, M. Simmons, M. Pepper, D. Mace, and D. Richie. Possible spin polarization in a one-dimensional electron gas. *Phys. Rev. Lett.*, **77** (1996).
- [Tscheuschner96] R. D. Tscheuschner and A. D. Wieck. Quantum ballistic transport in in-plane gate transistors showing onset of a novel ferromagnetic phase transition. *Superlatt. Microst.*, **20**, 615 (1996).
- [Tuttle89] G. Tuttle, H. Kroemer, and J. H. English. Electron concentrations and mobilities in AlSb/InAs/AlSb quantum wells. *J. Appl. Phys.*, **65**, 5239 (1989).
- [Tuttle90a] G. Tuttle, H. Kroemer, and J. H. English. Effects of interface layer sequencing on the transport properties of InAs/AlSb quantum wells: evidence for antisite donors at the InAs/AlSb interface. *J. Appl. Phys.*, **67**, 3032 (1990).
- [Tuttle90b] G. Tuttle, H. Kroemer, and J. H. English. Growth of InAs/AlSb quantum wells. In C. Tu, V. Matterna, and A. Gossard, editors, *III-V Heterostructures for electronic/photonic devices*, volume 145 of *MRS Symposia Proceedings*, 393. San Diego (1990).
- [Umbach84] C. P. Umbach, S. Washburn, R. B. Laibowitz, and R. A. Webb. Magnetoresistance of small, quasi-one-dimensional, normal-metal rings and lines. *Phys. Rev. B*, **30**, 4048 (1984).
- [vKlitzing80] K. von Klitzing, G. Dorda, and M. Pepper. Realization of a resistance standard based on fundamental constants. *Phys. Rev. Lett.*, **45**, 494 (1980).
- [Wang96] F.-C. Wang, W. E. Zhang, C. H. Yang, M. J. Yang, and B. Bennet. Observation of electrically resettable negative persistent photoconductivity in InAs/AlSb single quantum wells. *Phys. Rev. Lett.*, **69**, 1417 (1996).
- [Werking90] J. Werking, G. Tuttle, C. N. E. Hu, and H. Kroemer. InAs-AlSb heterostructure field-effect transistors fabricated using argon implantation for device isolation. *Appl. Phys. Lett.*, **57**, 905 (1990).
- [Yarlagadda91] S. Yarlagadda. Magnetization instabilities at tilted magnetic fields in the quantum hall regime. *Phys. Rev. B*, **44**, 13101 (1991).
- [Zallen67] R. Zallen and W. Paul. Effect of pressure on interband reflectivity spectra of germanium and related semiconductors. *Phys. Rev.*, **155**, 703 (1967).

Curriculum Vitae

Name: Sebastian Ludger Titus Brosig
born: May 10th, 1967, in Gelsenkirchen, Germany
Parents: Klara u. Bernd Brosig
Siblings: 2 brothers, born in 1961 und 1965

- 1973 Primary school
- 1977 Secondary school: Annette-von-Droste-Hülshoff-Gymnasium,
Gelsenkirchen-Buer
- 1986 Abitur, main exams in physics, chemistry
English and philosophy
- 1986 community service on a farm in Schleswig-Holstein
- 1988 work for a temporary staff agency: factory maintenance
and auxiliary industrial jobs
- 1988 physics course at Ruhr-Universität,
Bochum, Germany
- 1990 physics student the University of Sussex
as a member of an EU exchange programme
- 1992-'95 programming job as a 'Bochum verification project',
developing data acquisition and evaluation software for
acoustic and seismic data, for the
cooperative verification of arm reduction treaties
- 1994 begin of diploma work in the applied physics
group of Prof. Wieck
- 1996 Diploma thesis on "Insulating properties of focused ion
beam-written lines on GaAs/AlGaAs heterostructures"
- 9/1996 begin of PhD position in the
group of Prof. Ensslin, ETH, Zürich

Acknowledgements

First of all I would like to express my thanks to Prof. Klaus Ensslin. Without his constant support and supervision, exceeding, I believe, what is customary, I don't think I would have made it. His explanations, his feeling for the subject, and his enthusiasm helped me a great deal during this work.

Prof. A. D. Wieck willingness to come to Zurich as co-examiner for my work is greatly appreciated.

Of course I am indebted to the MBE growers in the group of Prof. Herb Kroemer at UCSB: Colombo R. Bolognesi, John English, George Tuttle, Chanh Nguyen and others grew InAs/AlSb quantum well samples of outstanding quality.

Thomas Heinzl and Thomas Ihn, whom I plagued with questions sometimes, always gave me the answers, and helped me on with that. The vast archive of Thomas Ihn's paper collection and his knowledge of who has written what, and where to find it, were indispensable.

Louis Jansen in Grenoble was both welcoming and helpful with the measurements at LCML. Richard Warburton and Sergio Ulloa gave me some theoretical support.

The technical support of Andreas Herrman and Paul Studerus was phenomenal. As an experimentalist one could not want better technicians.

My fellow PhD student Gian's friendly attitude made it fun to share a room with him, his clear perception about physics, and his ability to convey it too, gave me insights I wouldn't want to miss. I would like to thank my colleagues: Ryan, Silvia, Tobias, Volkmar, Jörg, Evaldo, Stefan and Andreas. Working in this group was fun.

Bulak and Branwen have both provided a light for me, at the end of the tunnel.